BROAD BEAM TRANSMISSION IN LEAD FILTERS

A Thesis Report

by

Ewa Papież

Submitted to the
Faculty of
Graduate Studies of
The University of Manitoba
in partial fulfillment of the
requirements for the degree
of Master of Science.

July, 1987

Winnipeg, Manitoba

ISBN 0-315-37275-3

BROAD BEAM TRANSMISSION IN LEAD FILTERS

BY

EWA PAPIEZ

A thesis submitted to the Faculty of Graduate Studies of
the University of Manitoba in partial fulfillment of the requirements
of the degree of

MASTER OF SCIENCE

TABLE OF CONTENTS

Page

Acknowledgements ii
Abstract iii
List of tables iv
List of figures v

Chapter

I. INTRODUCTION---------- 1
II. RADIATION SOURCES USED IN THIS WORK----------
2.1 Cobalt-60 radiation---------- 5
2.2 Medical Linear Accelerator----------12
III. INTERACTION OF RADIATION WITH MATTER----------18
3.1 X-ray attenuation----------18
3.2 Photon interaction with matter----------27
3.2.1 Coherent (Rayleigh) scattering----------29
3.2.2 Photoelectric effect----------29
3.2.3 Compton scattering----------34
3.2.4 Electron-positron pair production----------39
3.2.5 Relative cross sections----------42
IV. DOSIMETRY----------47
4.1 Cavity theory----------47
4.2 Dosimetric functions----------51
V. DOSE MODIFICATION BY LEAD FILTERS----------
5.1 Introduction----------59
5.2 The theoretical considerations----------59
5.3 X-ray dose calculation-practical methods-------68
5.4 The experimental parameters----------83
5.4.1 Introduction----------83
5.4.2 Radiation sources----------84
5.4.2.1 Cobalt-60----------84
5.4.2.2 4 MV x-rays----------84
5.4.3 Dosimetry devices----------85
5.4.4 Experimental setup----------88
5.5 The transmitted fraction of photonsmthrough the attenuator-TR----------93
5.5.1 Analysis----------104
5.6 The TR calculational method----------107
5.6.1 The calculational results----------117
5.6.2 The final dose distribution calculation------124
VI. CONCLUSIONS----------136
APPENDIX A----------138
APPENDIX B----------140
REFERENCES----------150

ACKNOWLEDGEMENTS

I would like to thank my supervisor, Dr. G. Froese, for introducing me to this project and also for his continuous support and encouragement while I was working on this project.

The assistance of the Machine shop staff is gratefully acknowledged.

Finally, I would like to thank my husband for his support and help during the course of this work.

This work was partly funded by Manitoba Cancer Treatment and Research Foundation.

ABSTRACT

There is at present no accurate method of dose calculation for the situation when beam modifying devices are used. The absorbed dose from a beam of incident photons at a point in a phantom can be presented as a product of dose in free space modified by the transmitted fraction of photons, TR and Tissue-air ratio, TAR. Once we are able to predict TR at any point across the attenuator and incorporate such data in further dose distribution calculations one should achieve much higher accuracy.

The narrow and broad beam transmission through lead was investigated in air for various radiation field sizes, thickness of attenuating material and angle from the central axis, for a geometry approximating typical treatment conditions for the Theratron "F" Co-60 unit and the 4 MV SHM linac.

A method to calculate the transmitted fraction of photons through any attenuator was developed.

When the calculated TR values were used in the dose distribution calculation for a wedge the errors in such a calculation diminished from 8% to 2.5%. As this method can be easily adapted to any beam attenuator it should be possible to obtain a similar accuracy in the dose distribution calculation for any attenuator, provided the geometrical and transmission data are known.

LIST OF TABLES

Table Page

3.1 Classification of photon interactions with matter----------28
5.1 The transmission data as measured and extrapolated for differentlead thickness, and radius of the field. The zero area and scatter component are displayed in different columns.----------102
5.2 The transmitted fraction values across the 30x30 cm^2 field at different points, for the 5.33 mm thick Pb slab----------118
5.3 The measured TR and the calculated TR values for the 45° wedge for 4MV SHM linac.----------121

LIST OF FIGURES

Figure Page

2.1 The decay scheme of ^{60}Co----------6
2.2 Measured pulse height distribution for the Stabilatron ^{60}Co source----------8
2.3 Normalized scattered photon distribution for ^{60}Co unit----------9
2.4 Overall view of Theratron "F" ^{60}Co unit----------10
2.5 Source head of Theratron "F" ^{60}Co unit----------11
2.6 X-ray head detail arrangement----------13
2.7 X-ray production----------14
2.8 Typical normalized photon distribution determined on the central axis----------16
2.9 Normalized photon distribution determined on the central axis, and at 5° and 9° off axis----------17
3.1 Arrangement for measuring narrow beam attenuation coefficient----------20
3.2 Arrangement for measuring broad beam attenuation coefficient----------22
3.3 Scattering of dN photons through an angle of Θ into the solid angle $d\Omega$----------25
3.4 Coherent or (Rayleigh) scattering in which an incident photon is scattered without a change in energy----------30
3.5 The photoelectric effect, incident photon is absorbed by an atom resulting in the ejection of a bound electron----------31
3.6 Photoelectric cross-sections for water and lead showing the discontinuities at the binding energies of different electron shells----------33
3.7 Compton scattering----------36
3.8 Klein-Nishina differential cross-section for various photon energies----------38
3.9 The total Compton coefficient, $_e\sigma$, the scatter coefficient, $_e\sigma_s$, and the transfer coefficient, $_e\sigma_{tr}$, as a function of photon energy----------40
3.10 Pair production----------41
3.11 Pair and triplet production cross-section for various material as a function of photon energy---43
3.12 Relative importance of the three principle interactions over a broad range of photon energies and absorbers----------45
3.13 Photon interaction cross-sections for lead--------46
4.1 Diagram illustrating the meaning of tissue-air ratio, which is the ratio formed by a dosimeter reading at X (in a water phantom) divided by its reading at the same point, X′, but in air---------53

LIST OF FIGURES (CON'T)

Figure Page

4.2 Graphs showing the dependence of tissue-air ratio of field size (radius) and depth----------55
4.3 Cross-section of a radiation beam, illustrating the sector integration method of calculating the dose due to scattered radiation at points either in or out the beam----------57
5.1 Geometry used for the calculation of primary and first scatter dose to point, P from three separate layers (lead, air, water) in a divergent beam-----61
5.2 Diagram to illustrate the calculation of the dose at point, P----------76
5.3 Diagram to illustrate the calculation of the dose at point, P for rectangular beams----------77
5.4 The errors in dose distribution calculation, when 45° wedge for 4 MV SHM linac is inserted into the beam----------80
5.5 Automatic 2D isodose plotter system configuration-87
5.6 The experimental setup for the transmission study for Co-60 radiation----------89
5.7 The experimental setup for the transmission study for 4 MV x-rays----------91
5.8 Experimental setup for transmission measurements at different -angles off the central axis--------92
5.9 The transmission through lead for Co-60 -rays as a function of radius of the field, each curve plotted for diffrent thickness of lead filter-----94
5.10 The transmission through lead for 4 MV x-rays as a function of radius of the field, each curve plotted for diffrent thickness of lead filter-----95
5.11 The scatter component of the total transmission plotted as a function of the radius of the field, each curve corresponds to different thickness of lead filter----------97
5.12 The total transmitted fraction of photons plotted as a function of the attenuator thickness, each curve for different radius of the field size-98
5.13 The zero area component of the total transmission TR and the total TR measured across the radiation field as a function of the distance off the central axis, each curve represents data for different filter thickness for a 30x30 cm^2 field----------100
5.14 The zero area component of the total transmission as a function of the distance off the central axis----------101

LIST OF FIGURES (CON'T)

Figure Page

5.15 Effective attenuation coefficient as a function of the attenuator thickness, each curve represents data for different field size----------106
5.16 Diagram illustrating the zero area and scatter component of the total transmitted fraction------109
5.17 Diagram showing representation of a beam of rectangular cross-section by a summation of sectors of circular beams, $\Delta\Theta$ is the angular width of one sector at an angle Θ and $R(\Theta)$ is its radius----------111
5.18 Diagram showing a schematic representation of geometry for the transmitted fraction calculation at point, P due to scatter arising within a volume element through point Q. The right hand diagram shows the beam cross-section through points P and Q----------114
5.19 Diagram illustrating the sector integration method of calculating the transmitted fraction of photons at any point in the radiation field----------116
5.20 The errors between measured and calculated TR values for a 5.33 mm slab----------119
5.21 Comparison of measured and calculated transmitted fractions across the 45° wedge. Bottom part shows the transmitted fractions as a function of the distance from the central axis----------122
5.22 The errors between measured and calculated TR values for 45° wedge for 4 MV SHM linac----------123
5.23 The beam profiles for open field and field altered by the 20° wedge for a Co-60----------125
5.24 The beam profiles for 45° wedge and open field for the 4 MV SHM linac----------126
5.25 The calculated and measured beam profiles, at 10 cm depth for 20° wedge for Co-60----------127
5.26 The calculated and measured beam profiles, at 10 cm depth for 45° wedge for the 4 MV linac--128
5.27 Comparison of the measured and calculated beam profiles for 20° wedge for Co-60----------130
5.28 Comparison of the measured and calculated beam profiles for 45° wedge for 4 MV linac----------131
5.29 The calculated and measured beam profiles at 5 cm depth for 45° wedge for the 4 MV linac----------132
5.30 The calculated and measured beam profiles at 15 cm depth for 45° wedge for the 4 MV linac----------133
5.31 Comparison of the measured and calculated beam profiles at 5 and 15 cm depth for 45° wedge for the 4 MV linac----------134
A.1 The scatter component of the transmitted fraction of photons----------139

I. INTRODUCTION

Radiotherapy stands as one of the three major modalities employed in cancer treatment, the other two being surgery and chemiotherapy. Varying degrees of damage are exhibited by all cells upon exposure to radiation.

A condition for successful radiation therapy is a homogeneous dose distribution in the target volume, which is defined as the volume within which a specified absorbed dose is to be delivered, together with optimal sparing of the surrounding normal tissues. There remains a need for precise target volume localization, knowledge of dose tolerances of normal tissues and also a detailed under - standing of the application of dose modifying devices. Isodose shaping can help to prevent over- or underdosage in parts of the target volume and to shield critical organs. Special collimators and penumbra trimmers reduce unwanted radiation for γ-radiation teletherapy units. Beam flattening filters correcting the forward peaked production rate of photons are necessary with electron accelerators. Special individual shields of highly attenuating materials (compensators and wedges) produce a flat beam profile at some defined depth in the patient. All these beam modifying devices alter the dose distributions by removing some of the incident primary photons. In doing so they produce scattered radiation; secondary

electrons and scattered photons thus impinge on the patient. The electrons compromise the skin sparing characteristics of the beam, while the presence of scattered photons may complicate the design of wedges or compensators as well as the subsequent calculations of dose distribution.

The degree of accuracy needed for clinical acceptability is not known and has been the subject of considerable debate. Evidence has been presented by Shukowsky (1970) and Herring and Compton (1970) that an increase of 10% above the "optimal" dose has produced an observable increase of tissue necrosis, while a reduction in the dose of 10% greatly decreases the chance of local control. The ICRU #24 (1976) concludes that the "available evidence for certain types of tumors points to the need for an accuracy of 5% in the delivery of an absorbed dose to a target volume if the eradication of the primary tumour is sought". The degree of error considered clinically acceptable is therefore within 5% of the dose to the target volume specified by the radiotherapist. Sources of error causing a shift from the dose specified may, for example, be patient motion; inexact placement of the treatment field; lack of anatomical data for dose computation algorithms of limited accuracy. To achieve an overall dose accuracy of

within 5%, systematic sources of error such as the accuracy of the dose computational algorithm should be minimized.

Accurate predictions of the dose in a phantom for various beam shaping devices and parameters of the beam can only be achieved with Monte Carlo calculations which are both complicated and time consuming. This limits the use of this method for practical calculations in treatment planning process. Various practical methods have been proposed to calculate the dose distribution when beam modifying devices are used. One of such methods is the calculational procedure used in the AECL treatment planning system (presently in use in the MCTRF). Such calculations are based on the empirical data for the attenuation of the photons by the filter and the overlying tissue. The errors involved in dose calculation with this algorithm are unacceptably large, as discuss in section 5.3. In practice it is necessary to adjust the input data describing the attenuating characteristics of the given filter by comparison with a measured dose distribution in order to obtain acceptable results. The absorbed dose from a beam of incident photons at a point in a phantom can be presented in simplified form as a product of dose in free space modified by the transmission through the filter and tissue-air ratio. The

presence of any attenuator will have an influence on dose in air as well as on TAR. If the "hardening" of the beam by a filter can be neglected, the main source of errors is the transmitted fraction of photons through the attenuator, TR .

The aim of this project was to develop a calculational method which allows the prediction of the transmitted fraction of photons through the attenuator at any point in the beam with appropriate accuracy. This would decrease the errors involved in dose distribution calculations whenever beam modifying devices are used. To be able to achieve this objective, the photon transmission through the lead attenuators as a function of field size, thickness of lead filter and the changes in the energy spectrum of the radiation beam were investigated.

This study has been organized into both theoretical and experimental sections. The theoretical section, which covers the basic concepts of the interaction of radiation with matter, the production of radiation for radiotherapy treatment, dosimetry and dose distribution calculation methods, is covered in chapters II through IV and part of chapter V. The experimental section is contained in chapter V. Conclusions are presented in chapter VI.

II. RADIATION SOURCES USED IN THIS WORK

2.1. Cobalt 60 radiation

γ-rays emitted in the decay of radioactive isotopes are an important source of radiation used in medicine. ^{60}Co with a half life of 5.26 years is produced by neutron activation of naturally occurring ^{59}Co. The decay scheme of ^{60}Co is shown in Fig.(2.1). ^{60}Co decays with a probability of 99.88% by emission of a β^- with a maximum energy of 0.315 MeV to form an excited state of ^{60}Ni. This excited state of ^{60}Ni decays rapidly by emission of two γ-rays of energies 1.1732 and 1.3325 MeV respectively in cascade. ^{60}Co decays also with probability of 0.12% by emission of a β^- with a maximum energy of 1.4847 MeV to form the lower excited state of ^{60}Ni which then rapidly decays by the emission of a 1.3325 MeV γ-ray. The two γ-rays of energy 1.1732 and 1.3325 MeV, with relative intensities of 99.88% and 100% respectively, provide the radiation used in ^{60}Co therapy and the pair is usually treated as a single photon of 1.25 MeV. The photon beam from a ^{60}Co therapy unit consists of not only the initial 1.17 and 1.33 MeV photons but also photons whose energies have been reduced by scattering processes in the source, its spacer sleeve, the housing and the collimator. Experimental

Figure 2.1. The decay scheme of ^{60}Co, published by Dillman (1975)

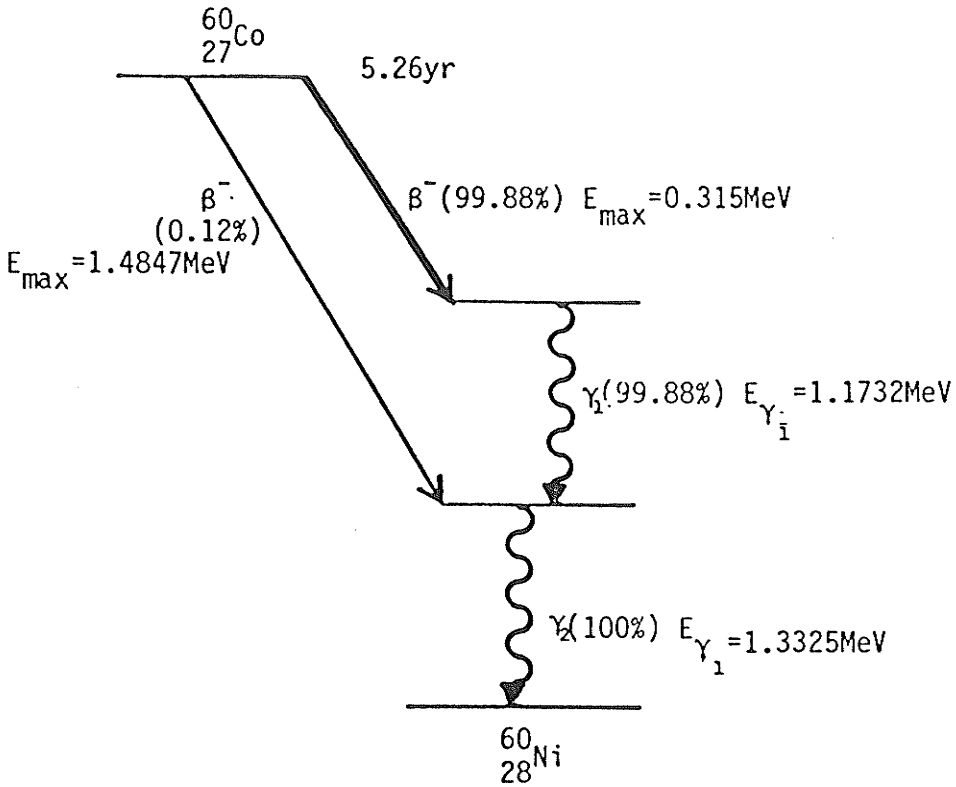
$^{60}_{27}Co$
5.26yr
β^- (0.12%)
E_{max}=1.4847MeV
β^-(99.88%) E_{max}=0.315MeV
γ_1(99.88%) E_{γ_1}=1.1732MeV
γ_2(100%) E_{γ_2}=1.3325MeV
$^{60}_{28}Ni$

investigations of the spectrum from ^{60}Co have been made by Costrill (1962), Aitken and Henry (1964), Scrimger and Cormack (1963), Godwin and Opal (1965), Löfroth (1973), Jessen (1973) and Enow and Jessen (1974). A typical set of results from a ^{60}Co source measured by Jessen (1973) is depicted in Fig.(2.2). The scattered radiation in the iterated spectrum coming from scattering within the source itself in the surrounding capsule and from the shield and collimating device published by Löftroth (1973) is illustrated in Fig.(2.3). The ^{60}Co machine used in this project is illustrated in Figs (2.4) and (2.5). The ^{60}Co source is uncapsulated in two stainless steel welded containers which are surrounded by a high Z shielding material, such as tungsten, on all sides except for the window through which the γ-rays are emitted. The source is placed near the centre of a lead filled steel container which serves as the head of the treatment device. To provide the γ-ray beam for treatment the source is positioned inside the head at an opening which serves as a radiation port to volumes external to the head. The method of source exposure used in Theratron „F" ^{60}Co unit is illustrated in Fig.(2.5). In the "off" position the source is shielded by a shielding shutter block, which is constructed in a way which assures that whenever any failure occurs the source is shielded from the outside.

Figure 2.2. Measured pulse height distribution for the Stabilatron ^{60}Co source, Jessen (1973).

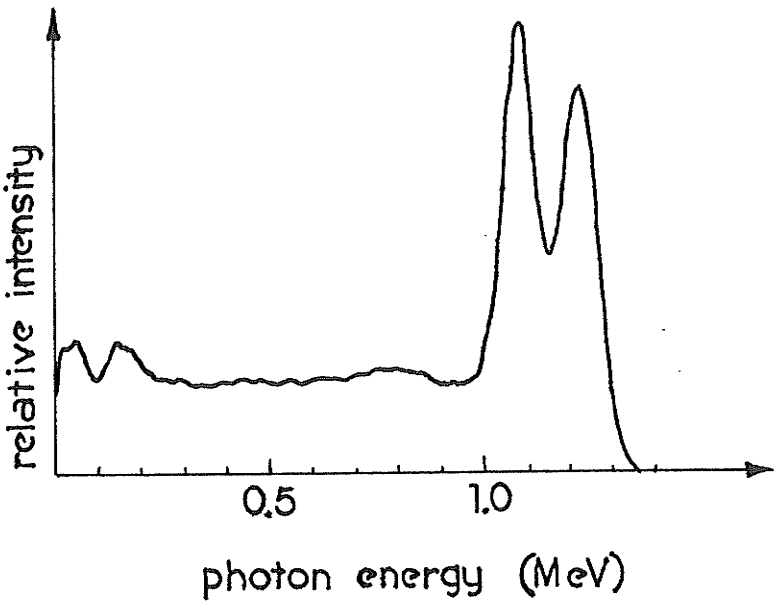
relative intensity
0.5
1.0
photon energy (MeV)

Figure 2.3. Normalized scattered photon distribution for ^{60}Co unit, Löftroth (1973) . F(E) is fractional signal due to the photons of energy E.

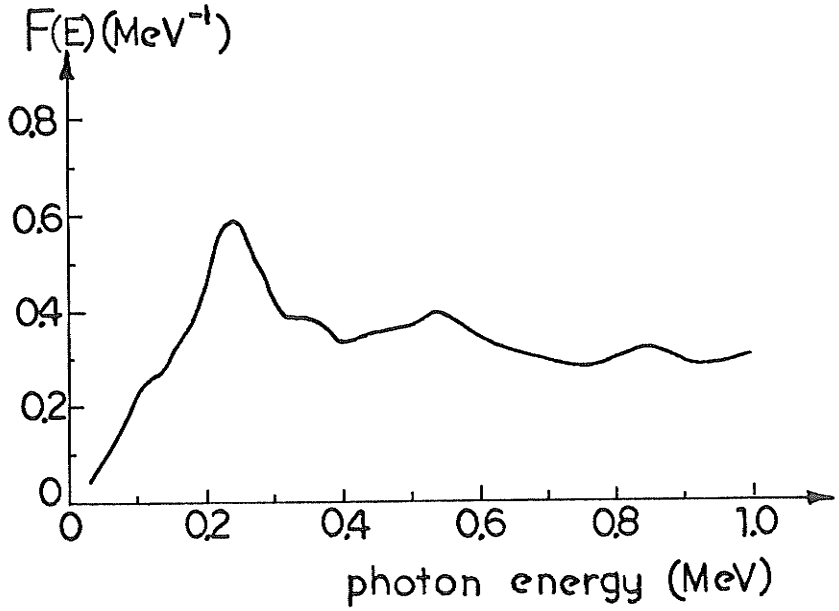
F(E) (MeV⁻¹)
0.8
0.6
0.4
0.2
0
0
0.2
0.4
0.6
0.8
1.0
photon energy (MeV)

Figure 2.4. Overall view of Theratron "F" ^{60}Co unit.

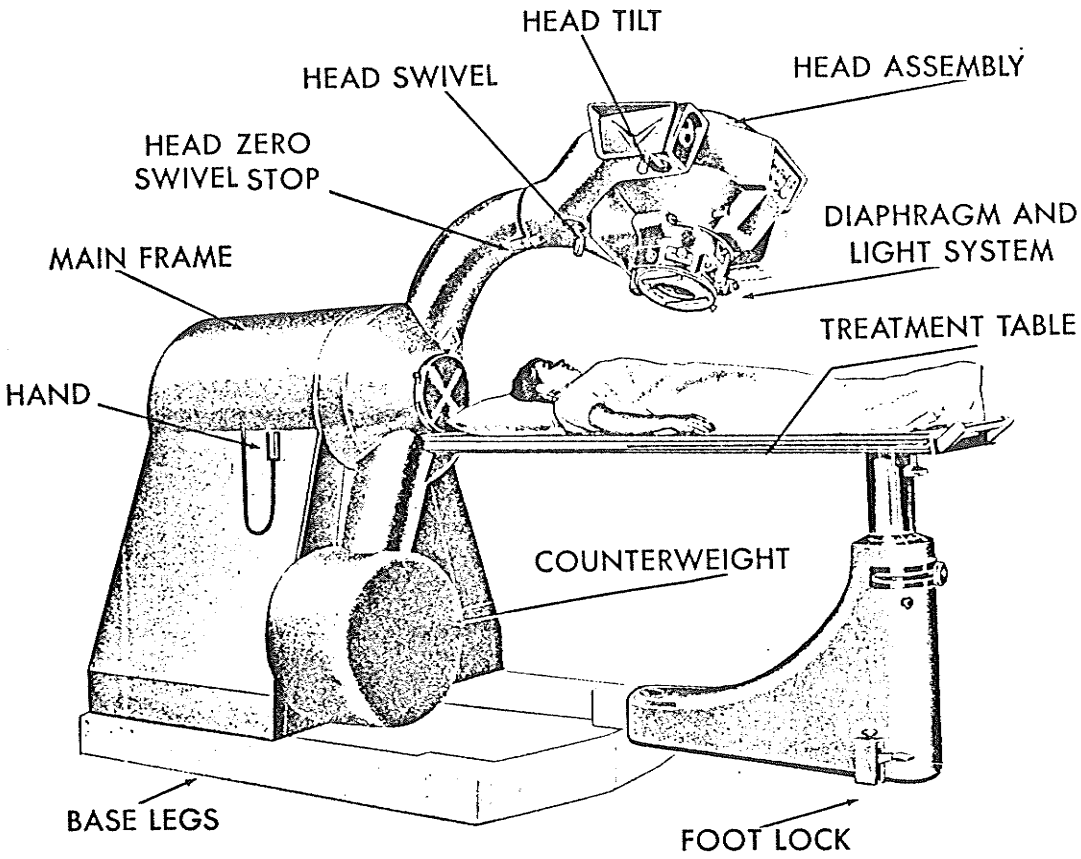

Overall View of Model "F"
with Alternate Counterweight

Figure 2.5. Source head of Theratron "F" ^{60}Co unit, reproduced from the Theratron "F" manual.

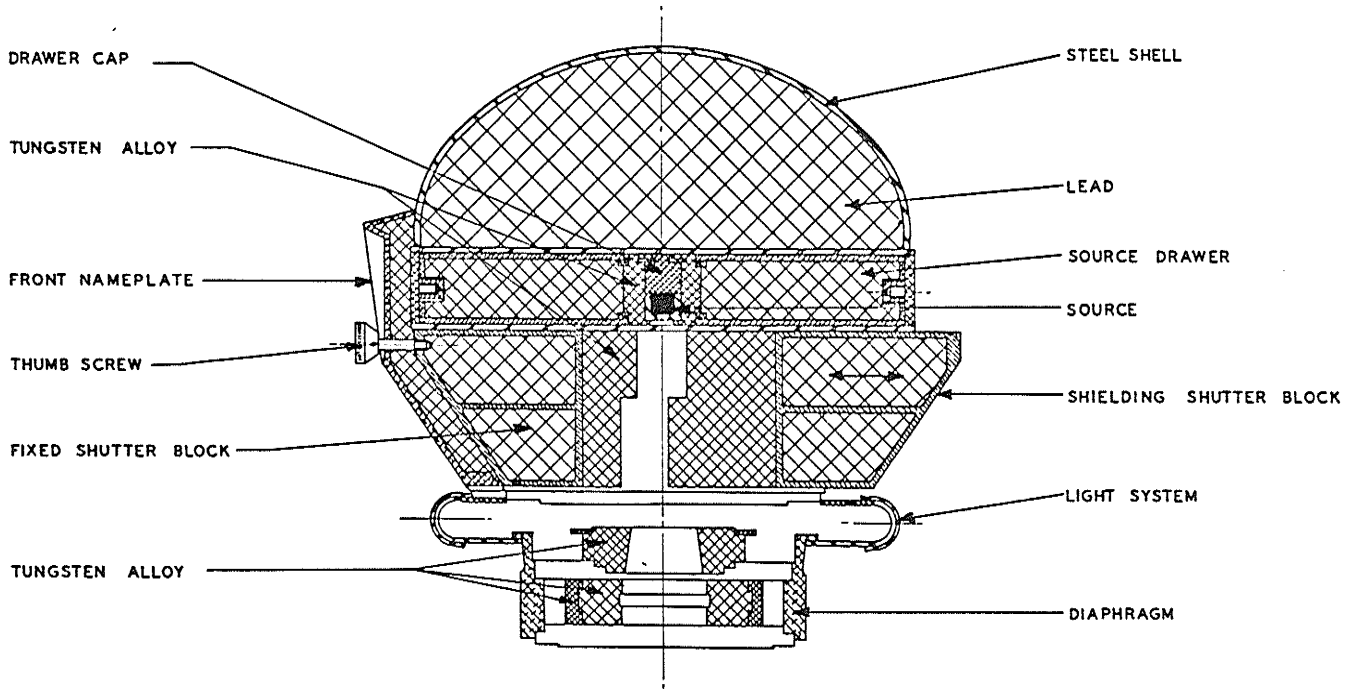
DRAWER CAP
TUNGSTEN ALLOY
FRONT NAMEPLATE
THUMB SCREW
FIXED SHUTTER BLOCK
TUNGSTEN ALLOY
STEEL SHELL
LEAD
SOURCE DRAWER
SOURCE
SHIELDING SHUTTER BLOCK
LIGHT SYSTEM
DIAPHRAGM

SOURCE HEAD

2.2. Medical Linear Accelerator.

The second photon beam used in this work was produced by a medical electron linear accelerator, the Therapi 4, manufactured by SHM Nuclear Corporation. The electron linear accelerator uses microwave power to accelerate electrons to high energies. The accelerated electrons are directed onto a target where they produce bremsstrahlung photons and these photons are used in radiotherapy treatment. The microwave power supply consists of a magnetron. The microwave power generated by the magnetron is transported by means of a waveguide to the accelerator structure. The accelerator structure is a microwave resonant cavity and provides the environment wherein electrons may be accelerated to high energies by means of their interaction with microwaves. The treatment head contains beam modifying and monitoring devices,Fig.(2.6).

The 4 MV linac produces a parallel beam of 4 MeV electrons, approximately 3 mm in diameter. Bremsstrahlung x-rays are produced when the electron beam is incident on the high Z target. This target ia attached to the end of the accelerator structure in a straight through design. The thickness of the target is large enough to stop most of the incident electrons. The x-ray intensity is forward peaked as shown in Fig.(2.7). To ensure

Figure 2.6. X-ray head detail arrangement, reproduced from the Therapi 4 manual.

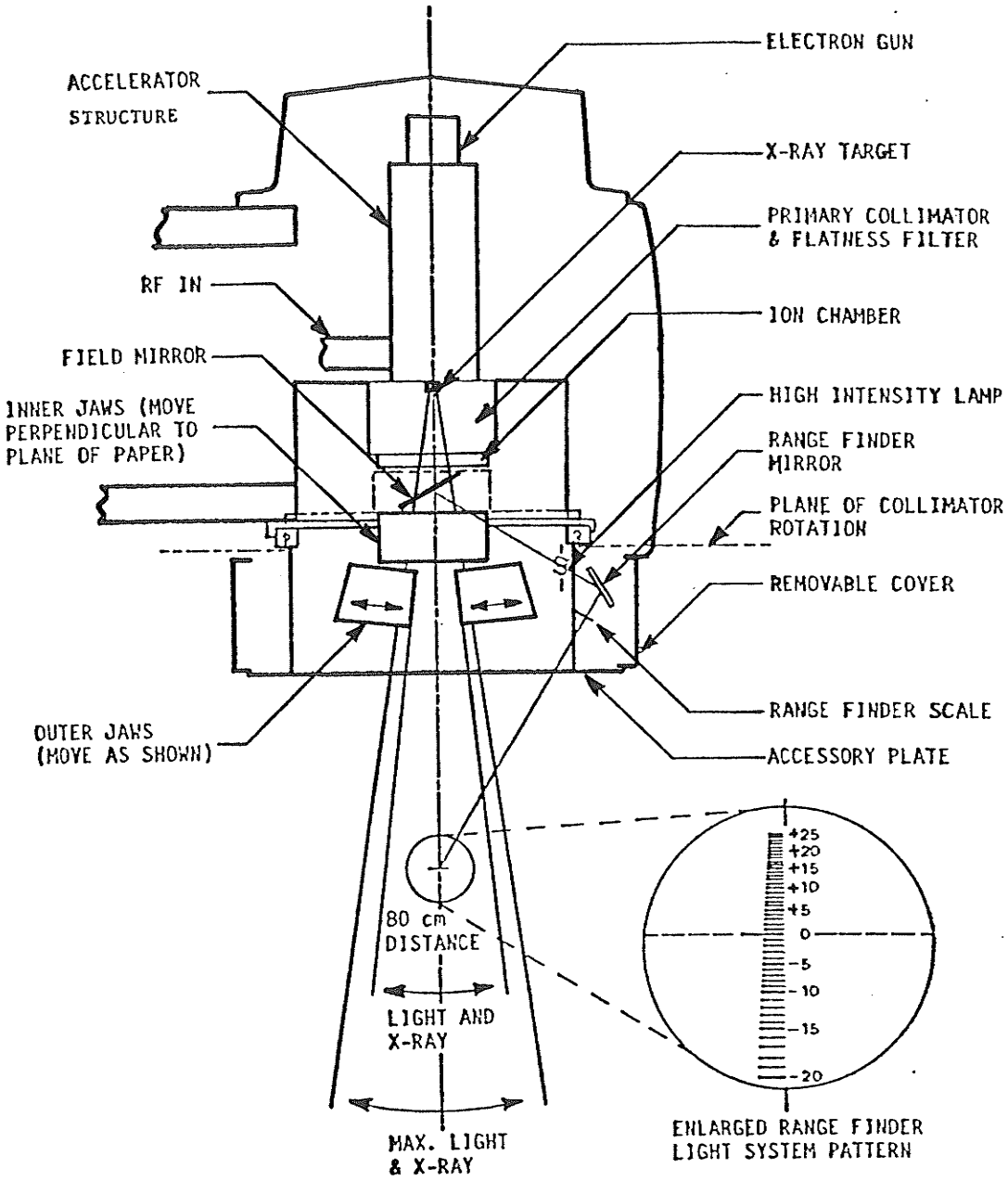
ELECTRON GUN
ACCELERATOR STRUCTURE
X-RAY TARGET
PRIMARY COLLIMATOR & FLATNESS FILTER
RF IN
ION CHAMBER
FIELD MIRROR
HIGH INTENSITY LAMP
INNER JAWS (MOVE PERPENDICULAR TO PLANE OF PAPER)
RANGE FINDER MIRROR
PLANE OF COLLIMATOR ROTATION
REMOVABLE COVER
RANGE FINDER SCALE
OUTER JAWS (MOVE AS SHOWN)
ACCESSORY PLATE
80 cm DISTANCE
LIGHT AND X-RAY
MAX. LIGHT & X-RAY
+25
+20
+15
+10
+5
0
-5
-10
-15
-20
ENLARGED RANGE FINDER LIGHT SYSTEM PATTERN

Figure 2.7. X-ray production.

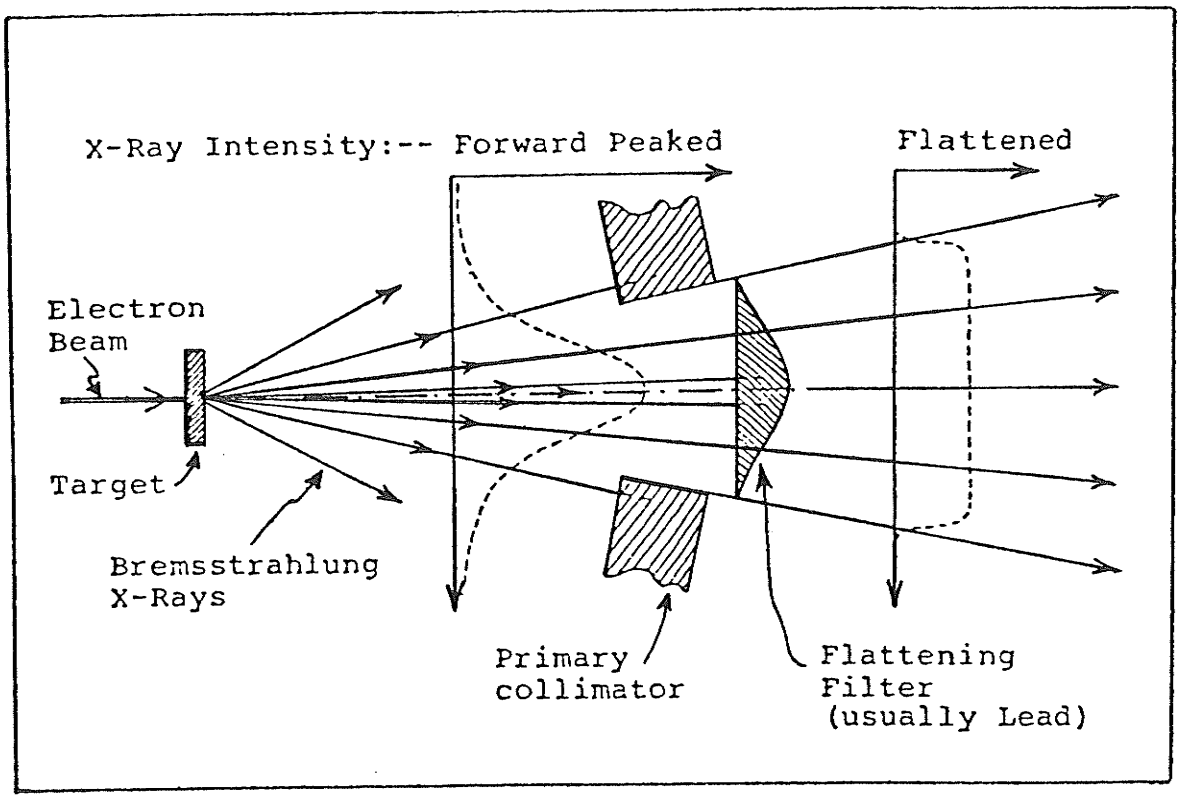
X-Ray Intensity:-- Forward Peaked
Flattened
Electron
Beam
Target
Bremsstrahlung
X-Rays
Primary
collimator
Flattening
Filter
(usually Lead)

relatively uniform beam intensity over a cross sectional area, an x-ray flattening filter made of high Z material is inserted in front of the primary collimator.

The bremsstrahlung energy spectrum in the central part of a photon beam as reconstructed from the transmission measurements by Mohan (1985) is somewhat harder than in the region near the edge of the beam. The flattening filter not only hardens the beam as a whole, but further enhances the relative hardness near the centre. Variation of the energy across the beam is important when calculating transmission through any attenuator. The energy spectrum derived by Huang et al.(1983) for few different 4 MV linear accelerators is depicted in Fig.(2.8), and the variation of energy spectrum as a function of radial distance from the central ray presented by Huang et al. (1983) is shown in Fig.(2.9).

Figure 2.8. Typical normalized photon distribution determined on the central axis for 4 MV linear accelerator, Huang et al.(1983). F(E) is fractional signal due to the photons of energy E.

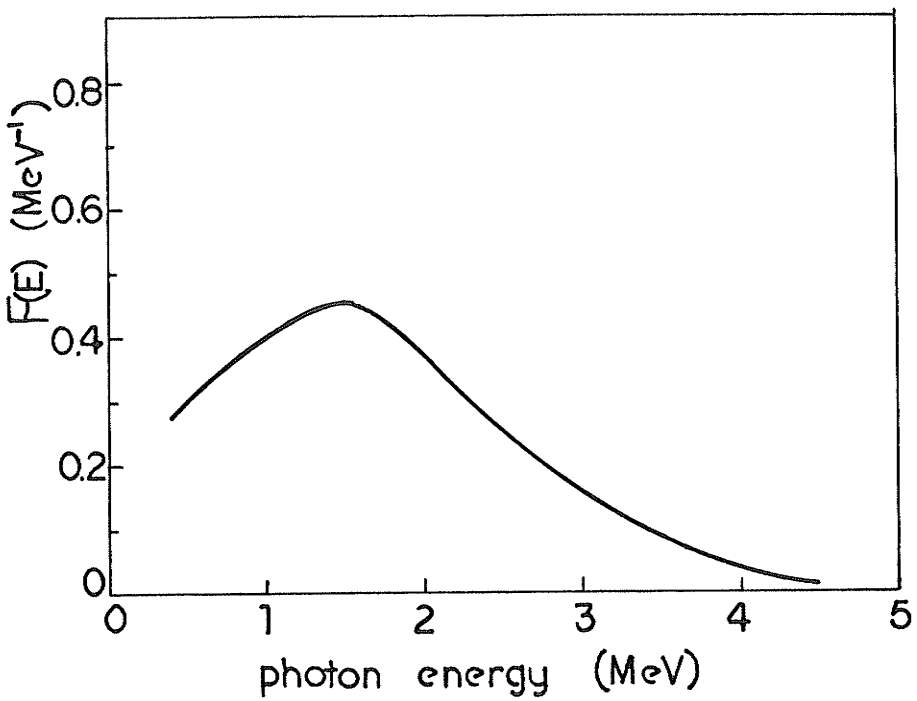
F(E) (MeV⁻¹)
0.8
0.6
0.4
0.2
0
0
1
2
3
4
5
photon energy (MeV)

Figure 2.9. Normalized photon distribution determined on the central axis, and at 5° and 9° off axis, Huang et al.(1983). F(E) is a fractional signal due to the photons of energy E.

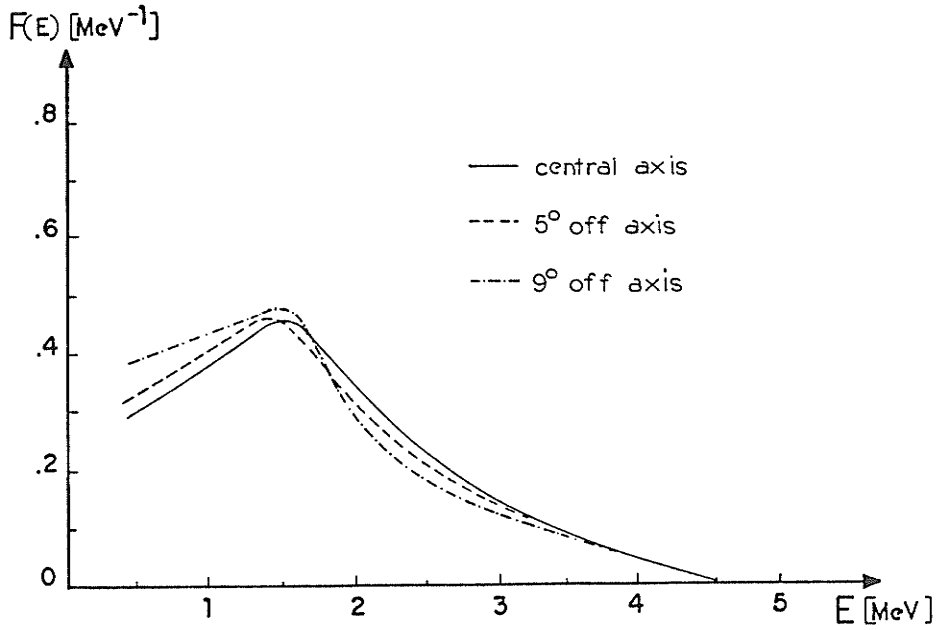
F(E) [MeV^{-1}]
.8
.6
.4
.2
0
1
2
3
4
5
E [MeV]
central axis
5° off axis
9° off axis

III. INTERACTION OF RADIATION WITH MATTER

An x-ray photon often experiences as many as 10 scattering processes before its eventual absorption. The direction of propagation thereby becomes increasingly random, and the initial straight penetration tends to go over into a diffusion process. The interaction processes which will be described in the section 3.2. experienced by x-rays give rise to a variety of "secondary radiations" The x-rays emitted directly from a source are called "primaries". For primary x-rays up to 10 MeV, the secondaries that contribute much to penetration are themselves x-rays of lower energies. The study of x-ray attenuation deals with photons of various energies, even where the primaries are monoenergetic.

3.1. X-ray attenuation.

The most important quantity characterizing the penetration of gamma radiation in extended media is the linear attenuation coefficient, μ . This quantity depends on the photon energy, E, and on the atomic number, Z, of the medium, and the density and may be defined as the probability per unit length that a photon will interact with the medium. The total probability that a photon of given energy suffers some interaction process while

traversing a layer of matter is studied experimentally with the arrangement shown schematically in Fig.(3.1). An x-ray beam may be characterized in terms of its fluence, Φ , which is the number, dN, of photons incident normal to area, dA.

$$\Phi = dN/dA \ . \qquad 3.1$$

A well collimated ("narrow") beam of monochromatic x-rays penetrates a layer of absorber and then reaches a detector. Attenuation of the photon beam prevents it from reaching the detector. The narrow parallel incident beam of fluence, Φ_o, of Fig.(3.1) which traverses the slab of material of infinitesimal thickness, dx, will be diminished in fluence by an amount $d\Phi$ according to the relation:

$$d\Phi \propto \Phi dx \qquad 3.2$$

or

$$d\Phi = -\mu dx \ . \qquad 3.3$$

The constant of proportionality, μ, is called the linear attenuation coefficient, and it represents the fraction of photons removed from the beam per unit path length. Rearranging (3.1) one obtains:

$$d\Phi/\Phi = -\mu dx \qquad 3.4$$

and upon integration (3.3) becomes

$$\Phi = \Phi_o e^{-\mu x} \qquad 3.5$$

Figure 3.1. Arrangement for measuring narrow beam attenuation coefficient, Fano(1953).

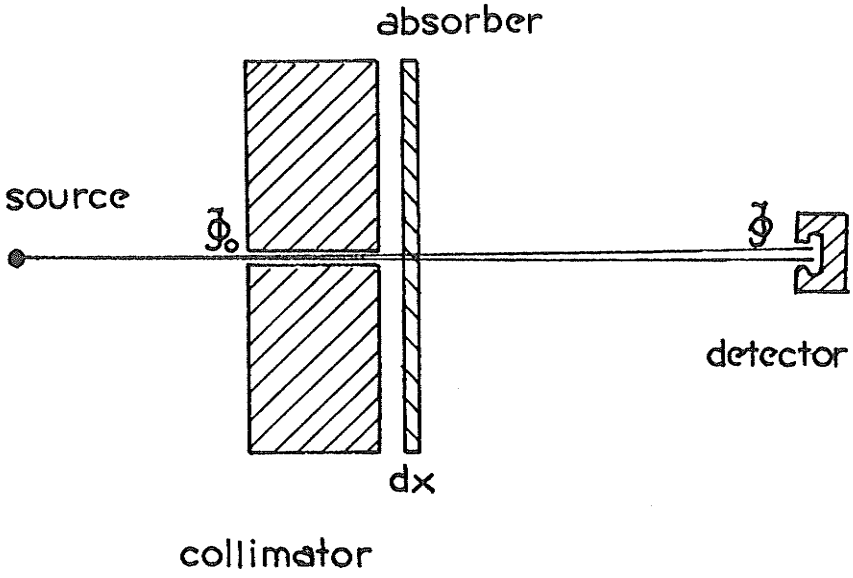
absorber
source
$\vec{\Phi}_o$
$\vec{\Phi}$
detector
dx
collimator

where Φ_o is the initial photon fluence and Φ the resultant beam fluence upon traversing a thickness, x, of material. The ratio of the resultant beam fluence, Φ, to the initial photon fluence, Φ_o, represents the transmitted fraction of primary photons and is called transmittance, TR.

$$TR = \Phi/\Phi_o = e^{-\mu x} . \qquad 3.6$$

The thickness, x, of absorber required to attenuate the beam by a factor of e is called the mean-free-path of the incident photons. Such a thickness, or path length, represents the mean distance traversed by a photon in the absorber medium between successive interactions and is equal to the inverse of the linear attenuation coefficient, μ^{-1}. In an attenuation experiment free from the "narrow-beam" limitation -Fig.(3.2), in which the aperture of the collimator has been greatly increased, the loss by scattering of some photons initially aimed at the detector is compensated in part by photons scattered from the absorber. Therefore one finds a higher transmittance under "broad beam" than under "narrow beam" conditions. Attenuation for "broad beam" geometry will no longer be strictly exponential, but may be described by:

$$\Phi = \Phi_o e^{-\mu x} \; B(x, A, d, h\nu) . \qquad 3.7$$

Where B is a modification factor, often referred to as a "build-up" factor, which is a function of an absorber

Figure 3.2. Arrangement for measuring broad beam attenuation coefficient, Fano (1953).

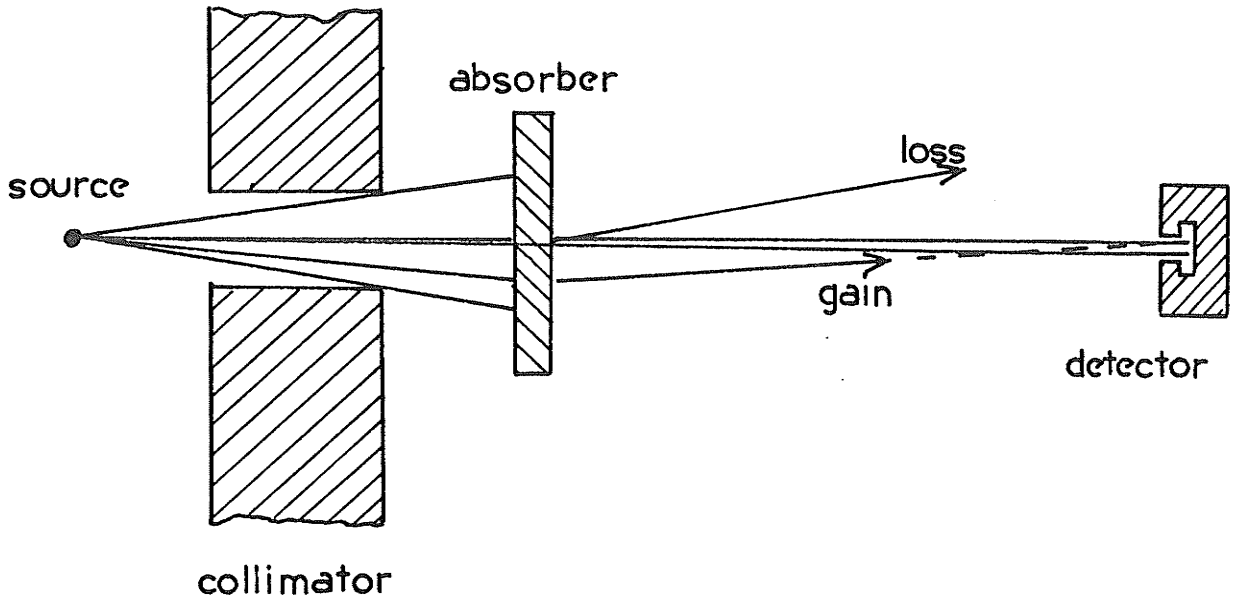
absorber
loss
source
gain
detector
collimator

thickness, x, beam area, A, distance of detector from the absorber, d, and incident beam energy, $h\nu$. It is often convenient to express attenuation independent of absorber density and this may be achieved by dividing the linear attenuation coefficient, μ, by the density, ϱ, of the absorber material. The attenuation coefficient, μ/ϱ, thus generated is called the mass attenuation coefficient. If the units of μ are expressed in cm^{-1} then the units of μ/ϱ are cm^2/g and μ/ϱ thus specifies the fraction by which an incident beam is reduced by a layer of absorber of thickness 1 g/cm^2. Similarly one may also define atomic and electronic attenuation coefficients respectively as:

$$a^{\mu} = (\mu/\varrho)(A/N_o) \qquad 3.7$$

$$e^{\mu} = (\mu/\varrho)(A/N_oZ) \qquad 3.8$$

where: A is the atomic weight of the absorber, N_o is Avogadro's number and Z is the effective atomic number of the absorber material.

Attenuation coefficients for a large number of atomic numbers over a large range of photon energies have been tabulated and published by Hubble and National Bureau of Standards (1969). With the concept of fluence, Φ, one may define another quantity the scattering cross-section σ.

Consider an x-ray beam of fluence, ϕ, incident upon a target as depicted in Fig.(3.3). Of the N photons incident upon area, A, of the target, dN photons are scattered through an angle, Θ, into the solid angle, $d\Omega$, and are detected by the detector. If there are n (el/cm^2) independent interaction or scattering sites in the irradiated area, A (cm^2), then the number, dN, of photons scattered into the solid angle, $d\Omega$, is given by:

$$dN = A\, n \left(d\sigma/d\Omega(\Theta)\right) d\Omega\, dx\, \rho_e \qquad 3.10$$

where, (Θ), (which has units of area) is the constant of proportionality specifying the probability of a photon being scattered through an angle Θ into the solid angle, $d\Omega$ and ρ_e (el/cm^3) is electron density of the target material. One may also write $\sigma(\Theta)$ as:

$$\frac{d\sigma}{d\Omega}(\Theta)\, d\Omega = d\sigma(\Theta) \qquad 3.11$$

and thus $d\sigma/d\Omega(\Theta)$ is called the differential cross-section of the scattering event. Photons may be scattered into any angle and hence the probability of a photon being scattered by the target may be obtained by integrating the differential scattering cross section, $\sigma(\Theta)$ (O), over all solid angles:

$$\sigma_{tot} = \oint \frac{d\sigma}{d\Omega}(\Theta)\, d\Omega = \oint \sigma(\Theta)\, d\Omega \qquad 3.12$$

to obtain the total scattering cross section σ_{tot}. Thus the total number of photons, dN_{tot} scattered out of the beam (assuming narrow beam geometry) is:

Figure 3.3. Scattering of dN photons through an angle of Θ into the solid angle $d\Omega$.

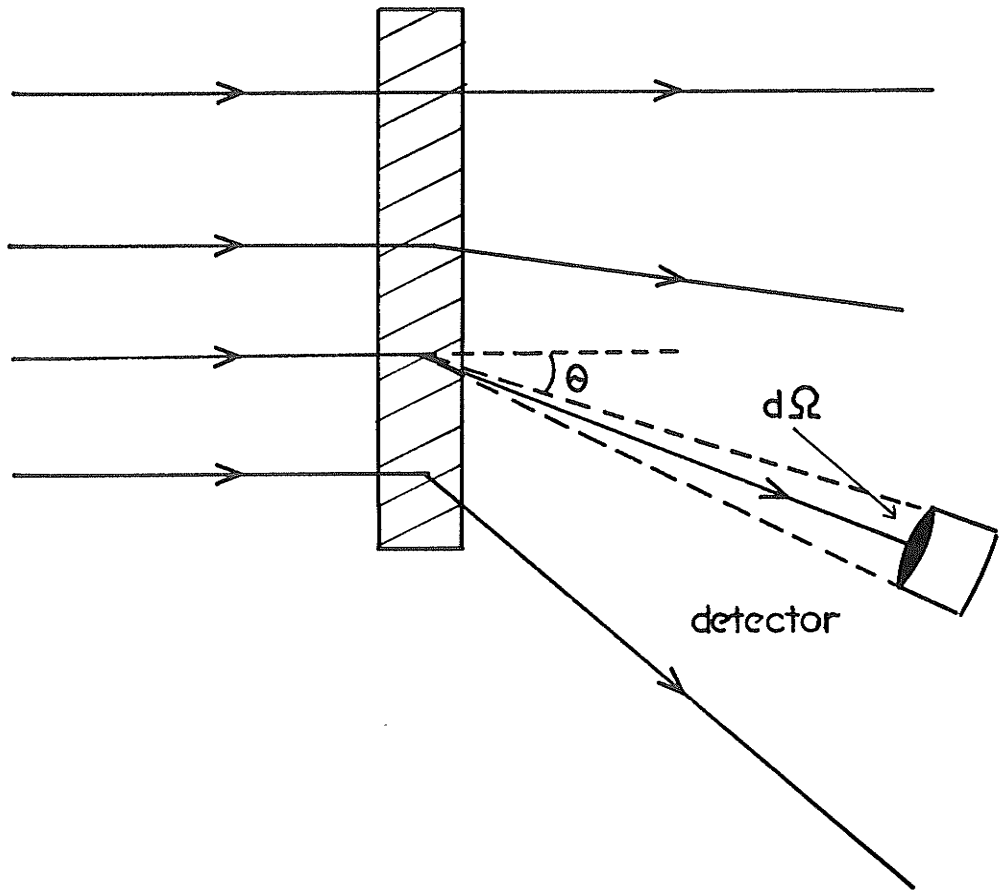
θ
dΩ
detector

$$dN_{tot} = \int dN = \Phi n \int \sigma(\theta)\, d\Omega = \Phi n \sigma_{tot} \quad . \qquad 3.13$$

The number, N_{tot}, of photons incident on the target is ΦA and hence the fractional decrease (or attenuation) of the beam due to the target is:

$$dN_{tot}/N_{tot} = dN_{tot}/\Phi A = (n/A)\, \sigma_{tot} \quad . \qquad 3.14$$

Thus if the scattering sites are taken to be the atoms in the target then:

$$\sigma^{a}_{tot} = \mu_a = (\mu/\rho)\ (A/N_o) \qquad 3.15$$

or

$$\sigma^{e}_{tot} = \mu_e = (\mu/\rho)\ (A/ZN_o) \qquad 3.16$$

if the scattering sites are taken to be the electrons.

A large number of cross sections are of the order of $10^{-24} cm^2$ and thus cross sections are often given in terms of barns (b):

where: 1 barn=1b=10^{-24} cm^2

3.2. Photon interaction with matter

When a beam of photons passes into an absorbing medium some of the energy carried by the beam is transferred to the medium where it may produce biological damage. The energy deposited per unit mass of the medium is known as the absorbed dose. The biological events that result from this damage are quite complicated. The initial step in the process usually involves the collision between a photon and an electron in the material, resulting in the scattering of some radiation and the setting in motion of a high speed electron. Electromagnetic radiation of high energy usually originates from excited nuclei, from excited atoms, or from electrons traversing matter and interacting with the electromagnetic field of the nucleus. In Table (3.1) the elementary photon interactions are classified. Each of the interactions serves to attenuate the primary beam and in the process transfer a varying amount of energy to matter. One such interaction which transfers no energy to the attenuating medium is that of coherent scattering.

Table 3.1. Classification of photon interactions with matter.

Interaction with	Type of Interaction		
	Absorption	Elastic (coherent)	Inelastic (incoherent)
Atomic electrons	Photoelectric effect	Rayleigh scattering	Compton Scattering
Nucleons	Photonuclear reactions	Elastic nuclear scattering	Nuclear resonance scattering
Electric field of charged particles	Pair and Triplet production		
Mesons	Photomeson production		

3.2.1. Coherent (Rayleigh) scattering.

The process of coherent scattering is depicted in Fig.(3.4). Here an x-ray photon is incident upon an atom but does not result in the excitation of the atom. The photon is scattered by the bound electrons of the atom and the scattered photon exits without a loss of energy. The differential cross section for coherent scattering is given by:

$$d\sigma/d\Omega_{coH} = (r_o^2/2)(1+\cos^2\theta)\,[F(q,Z)]^2 \qquad 3.17$$

where: r_o is = 2.81794 10^{-5} m (the classical electron radius) and F(q, Z) is the atomic form factor.

The square of this atomic factor gives the probability that the Z electrons of the interacting atom will receive a recoil moment, q, without the absorption of energy. This interaction occurs mainly for low energy photons interacting with high Z atoms and resulting scattered photons are strongly forward peaked. Thus the coherent scattering serves to diverge the incident x-ray beam.

3.2.2. Photoelectric effect.

In the photoelectric process illustrated in Fig.(3.5), a photon with an energy, $h\nu$, collides with an atom and ejects one of the bound electrons from K,L,M or N shells.

Figure 3.4. Coherent or (Rayleigh) scattering in which an incident photon is scattered without a change in energy, reproduced from Johns and Cunningham (1983).

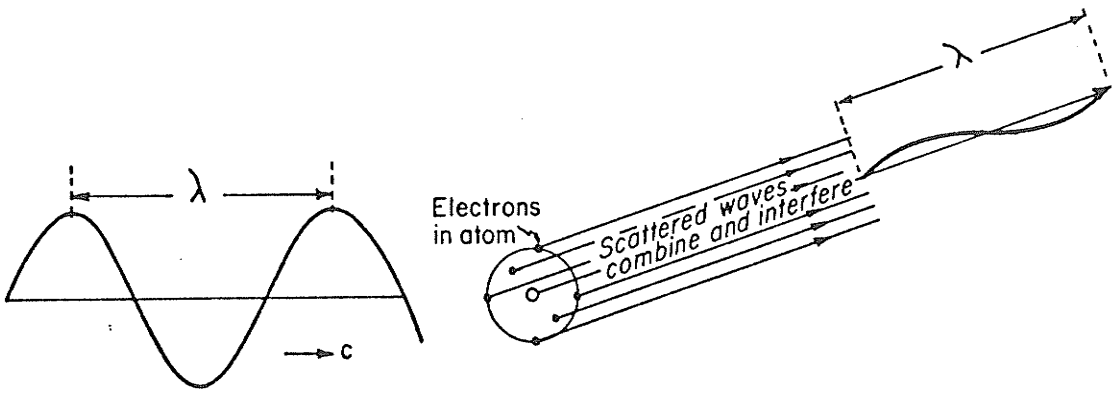
λ
c
Electrons
in atom
Scattered waves
combine and interfere
λ

Figure 3.5. The photoelectric effect. An incident photon is absorbed by an atom resulting in the ejection of a bound electron, reproduced from Johns and Cunningham (1983).

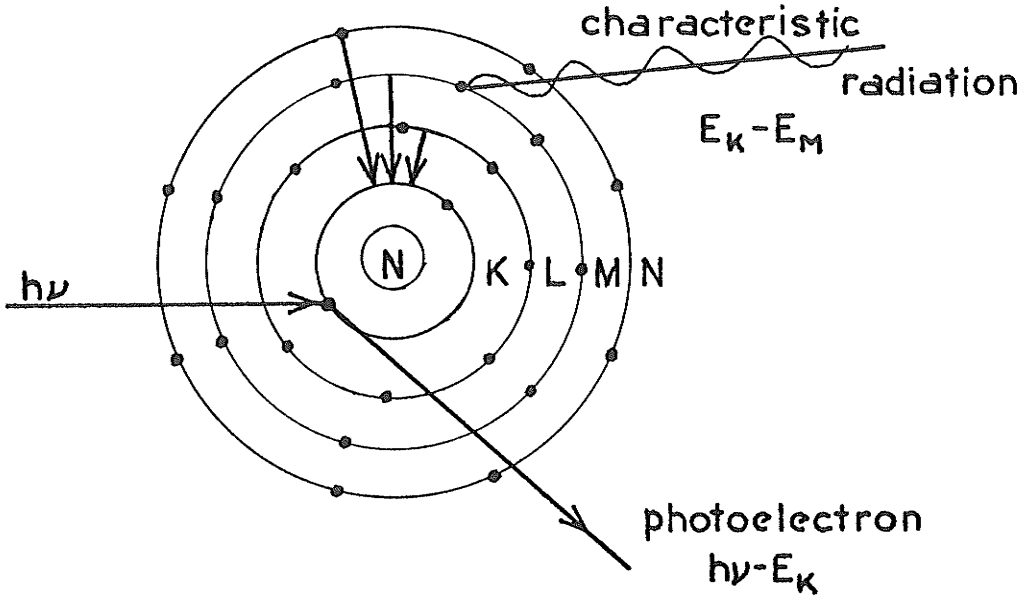
characteristic
radiation
$E_K - E_M$
N
K
L
M
N
$h\nu$
photoelectron
$h\nu - E_K$

The ejected electron emerges with an energy:

$$E = h\nu - E_B \qquad 3.18$$

where: $h\nu$ is the energy of the incident photon and E_B is the binding energy of the electron in the atom. The excited atom returns to ground state via emission of fluorescent radiation and electrons. Thus a photoelectric interaction can only occur if the energy of the incident photon is greater than the binding energy of the electron to be ejected. The ejected electron flies off predominantly sideways to the photon beam for $E<<0.5$ MeV. Because of the high photon momentum, the predominant direction is forward for higher energies. Following photoelectron emission a vacancy is created which is filled by transitions from other shells. The transitions result in the isotropic emission of photons called "characteristic" radiation of energies E_K-E_L, E_K-E_M, etc. Alternatively, in a process favored for low Z materials, an Auger electron may be ejected from the atom with energy E_M-E_L-E_M,in a case when the M shell is the less bound, for example.

The mass attenuation coefficient for photoelectric process, τ/ρ (cm^2/g), is a decreasing function of incident photon energy with discontinuities existing at the binding energies of different electron shells as shown in Fig.(3.6). The atomic photoelectric cross-

Figure 3.6. Photoelectric cross-sections for water and lead showing the discontinuities at the binding energies of different electron shells, Johns and Cunningham (1983).

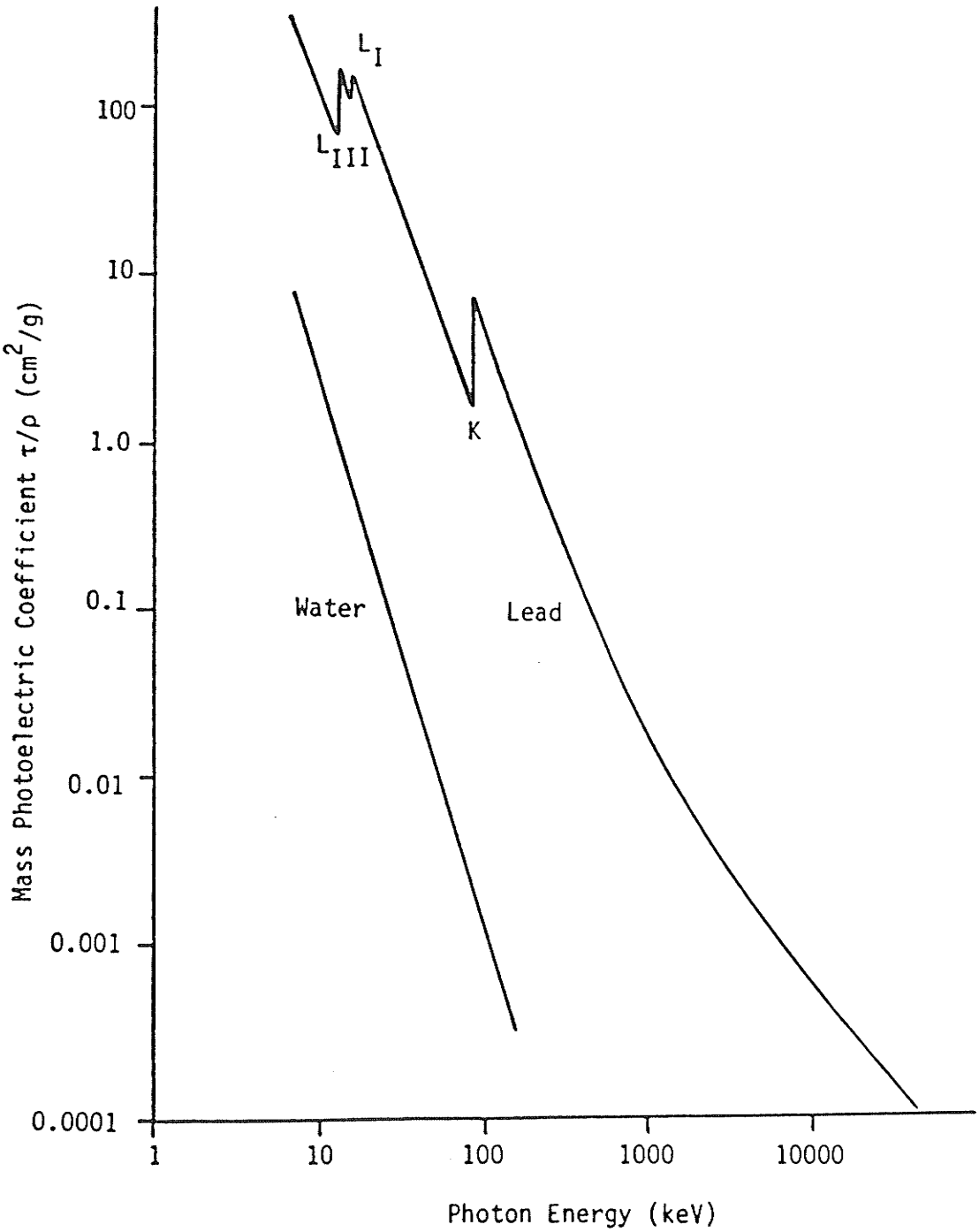
Mass Photoelectric Coefficient τ/ρ (cm²/g)
100
10
1.0
0.1
0.01
0.001
0.0001
1
10
100
1000
10000
Photon Energy (keV)
L_I
L_III
K
Water
Lead

section varies approximately as $1/(h\nu)^3$ for low energies and as $1/h\nu$ for high energies. The cross section per atom depends upon approximately Z^4 for high atomic number materials (f.e. lead) and on $Z^{4.8}$ for low Z materials. Since each atom contains Z electrons, the coefficient per electron depends upon Z^3 and $Z^{3.8}$ for high and low Z materials respectively. Since the number of electrons per gram is more or less independent of Z, the mass coefficients vary roughly as Z^3 and $Z^{3.8}$ for the two classes of materials. In the photoelectric process for low Z material the photoelectron acquires an energy approximately equal to the incident photon energy, since the binding energy for low Z materials is small. The resulting characteristic radiation is of low energy and is therefore absorbed locally. For high Z material the energy transfer to the photoelectron is small and the energy of the characteristic radiation is much greater in comparison to low Z materials, resulting in distant deposition of the characteristic radiation energy.

3.2.3. Compton scattering.

Compton scattering is an inelastic interaction between an incident photon and what is considered to be loosely bound(i.e.:virtually free) electron at rest in which the incident photon imparts some of its energy to the

electron, resulting in a scattered photon of reduced energy and an electron set in motion with some finite energy, as shown in Fig.(3.7). The energy taken up by the electron depends primarily on its recoil momentum. This effect predominates for the photon energies of interest in this work. In a first approximation the binding energy is taken to be negligible in comparison to the energy of the incident photon and the interaction is treated as being elastic. Thus the incident photon of energy, $h\nu$, is scattered at an angle, Θ, with energy, $h\nu'$ and a recoil electron is ejected at an angle, φ , with an energy, E. Applying conservation of energy and momentum to this situation yields the following relations between angle and energy for the scattered photon and recoil electron:

$$h\nu' = h\nu \frac{1}{1+\alpha(1-\cos\Theta)} \qquad 3.19$$

$$E = h\nu \frac{\alpha(1-\cos\Theta)}{1+\alpha(1-\cos\Theta)} \qquad 3.20$$

where: α is $= h\nu/m_o c^2$, m_o is rest mass of electron and

$$\cot\varphi = (1+\alpha)\tan(\Theta/2). \qquad 3.21$$

Maximum energy transfer occurs when $\Theta=180^\circ$ and $\Theta=0^\circ$.

Figure 3.7. Compton scattering,reproduced from Johns and Cunningham (1983).

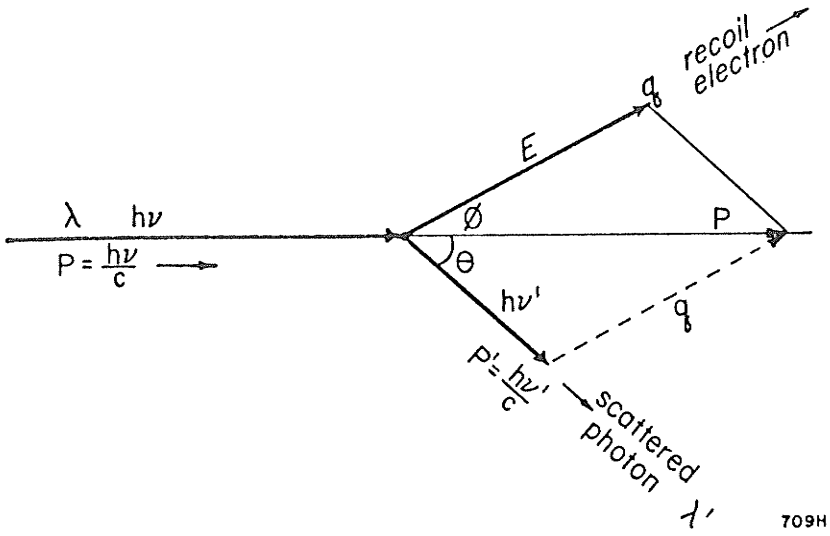
recoil electron
q_e
E
λ $h\nu$
$P = \frac{h\nu}{c}$
ϕ
P
θ
$h\nu'$
q_e
$P' = \frac{h\nu'}{c}$
scattered photon
λ'
709H

This condition yields:

$$h\nu'_{min} = h\nu \frac{1}{1+2\alpha} \qquad 3.22$$

$$E_{max} = h\nu \frac{2\alpha}{1+2\alpha} \quad . \qquad 3.23$$

The probability of photon scattering at an angle Θ is given by Klein Nishina formula. A graph of this equation - Fig.(3.8) for various photon energies illustrates preferred scattering in the forward directions for photon energies of interest in this work.

The total probability (total Compton coefficient) that a photon will interact with a free electron is given by:

$$e\sigma = 2\pi r^2 \left\{ \frac{1+\alpha}{\alpha^2} \left[\frac{2(1+\alpha)}{1+2\alpha} - \frac{\ln(1+2\alpha)}{\alpha} \right] + \right.$$

$$\left. + \frac{\ln(1+2\alpha)}{2\alpha} - \frac{1+3\alpha}{(1+2\alpha)^2} \right\} \frac{cm^2}{el} \qquad 3.24$$

where: r =2.81794x10^{-13}cm (the classical electron radius).

The total energy scattering cross section, $e\sigma_s$, which deals with the scattered photon energy $h\nu'$ is smaller than $e\sigma$ by:

$$e\sigma_s = \frac{h\nu'}{h\nu} e\sigma \quad . \qquad 3.25$$

The total energy transfer coefficient , $e\sigma_{tr}$, is given by:

$$e\sigma_{tr} = e\sigma - e\sigma_s \quad . \qquad 3.26$$

Figure 3.8. Klein-Nishina differential cross-section for various photon energies, Johns and Cunningham (1983).

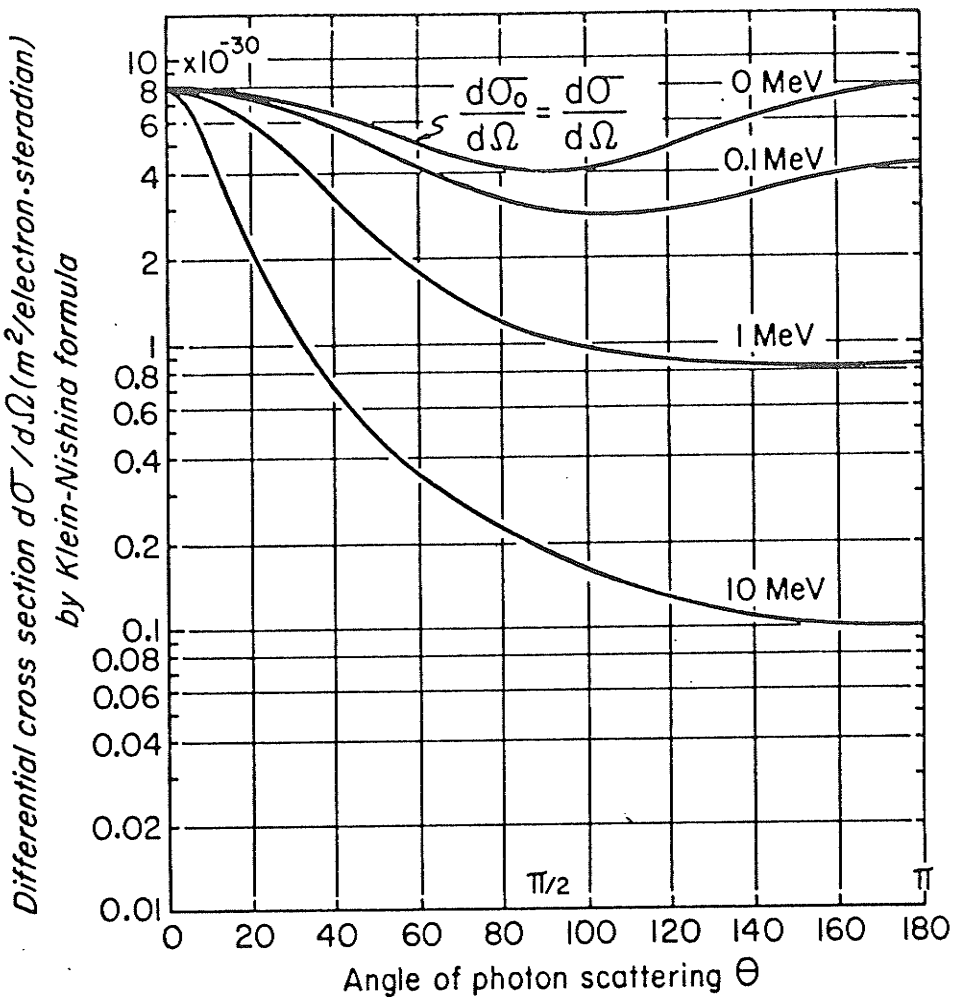
Differential cross section dσ/dΩ (m²/electron·steradian) by Klein-Nishina formula
x10⁻³⁰
10
8
6
4
2
1
0.8
0.6
0.4
0.2
0.1
0.08
0.06
0.04
0.02
0.01
dσ₀/dΩ = dσ/dΩ
0 MeV
0.1 MeV
1 MeV
10 MeV
π/2
π
0
20
40
60
80
100
120
140
160
180
Angle of photon scattering Θ

and represents the probability for the recoil kinetic energy, E, to be imparted to an electron in the course of a Compton collision. Fig.(3.9) shows the variation of $_e\sigma$, $_e\sigma_s$, $_e\sigma_{tr}$ with photon energy. The scatter coefficient, is equal to the total coefficient at photon energies less than 0.01 MeV, since at these energies the photon is scattered with nearly the same as the incident photon and the recoil electron gets little energy. At very high energies $_e\sigma_s << {}_e\sigma$ since at these energies the scattered photon gets very little energy. Since the Compton process involves free electrons and since most materials have approximately the same number of electrons per gram, the probability of a Compton interaction is independent of the atomic number Z. Hence all materials absorb essentially the same amount of radiation per electron and per gram from this process.

3.2.4. Electron-positron pair production.

In this effect, which predominates for high photon energies, especially in high Z materials , a photon disappears in the field of a charged particle and an electron positron pair appears, Fig.(3.10). A minimum incident photon energy $2\ m_o c^2$ or 1.022 MeV is required for pair production. The remaining energy $h\nu$ -1.022 MeV is shared between positron and electron. Pair production is

Figure 3.9. The total Compton coefficient, $_e\sigma$, the scatter coefficient, $_e\sigma_s$, and the transfer coefficient, $_e\sigma_{tr}$, as a function of photon energy, published by Hubbel, NBS (1986).

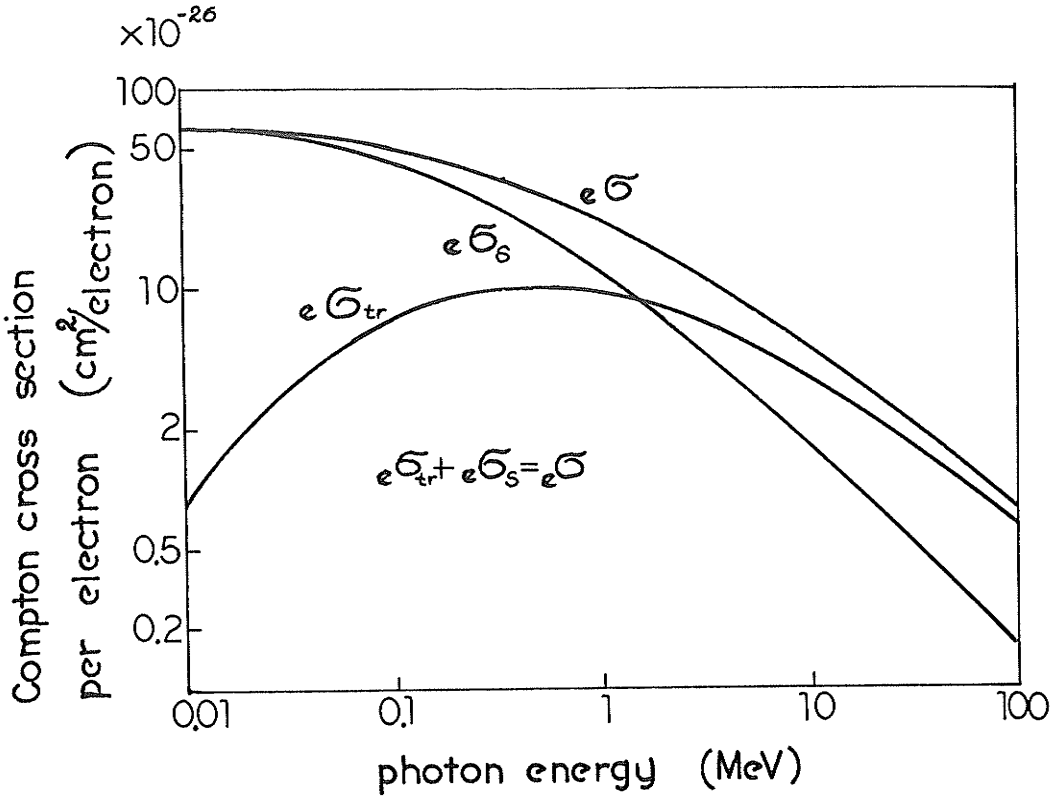
×10^-26
100
50
10
2
0.5
0.2
Compton cross section per electron (cm²/electron)
eσ
eσs
eσtr
eσtr+eσs=eσ
0.01
0.1
1
10
100
photon energy (MeV)

Figure 3.10. Pair production, reproduced from Johns and Cunningham (1983).

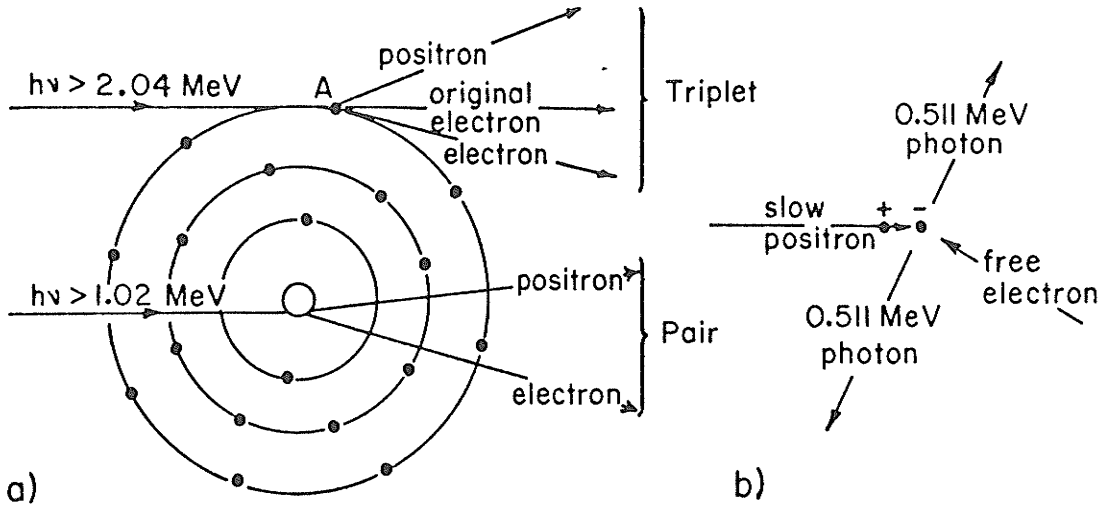
hν > 2.04 MeV
A
positron
original electron
electron
Triplet
hν > 1.02 MeV
positron
electron
Pair
a)
0.511 MeV photon
slow positron
+
-
free electron
0.511 MeV photon
b)

accompanied by the emission of annihilation radiation consisting of two 0.511 MeV photons ejected in essentially opposite direction, produced when a low energy positron combines with a free electron Fig.(3.10).

Triplet production may occur in the field of an orbital electron. This effect has a threshold of $4m_e c^2$ (=2.044 MeV) as required by the sharing, in this case, of the photon energy and momentum with the target electron as well as the created electron-positron pair. Fig.(3.11) illustrates the variation of pair and triplet production cross section, κ , with photon energy and atomic number Z.

3.2.5. Relative cross sections.

At any given incident photon energy a number of the above mentioned interaction processes may be taking place according to their relative probabilities. The total photon cross section at any given energy is the sum of the cross sections of each individual interaction taking place at that energy. Thus for the energy ranges employed in this work the total photon cross section, μ, may be expressed as:

$$\mu = \sigma_{coh} + \tau + \sigma_{inc} + \kappa \qquad 3.27$$

The relative significance of the three interactions (photoelectric, Compton and pair production) which transfer

Figure 3.11. Pair and triplet production cross section for various material as a function of photon energy, reproduced from Plechaty et al. (1975).

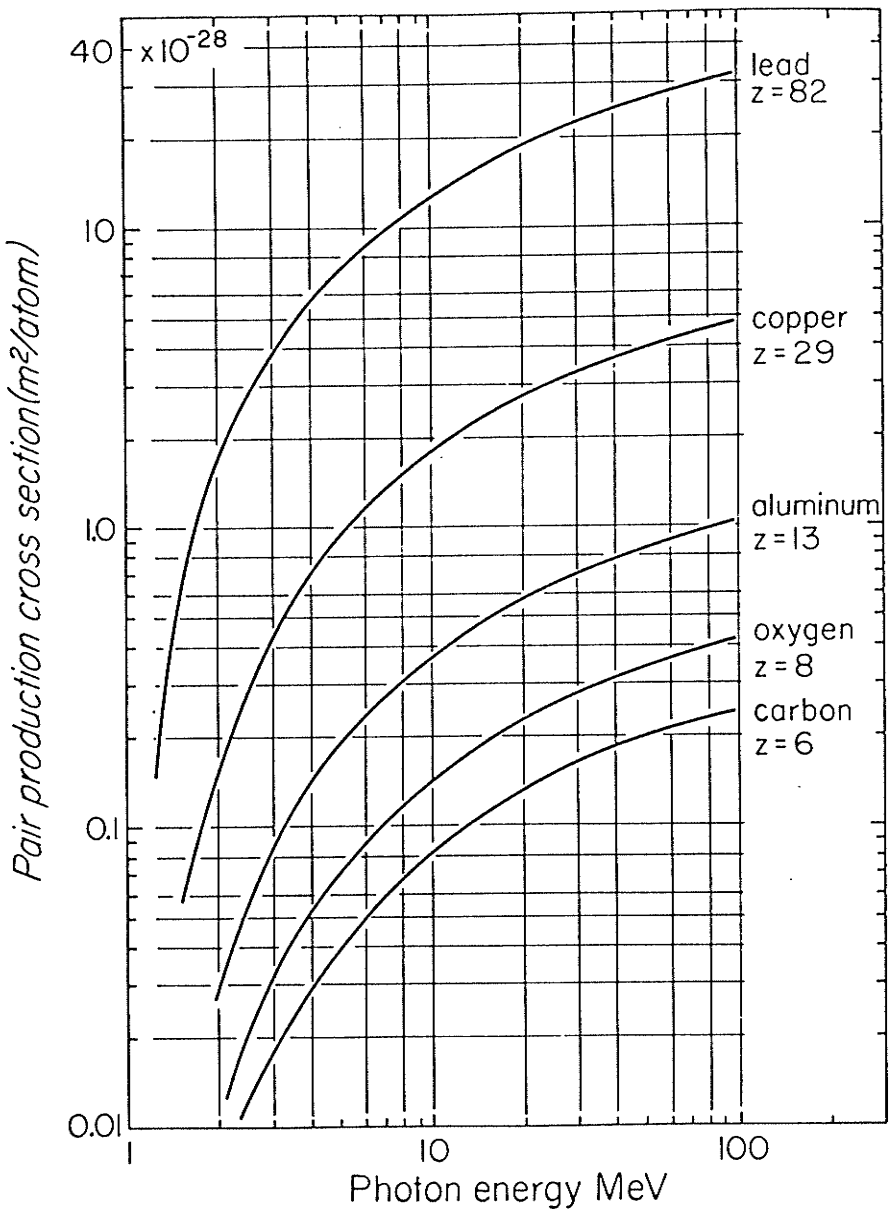
40
x10^-28
10
1.0
0.1
0.01
Pair production cross section(m²/atom)
lead
z = 82
copper
z = 29
aluminum
z = 13
oxygen
z = 8
carbon
z = 6
1
10
100
Photon energy MeV

energy from the x-ray beam to the attenuating medium are illustrated in Fig.(3.12). The total photon cross section σ_{tot} for lead, along with the individual interaction cross section of which it is composed are shown in Fig.(3.13).

Figure 3.12. Relative importance of the three principal photon interactions over a broad range of photon energies and absorbers, Evans (1955).

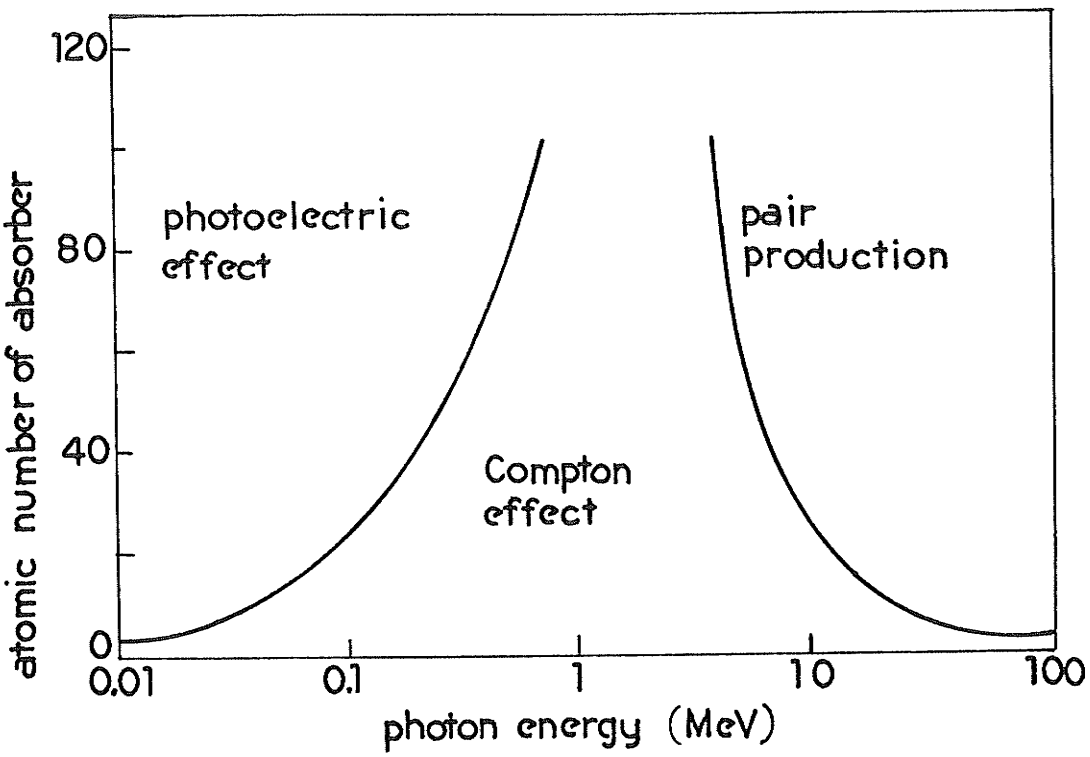
120
80
40
0
atomic number of absorber
photoelectric
effect
Compton
effect
pair
production
0.01
0.1
1
10
100
photon energy (MeV)

Figure 3.13. Photon interaction cross sections for lead, reproduced from Robinson (1986).

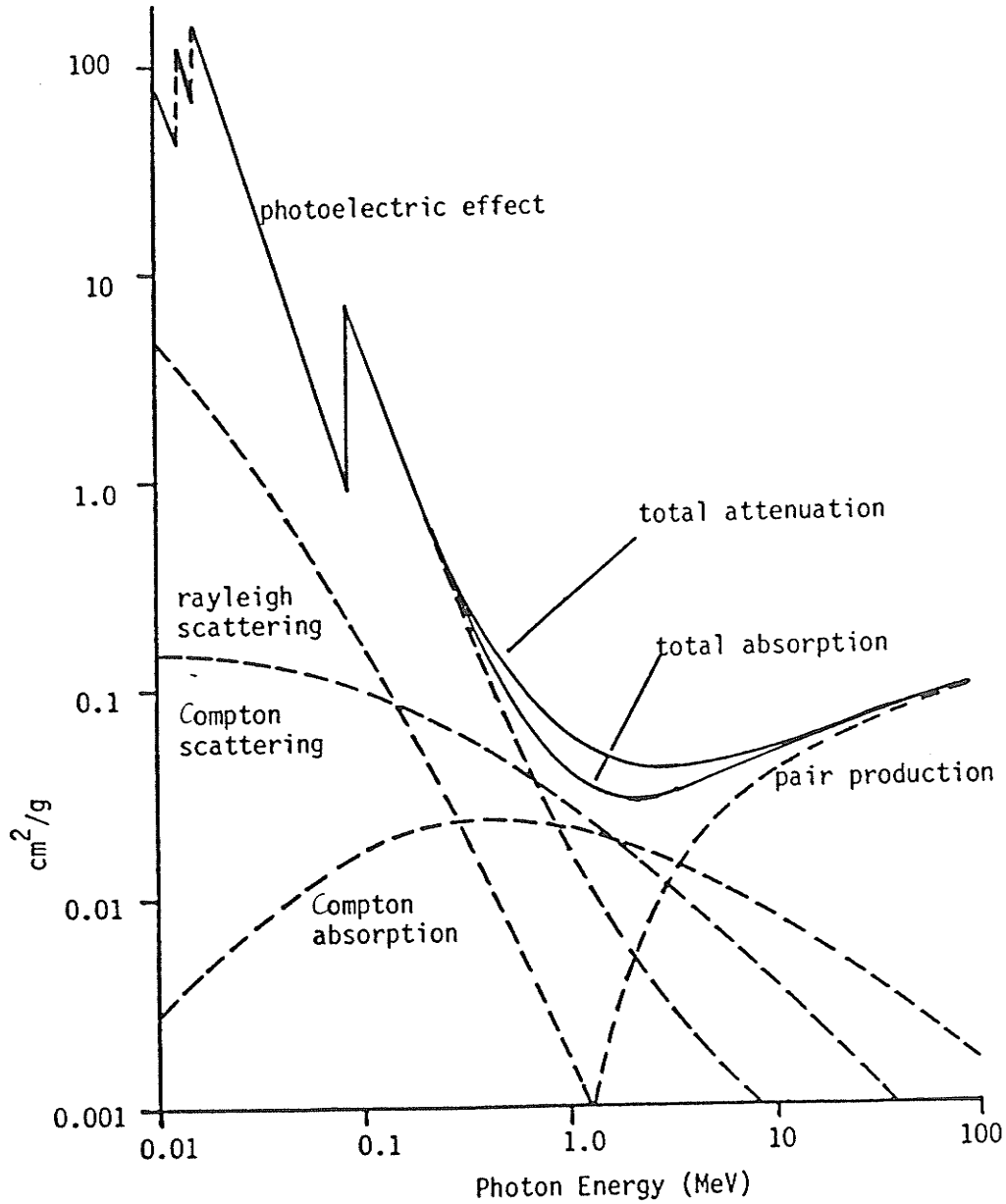
100
10
1.0
0.1
0.01
0.001
cm²/g
photoelectric effect
total attenuation
total absorption
rayleigh scattering
Compton scattering
pair production
Compton absorption
0.01
0.1
1.0
10
100
Photon Energy (MeV)

IV. DOSIMETRY

In radiotherapy a quantity of great interest is that of the absorbed dose. The absorbed dose from a beam of incident radiation is defined as being the energy absorbed from the radiation beam per unit mass of absorbing medium.

Absorbed dose is defined as :

$$D = \Delta E / \Delta m \qquad 4.1$$

The SI unit for absorbed dose is the Gray (Gy) and is defined as:

$$1Gy = 1J/kg$$

The only absolute method of measuring absorbed dose is by calorimetry in which the rise in temperature of an isolated mass of the medium is measured.

4.1. Cavity theory.

Most absorbed dose measurements made today are based on a measurement of ionization followed by calculations involving a number of corrections factors. These factors are derived from Bragg-Gray cavity theory, presented by Gray (1929, 1936). The Bragg-Gray equation relates the absorbed dose in a cavity gas to the absorbed dose in a surrounding medium, in terms of the ratio of the mean collision mass stopping powers:

$$\frac{D_{med}}{D_{gas}} = \frac{(\bar{S}/\rho)_{med}}{(\bar{S}/\rho)_{gas}} = \left(\frac{\bar{S}}{\rho}\right)^{med}_{gas} \qquad 4.2$$

While there are certain special cases in which this equation may be an adequate approximation, in general the ratio D_{med}/D_{gas} depends in a complicated manner on the spatial gradient of the primary photon or electron field, the energy of the secondary electrons, the atomic number of the cavity gas and the wall material, the shape of the cavity, and the pressure and size of the cavity gas.

The Bragg-Gray formulation of cavity theory makes the following assumptions;

i) the size of a the cavity is small in that its dimensions are much less than the range of secondary electrons in the medium

ii) the introduction of the cavity to the medium does not perturb the medium's spectrum of secondary electrons

iii) photon attenuation is negligeable over the dimensions of the cavity, and hence secondary electrons in the cavity are due to photon interactions in the medium surrounding the cavity

iv) the primary photon fluence in the region surrounding the cavity from which secondary electrons generated in the medium may enter the

cavity is isotropic

v) seccondary electrons lose energy continuosly.

Some modification of this theory is required. While there is no fully rigorous theory of cavity ionization, the Spencer-Attix theory is widely used. In this theory, the effects of large, discrete energy losses by electrons are considered. The effect of δ-ray production has been taken into account by Spencer and Attix (1955) by employing the restricted stopping power $\bar{L}$ in place of unrestricted stopping power $\bar{S}$.

The Spencer-Attix formulation can be expressed in the general form :

$$\frac{D_{med.}}{D_{gas}} = \left(\frac{\bar{L}}{\rho}\right)^{med.}_{gas} \qquad 4.3$$

where $\bar{L}/\rho$ represents the restricted mean mass collision stopping power, averaged over the electron slowing-down spectrum in the wall material. Whereas the Bragg-Gray formulation of cavity theory uses unrestricted stopping powers averaged over the slowing-down spectrum of only the primary electrons, the Spencer-Attix formulation uses restricted stopping powers averaged over the slowing-down spectrum of all generations of electrons. The absorbed dose to the gas is simply:

$$D_{gas} = J_{gas}\,(W/e)_{gas} \qquad 4.4$$

where J_{gas} is the charge per unit mass of gas in the ca-

vity, and $(W/e)_{gas}$ is the mean energy expended in the gas per unit charge of ionization.

For both photon and electron beams, this schematization contains the assumption

i) that the spectral distribution of electron fluence in the medium adjacent to the cavity is not changed by the presence of the cavity. For photon beams, the further assumptions are made

ii) that photon interactions that generate electrons in the cavity can be neglected, and

iii) that the primary photon fluence is uniform through out the region in the medium from which secondary electrons can reach the cavity.

Practical ionization chambers, however, perturb the photon and electron fluence in various ways that must be accounted for by certain correction factors. Thus, a general relationship between dose to gas in the chamber and dose to medium that replaces the chamber when it is removed is given by:

$$\frac{D_{med.}}{D_{gas}} = \left(\frac{\bar{L}}{\rho}\right)_{gas}^{med.} P_{ion} P_{repl} P_{wall} \qquad 4.5$$

$P_{ion.}$ is a factor that corrects for ion recombination. $P_{repl.}$ is a replacement correction which depends upon the type and energy of the radiation, the gradient of the depth-dose curve at the point at which the measurement is made, and the radius of the chamber's air cavity, P_{wall} is

a correction factor which corrects for the attenuation and multiple scattering of primary photons in the chamber wall, and the buildup cap used to establish charged particle equilibrium. Hence if one can measure the absorbed dose in the cavity then one can determine the absorbed dose to the volume of medium displaced by the cavity.

4.2. Dosimetric functions.

Of prime concern in radiotherapy is the absorbed dose in tissue in an irradiated volume. Much experimental work has been performed with materials which absorb and scatter radiation in a similar manner to tissue. The requirements of such phantom materials according to the ICRU report # 24 (1976), are that it be " a volume of tissue-equivalent material, usually large enough to provide full scatter conditions for the beam being used" where a tissue-equivalent material is a "material whose absorption and scattering properties for a given irradiation simulate, as nearly as possible, those of a given biological material, such as soft tissue, muscle, bone or fat".

The absorbed dose at any point in a phantom is the result

of two components. The first component is the dose due to primary radiation and the second component is the dose due to scattered radiation. Both are functions of the physical parameters of the radiation beam and the parameters of the physical geometry. The dose to a given point at a depth below the phantom surface will be a function of field size, distance from the source, energy of the radiation beam and depth in tissue. With this in mind certain relationship have been developed to describe the absorbed dose as a function of these parameters.

To relate absorbed dose at a point in a phantom to the dose measured in air two quantities, tissue-air ratio, TAR, and scatter-air ratio, SAR, have been defined. TAR has been defined by the International Commission on Radiological Units ICRU (1963), as the ratio of the absorbed dose at a given point in a phantom to the absorbed dose which would be measured at the same point in free air within a volume of the phantom material just large enough to provide maximum electronic buildup at the point of measurement".

This situation can be explained by referring to Fig.(4.1). The diagram on the left depicts a radiation beam irradiating a water phantom and a dosimeter is placed at point X on the axis of the beam. For the diagram on the right all irradiation conditions

Figure 4.1. Diagram illustrating the meaning of tissue-air ratio, which is the ratio formed by a dosimeter reading at X (in a water phantom) divided by its reading at the same point, X', but in air, reproduced from Bleehen (1983).

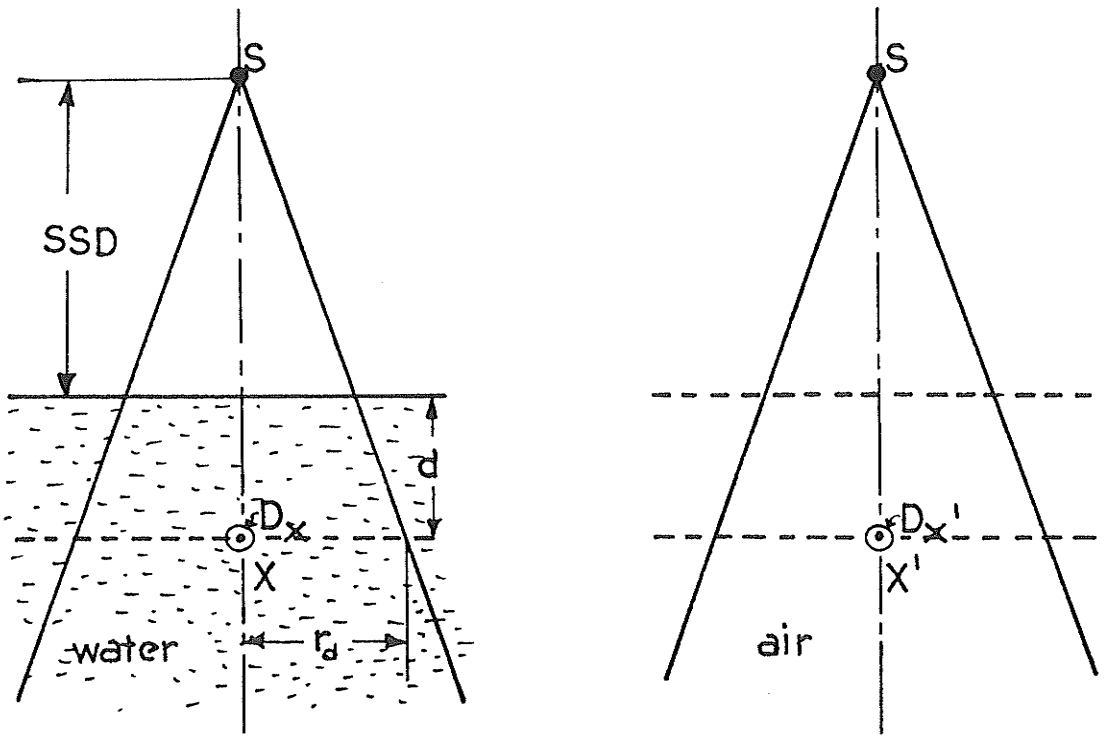
S
SSD
d
D_x
X
water
r_d
S
$D_{x'}$
X'
air

(collimator adjustment, distance from the source, flattening filter etc.) are the same except that there is no water present, and the dosimeter, at the same location but now designated by X', is in air and is far from any scattering material. The tissue-air ratio, TAR is:

$$TAR(d, Wd, E) = Dx/Dx.' \qquad 4.6$$

The values of Dx and Dx' should be obtained considering all the conversion factors, but in practice, it is generally assumed that cancellations may take place leaving only the ratio of instrument readings. The TAR describes the combined effects on the beam of attenuation and scatter. Fig.(4.2) shows TAR dependence on field size and depth in a phantom. The two effects may be separated by the following procedure. Consider the TAR as function of cross-sectional area. If the area were reduced so as to approach zero, the scattering volume would approach zero and only the attenuation of the primary would remain. The scatter component for a beam of finite size would then be:

$$SAR(d, r_d) = TAR(d, r_d) - TAR(d, 0). \qquad 4.7$$

TAR(d, 0) is called zero area TAR and it can not be measured directly. It can be obtained by measuring tissue-air ratio for beams with field dimensions approaching zero and then extrapolating to zero.

Figure 4.2. Graphs showing the dependence of tissue-air ratio on field size (radius) and depth, reproduced from Bleehen (1983).

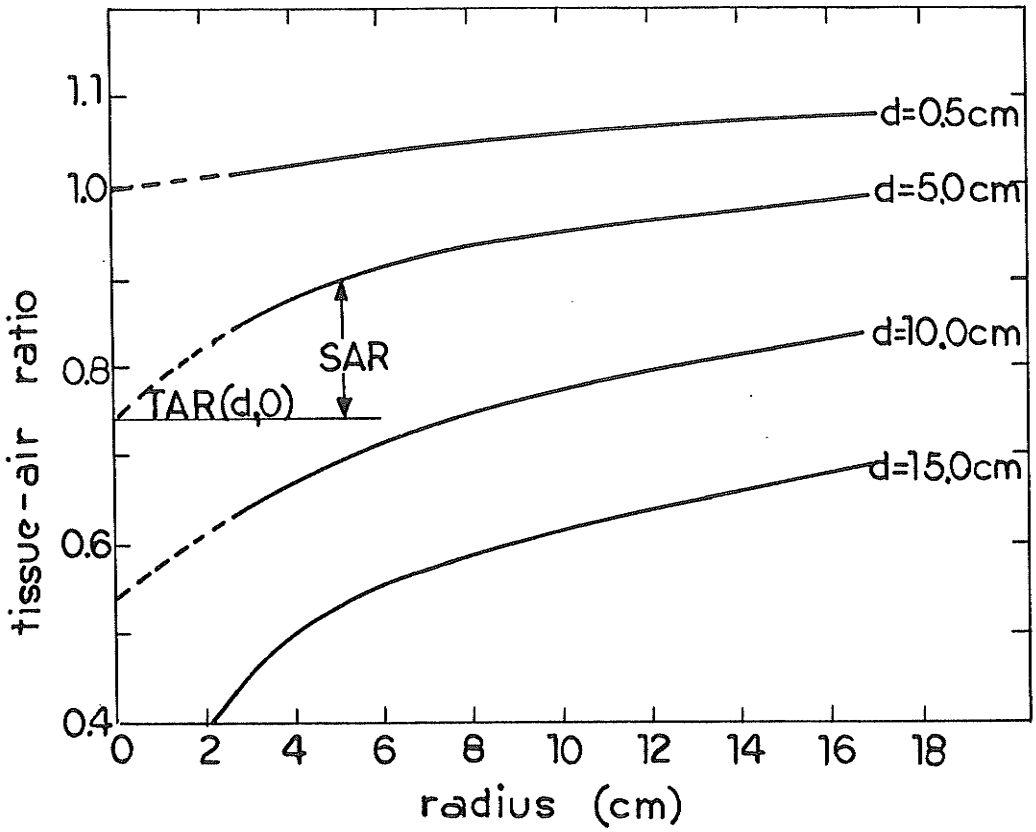
1.1
1.0
0.8
0.6
0.4
tissue-air ratio
d=0.5cm
d=5.0cm
d=10.0cm
d=15.0cm
SAR
TAR(d,0)
0
2
4
6
8
10
12
14
16
18
radius (cm)

SARs are primarily of interest for computational work, since they permit the calculation of the dose at any point in any shaped field. The calculational method was developed by Clarkson (1941) and further developed by Aspin et al. (1961) and Gupta and Cunningham (1966). Scatter-air ratios can be determined from measurements and can be tabulated as a means of describing radiation scattered within an irradiated volume. Their use can be illustrated by referring to Fig.(4.3). This diagram shows a cross-section of a radiation beam. Point P is a point somewhere within the beam. The cross-hatched region is a sector of a circle with radius, r_1. The amount of scattered radiation reaching point P from this sector can be taken as $S(d, r_1)(\Delta\theta/2\pi)$, where $\Delta\theta$ is the angular width of the sector. This would be exactly equal to the scattered radiation reaching P from the sector of the circular beam of radius r_1 shown by the dashed circle. The whole irradiated volume can be covered by a series of such sectors and the total dose due to scatter at point P would be:

$$D_S = D_A(d)\sum_{i=1}^{n} S(d, r_i)\ \frac{\Delta\theta_i}{2\pi} \qquad 4.8$$

The use of sectors of circular radiation beams to represent components of other beams involves at least four simplifying assumptions:

i) the scattered radiation from each sector to point, P

Figure 4.3. Cross section of a radiation beam,illustrating the sector integration method of calculating the dose due to scattered radiation at points either in or out of the beam, reproduced from Bleehen (1983).

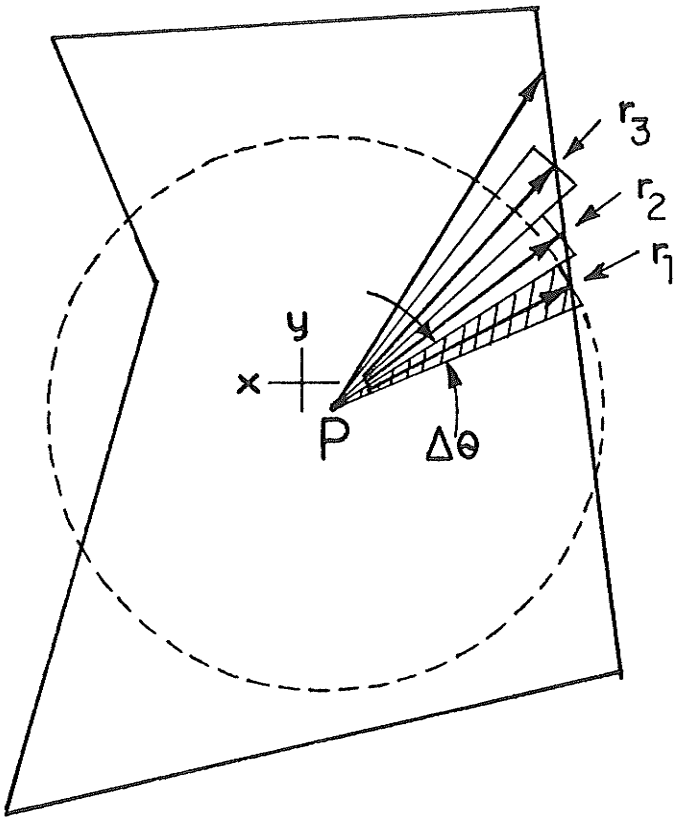
r3
r2
r1
y
x
P
Δθ

same in the circular beam as it is in the actual beam.

This will be true except for multiply scattered radiation and will tend to balance out for most locations.

ii) it is assumed that the surface of the irradiated phantom is at right angles to the ray from the source to the point of calculation.

This will not be true for points near an edge of the beam.

iii) it is assumed that the radiation field is uniform across the sector, and finally

iv) that the edge of the beam in which calculations are being made is similar in shape to that of the beam in which the scatter-air-ratios were measured.

Such a method based on such sector integration will be used to calculate the scatter component of the transmitted fraction of photons passing through lead attenuators.

V. DOSE MODIFICATION BY LEAD FILTERS

5.1. Introduction.

The beam modifying devices alter the dose distributions by removing some of the incident primary photons . In doing so, at photon energies where the Compton effect is the dominant interaction process, the beam modifying filter also produces scattered radiations; secondary electrons and scattered photons thus impinge on the patient. The electrons compromise the skin sparing characteristics of the beam, while the presence of scattered photons may complicate the design of wedges or compensators as well as subsequent calculations of dose distributions.

5.2. The theoretical considerations.

The total dose to a point in a phantom consists of the primary dose, single scatter dose and multiple scatter dose. The relative contribution of each component to a total dose depends on the radiation energy, the geometry of irradiation and depth in a phantom. The primary and first scattered radiation account for a large proportion of the total dose as has been shown by Padikal and Deye (1978) with Monte Carlo calculations. In the theoretical model due to El-Khatib (1986) which is presented below only first order Compton scattering is accounted for in

the calculations.

For a parallel beam of monoenergetic photons with an energy, E, incident on a homogeneous phantom the dose D(P) at point P due to primary radiation is given by:

$$D_p(P) = \Phi E_o (\mu_{ab}/\rho)_p \, e^{-\mu_o d} \qquad 5.1$$

where: d is the depth in phantom, Φ is the photon fluence in vacuum at point, P, μ_{ab}/ρ is the mass energy absorption coefficient for the primary photons in the phantom material and μ_o is the narrow beam linear attenuation coefficient for the phantom material at photon energy E_o.

The first scatter dose at point P in a homogeneous phantom due to once scattered photons coming from all surrounding elements in the radiation field is given by (in a spherical coordinate system and for a circular radiation field - as shown on Fig. (5.1)):

$$D_s(P) = 2\pi n_e \Phi e^{-\mu_o d} \int_0^{\pi} \int_0^{R(\theta)} E_s (\mu_{ab}/\rho)_s \sin\theta \frac{d\sigma}{d\Omega} \qquad 5.2.$$

$$* \exp\{r[\mu_o \cos\theta - \mu_s]\} \, dr \, d\theta$$

Figure 5.1. Geometry used for the calculation of primary and first scatter dose to point, P, from three separate layers (lead,air,water) in a divergent beam, reproduced from El-Khatib (1986).

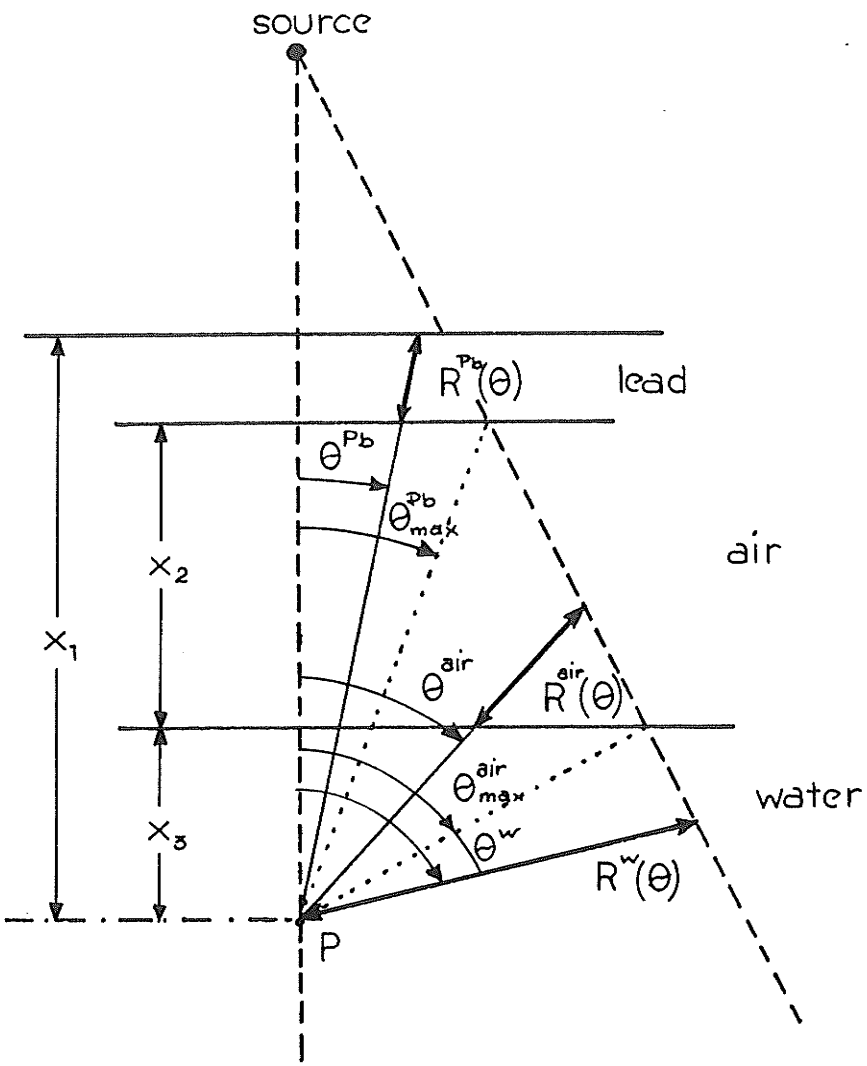
source
lead
air
water
P
$R^{Pb}(\theta)$
θ^{Pb}
θ^{Pb}_{max}
θ^{air}
$R^{air}(\theta)$
θ^{air}_{max}
θ^{w}
$R^{w}(\theta)$
X_1
X_2
X_3

where: θ is the scattering angle, $d\sigma/d\Omega$ is the differential Compton cross - section per unit solid angle (cm^2 / electron), E_s is the energy of the scattered photon, n_e is the electron density of the phantom material (electrons /cm^3), $(\mu_{ab}/\rho)_s$ is the mass energy absorption coefficient for once scattered photons in the phantom material, μ_s is the linear attenuation coefficient for first scattered photons in the phantom material and $R(\theta)$ is the radial distance from P to the edge of the phantom or the geometric edge of the beam.

Integrating equation (5.2) over r gives :

$$D_s(P) = 2\pi n_e \Phi e^{-\mu_o d} \int_0^{\pi} E_s (\mu_{ab}/\rho) \sin\theta \frac{d\sigma}{d\Omega} \times \frac{\exp\left[R(\theta)(\mu_o \cos\theta - \mu_s)\right]}{\mu_o \cos\theta - \mu_s} \qquad 5.3$$

In typical treatment conditions one has to consider the radiation transmitted through and scattered from three separate layers of media such as the attenuator, the air gap and the phantom.

The primary dose to a point P in phantom is given by:

$$D_p(P) = \Phi E_o (\mu_{ab}/\rho)_p^w \times \exp\left[-\mu_p^{Pb}(x_1 - x_2 - x_3) - \mu_p^{air} x_2 - \mu_p^w x_3\right] \qquad 5.4$$

where: x_1, x_2, x_3 are defined in Fig.(5.1) and μ_p^{Pb}, μ_p^{air} and μ_p^{w} represent the primary beam linear attenuation coefficient for lead, air and water respectively.

The first scatter doses contributed to point P in a unit density phantom by the three layers are:

$$D_s^{Pb} = 2\pi \eta_e^{Pb} \Phi \exp\left\{-\mu_p^{Pb}[x_1 - x_2 - x_3]\right\} \int_0^{\theta_{max}^{Pb}} E_s \left(\frac{\mu_{ab}}{\rho}\right)_s^{w} \sin\theta \frac{d\sigma}{d\Omega}$$

$$\times \exp\left\{-\frac{\mu_s^{air} x_2 + \mu_s^{w} x_3}{\cos\theta}\right\} \frac{\exp\left\{R^{Pb}(\theta)\left[\mu_p^{Pb}\cos\theta - \mu_s^{Pb}\right]\right\} - 1}{\left(\mu_p^{Pb}\cos\theta - \mu_s^{Pb}\right)} d\theta \qquad 5.5$$

$$D_s^{air} = 2\pi \eta_e^{air} \Phi \exp\left\{-\mu_p^{Pb}[x_1 - x_2 - x_3] - \mu_p^{air} x_2\right\} \int_0^{\theta_{max}^{air}} E_s \left(\frac{\mu_{ab}}{\rho}\right)_s^{w} \sin\theta \frac{d\sigma}{d\Omega}$$

$$\times \exp\left\{\frac{\mu_s^{w} x_3}{\cos\theta}\right\} \frac{\exp\left\{R^{air}(\theta)\left[\mu_p^{air}\cos\theta - \mu_s^{air}\right]\right\} - 1}{\left(\mu_p^{air}\cos\theta - \mu_s^{air}\right)} d\theta \qquad 5.6$$

$$D_s^{w} = 2\pi \eta_e^{w} \Phi \exp\left\{-\mu_p^{Pb}\left[x_1 - x_2 - x_3\right] - \mu_p^{air} x_2 - \mu_p^{w} x_3\right\} \times \qquad 5.7$$

$$\times \int_0^{\pi} E_s \left(\mu_{ab}/\rho\right)_s^{w} \sin\theta \frac{d\sigma}{d\Omega} \frac{\exp\left\{R^{w}(\theta)\left[\mu_p^{w}\cos\theta - \mu_s^{w}\right]\right\} - 1}{\left(\mu_p^{w}\cos\theta - \mu_s^{w}\right)} d\theta$$

The total dose at point, P, in the water phantom accounting for the primary beam attenuation and first scatter from the various layers of the phantom is:

$$D(P) = D_p(P) + D_s^{Pb}(P) + D_s^{air}(P) + D_s^{w}(P) \qquad 5.8$$

Using the above equations to calculate the dose to a point when a beam modifier is used and for an open beam one should be able to predict the transmitted fraction of primary photons through the attenuator for any therapeutic geometry. The transmitted fractions are essentially correction factors to be applied to the dose at point P in the phantom measured without attenuators to get the dose to the same point P when an attenuator of a given thickness is inserted into the radiation beam. The transmitted fraction can be easily measured for different geometrical setups and such measurements will provide a very good tool to test the accuracy of the calculated dose using the calculational method described above. In the recently published paper by El-Khatib (1986) an algorithm was presented based on this theoretical model to calculate analytically the radiation transmitted through and scattered from three separate layers of media in a divergent radiation beam. The three layers represent the attenuator, the air gap and the unit density phantom. The "broad" and "narrow" beam transmission

through lead filters for different thickness of attenuator, field size and depth in tissue for Co-60, 4 MV, 6 MV and 10 MV x-rays was studied. The results of these measurements were compared to the calculated dose ratios for the same experimental conditions. Based on the calculations two conclusions can be made; first that the transmission curves are pure exponentials for all field sizes and depths of measurement and second that at a given depth in the phantom the slope of the transmission curve depends on the field size, a larger field giving a more penetrating beam because of an increase in scattering contributions from the attenuator to the point of measurement. The measured data agree quite well with the calculated ones with two exceptions.

First for narrow radiation beams the slope of the measured transmission curve does depend on the depth of measurement in the phantom, and second the deviation from narrow beam geometry for large fields is larger for the measured data than for the calculated curves. The first effect has been explained by Rogers et al. (1984) by the fact that the narrow Cobalt-60 beam contains, in addition to monoenergetic 1.25 MeV photons, some lower energy photons originating in the source capsule and the collimator. The lead filter and phantom preferentially attenuate these low energy photons and consequently

harden the beam, making the transmission curve measured at large phantom depths more penetrating. The calculation assumes a monoenergetic spectrum and therefore does not predict this effect. For large fields this beam hardening effect is less pronounced because it is counterbalanced by an increased contribution of the low energy photons scattered from the attenuator to the dose measured at shallow phantom depths, which brings the slope of the transmission curve for shallow depth closer to the slope measured at larger depths. The discrepancy between calculated and measured transmission curves for large radiation fields is due to neglecting the multiple scattering in the calculations . Calculated and measured transmission curves in lead for 4 MV x-rays revealed that both the narrow and the broad beam undergo beam hardening effects, causing the slope of the transmission curve to become less steep as the lead thickness increases. The calculations based on 4 MV spectrum obtained by Mohan (1985) give the transmission curves which agree to within 2% with the measured data, properly predicting the field size dependence and the hardening effect. The good agreement between calculated and measured transmission curves for 4 MV x rays can be mainly attributed to the incorporation in the calculations the beam hardening effects which predict well the depth dependence for a

given field size.

Since the major portion of the total dose to a point in the tissue consists of primary and first scatter dose, analytical calculations like these give a good description of any changes in dose to the point due to the beam alteration by beam modifying devices. For larger field sizes the calculations are less accurate because of the increased contribution of multiple scattering as pointed out by El-Khatib et al. (1986). Accurate predictions of the dose in a phantom for various lead thicknesses and parameters of the beam as well as the phantom can only be achieved with Monte Carlo calculations which are both complicated and time consuming. The Electron Gamma Shower Monte Carlo method can take into account most of the physics required for the energies of interest, Rogers and Bielajew (1984): the photon interactions which can be treated are Rayleigh scattering, photoelectric effect, Compton scattering and pair and triplet production; the charged particle interactions which can be accounted for are multiple scattering, Moller scattering for electrons, Bhabha scattering for positrons; the continuous slowing down approximation, positron annihilation and bremsstrahlung. While the EGS calculation will produce by far the most accurate results, the computation time required (for example one point requires an average computation

time of about 20 CPU hours on VAX 11/780 computer) will limit the use of this method for practical calculation in treatment planning.

5.3. X-ray dose calculation - practical methods.

A number of different methods for the calculation of dose in a radiation beam is available. The calculational algorithm chosen for computer planning procedures should be sufficiently general to allow calculations to be made for rather generalized beam conditions. It should be possible to calculate accurately the dose at any point when beam shaping devices such as compensators, wedges or blocks are introduced into the beam. When a beam modifying filter is placed in an X-ray beam, the characteristics of the beam change because of scattered photons produced in the filter. This effect should be considered in dose calculations.

Any calculational method for such cases will involve the introduction of some correction factors. The transmitted fraction of photons through the attenuator which is defined as:

$$TR = e^{-\mu t} \qquad 5.9$$

where: μ is beam attenuation coefficient and t is thickness of the portion of the attenuator and TR can be considered as such a correction factor. It is to be applied to the dose at a point in a phantom measured without an attenuator to get the dose to the same point when the attenuator of thickness, t , is in the radiation beam. The use of a narrow beam attenuation coefficient in the calculation of TR leads to errors in the delivered dose as high as 26%, van Dyk (1986). The magnitude of such errors will be dependent on the geometry and the amount of attenuator in the beam. Broad beam geometries which apply in radiotherapy are complicated by radiation that is scattered from the absorber and reaches the detector. The attenuation of the primary radiation component follows the narrow beam exponential decrease, the scatter component, however is hard to predict theoretically since it depends in a complicated fashion on the properties of the beam, the phantom and the attenuator. Generally therefore the transmitted fraction, TR, measured for a given attenuating material is dependent on beam field size, thickness of attenuator and energy of impinging photons. The field size dependence of the transmitted fraction of the high energy photons through lead absorbers is well known and has been considered by Fano (1953), Berger and Dogget (1956), Peebles et al.

(1951) and Maruyama et al. (1971) for radiation protection purposes. However, there is very little quantitative data for therapeutic geometries. J.van Dyk (1986) performed an experimental and theoretical study of the effect of broad beam attenuation in lead, measured in air for Cobalt-60 and at depth of 5 cm in a water phantom for 6, 18 and 25 MV x-rays. Measured attenuation coefficients for broad beam geometries, for a 40x40 cm^2 field, approximating some treatment conditions, were found to deviate between 14% and 16%, depending on energy, from the narrow beam geometry. The theoretical calculations were based on first-scatter considerations and indicated a dependence on treatment geometry. To deal with the irregular fields the sector integration method, as outlined by Cunningham et al. (1972) and described by equation 4.8 was employed. For a long rectangular field the agreement between measured and calculated attenuation coefficients was better than 1.5% for all energies. This calculation does not account for variation in absorber thickness throughout the beam. Further refinement can be made to that methodology to allow for more general cases when only part of a beam is shielded or the thickness of the absorber throughout the beam varies. In such case, the sectors should be subdivided such that only the scatter from the appro-

priate absorber thickness is included in the calculations. The effects on dose of scattered photons generated in copper filters have been studied by P.H.Huang et al.(1986) on a 4MV x-ray beam in air for therapeutic geometries. An experimental and analytical technique was developed for obtaining quantitative information about scattered photons from beam modifying filters. The influence of filter thickness, field size, distance from the filter and off-axis position were investigated. Their experimental results showed that the narrow beam effective attenuation coefficient decreases slightly as the thickness of the attenuating filter increases, reflecting the progressive hardening of the x-ray beam, and that the broad beam attenuation coefficient, μ_{eq} decreases drastically as the field size increases. When other conditions remain constant, a shorter filter-detector distance results in smaller values of μ_{eq}. The results indicate that the dose contribution from the scattered photons produced in the filter is greater for a larger field size and a shorter filter-detector distance. For large source to surface distances the field size dependence on the effective attenuation coefficient is less pronounced. The narrow beam attenuation coefficient, μ_o, measured at different off-axis positions indicates that the quality of the 4 MV x-ray beam is

relatively constant from the central axis to 5^{o} off-axis. At larger angles, the beam gradually becomes softer and hence μ_o increases toward the edges of the field, in agreement with the difference between the central axis and off-axis energy spectra, reported by Huang et al. (1983). The finite beam effective attenuation coefficient, μ_{eff}, measured across a large field (30x30 cm^2) in the isocentric plane increases more rapidly with the distance from the central axis than, μ_o, which means that more scattered photons from the filter are present on the central axis than at off-axis positions. The measured effective attenuation coefficient for a particular field size was used to generate the thickness profiles of the wedges, and a good agreement between the calculated and measured isodoses in water for a 10x10 cm^2 field size was achieved. Although a good agreement with experimental results was found, the use of one effective attenuation coefficient value in dose distribution calculation will still give some errors for other field sizes or different thicknesses of the attenuator. One method proposed by Huang et al. (1986) to avoid such errors is to introduce a correction factor. When wedges are used clinically, isodose curves normalized to the value at some reference point are employed; to transform these relative data to absolute doses, a calcu-

lation is made for the absorbed dose at the reference point by using the "wedge factor" , which is the ratio of the measured doses at a reference point with and without the wedge. The "wedge factor" is a function of the beam parameters, especially field size. To avoid large errors the authors suggest that field size dependent "wedge factors" should be used in dose calculations. Similarly the concept of a field size dependent "compensator factor" for compensators was introduced to ensure the accuracy of the delivered dose. The "hardening" of the beam by the beam modifying filter is of limited importance. It was found that for copper filters the effective attenuation coefficient changes only by 2% per 1 cm of copper, which at 10 cm depth in water causes less than a 1% change in attenuation.

A procedure widely employed for photon dose calculation involves separate computations of the primary and scatter components of the radiation beam. Each one is manipulated according to the appropriate boundary conditions and recombination occurs as a final step. This method allows very accurate handling of beam filters, missing tissue and off-axis calculations, Bleehen et al.(1983).

The dose, D(P), to a point, P, at depth, d, in a phantom irradiated by a beam of photons may be expressed as:

$$D(P) = D_A(d)\left[f(d,x,y)\ TAR(d,0) + SAR(d,r)\right] \qquad 5.10$$

where: $D_A(d)$ is dose in free space at depth, d, x, y

are the coordinates of point, P in a plane perpendicular to the beam central ray with the central ray as the origin, f(d, x, y) is a factor describing the relative beam intensity in air as modified by the collimating and flattening system, TAR(d, 0) is the zero area TAR and describes the attenuation of the beam caused by the thickness, d, of a phantom material and SAR(d, r) is the scatter-air ratio at depth, d, for a beam of a radius, r, and is defined by equation 4.7.

TAR(d, 0) values are stored in look-up tables, SARs are calculated using the method described in paragraph (4.2).

In the case when a beam modifying filter is inserted into the beam both primary and scatter components must be modified by the transmitted fraction of photons through the filter. The total dose to a point, P, can be written as:

$$D(P) = D_A(d)\left\{f(d,x,y)\,TAR(d,0)\,TR + \sum_{i=1}^{n}\frac{\Delta\theta}{2\pi}\sum_{r_i=0}^{R_i} TR(r_i,\theta)\times\left[SAR(d,r_i(\theta)) - SAR(d,r_i(\theta)-\Delta r)\right]\right\} \quad 5.11$$

The diagram (5.2) illustrates the calculation of the dose at point, P, for such a case. The primary beam at a point, P, is modified by the portion of a wedge

immediately above it (TR), the scatter from each component is added separately taking into account the depth of tissue above that element and the change in dose, in free space due to the attenuation of the primary beam by a thickness of a filter above that element (TR(r, θ)).

The existing AECL computer treatment planning algorithm uses a simplified version of equation 5.11 for rectangular fields to sum the scatter from the elements in a beam. Advantage is taken of the rectangular shape of the beam as shown schematically in Fig.(5.3), reproduced from the AECL manual. The point, P, will receive primary radiation which has passed through the filter and has been attenuated by it. The amount of scatter contributed by the crosshatched volume will be dependent on the primary radiation striking the volume and this will be attenuated by another part of the filter. The total scatter at point P would be the sum of a series of such scatter terms for each different volume, each weighted by the primary intensity for its position. It is assumed that the primary for the entire slab is approximately equal to that at the centre of the slab and that the filter does not change its topographical shape as a function of length and only changes of the filter thickness along the attenuator length are incorporated in the calculations. Dose to a point P can be written as:

Figure 5.2. Diagram to illustrate the calculation of the dose at point, P.

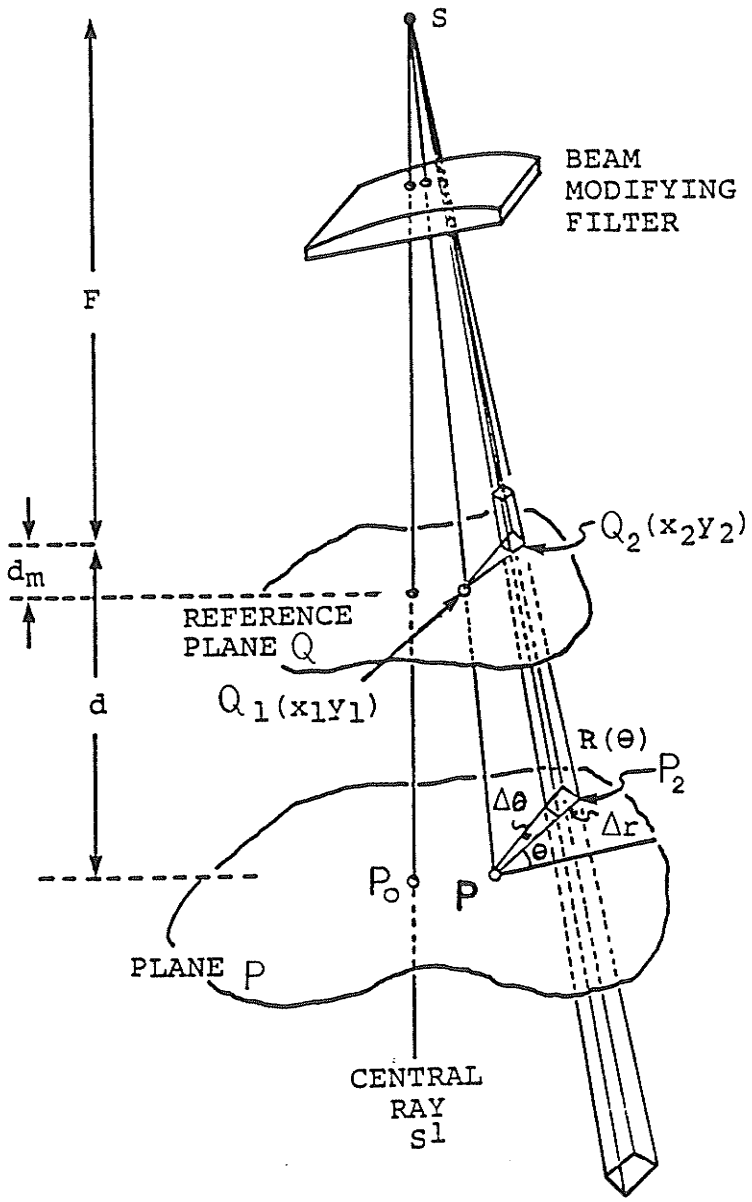
S
BEAM
MODIFYING
FILTER
F
d_m
d
REFERENCE
PLANE Q
$Q_2(x_2y_2)$
$Q_1(x_1y_1)$
R(θ)
P_2
Δθ
Δr
θ
P_o
P
PLANE P
CENTRAL
RAY
s1

Figure 5.3. Diagram to illustrate the calculation of the dose at point, P, for rectangular beams.

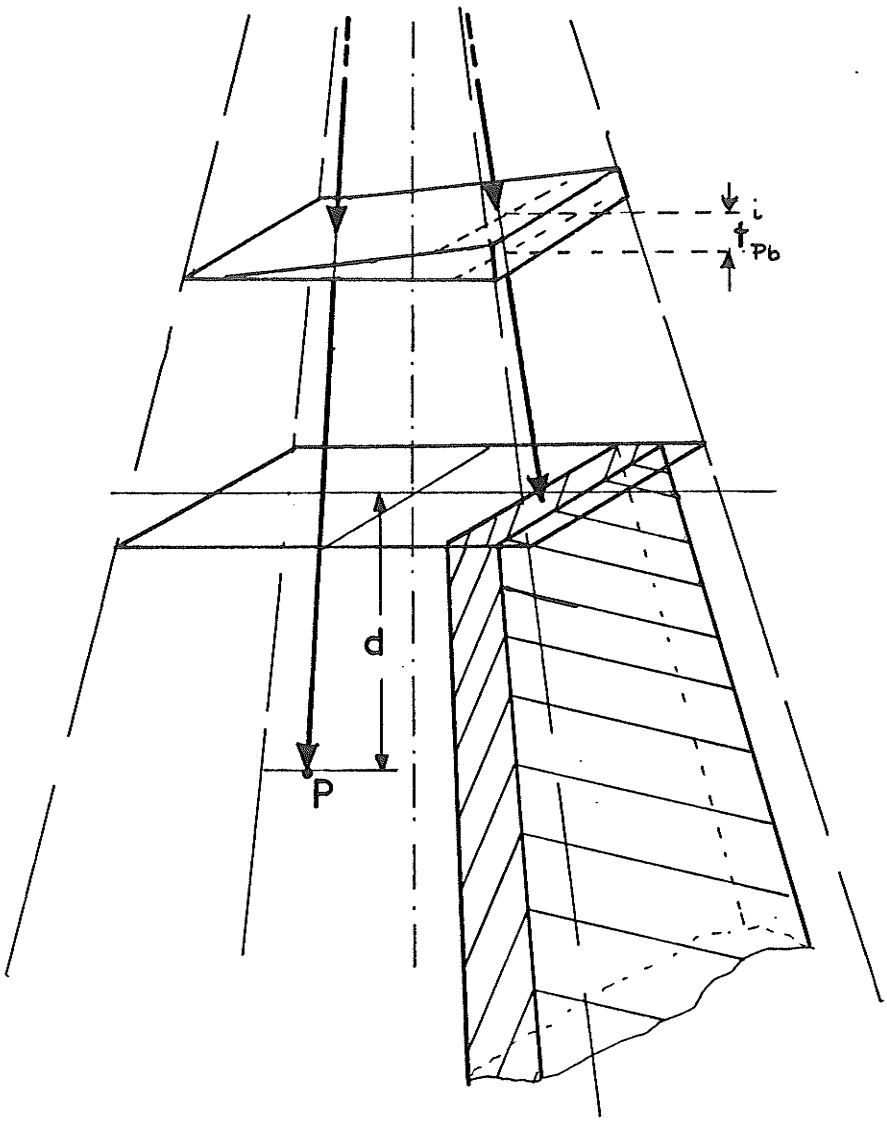
i
Pb
d
P

$$D_p = D_A(P)\left\{ f(d,x,y)\, TR(t_{Pb})\, TAR(d,0) + \sum_{i=1}^{n} f_s\, TR(x_i, t^i_{Pb})\ \Delta SAR(d,x,W_y, WYC)\right\} \qquad 5.12$$

where: f(d, x, y), $D_A(P)$ and TAR(d, 0) have been explained in section 5.3. ΔSAR(d, x , Wy, WYC) is a measure of the scatter to a point, P, from the crosshatched vertical slab of a length, Wy, and width, x, n is the number of scattering elements to be included in the summation, $TR(x_i, t^i_{Pb})$ is the transmitted fraction of photons through the filter reaching the point of calculation and f_S is a factor relating the primary for the i-th slab to its value on the central ray.

The transmitted fraction, TR, can be expressed as:

$$TR(x_i, t^i_{Pb}) = e^{-\mu t^i_{Pb}} \qquad 5.13$$

where: μ is the narrow beam linear attenuation coefficient of the filter material and t^i_{Pb} is the i-th rayline thickness of material along the rayline between the point of calculation and the source.

In practice, when the narrow beam linear attenuation coefficient and the geometrical dimensions of the attenuator are used in dose calculations errors as high as 26% can occur. The use of the broad beam attenuation

coefficient can improve the dose calculations for some points but, for example, for a 45° wedge for 4 MV SHM linear accelerator, errors as high as 8% can still occur. Fig.(5.4) shows the errors between measured at 10 cm depth in a water phantom for a 20x20 cm^2 field beam profile and calculated, using the Theraplan dose distribution calculation algorithm, beam profile for the same irradiation conditions. The practical solution to achieve an acceptable agreement between the measured and calculated dose distribution is to measure the transmitted fraction of photons through a given filter across the field, and use the obtained TR values to recalculate, according to equation (5.13), the geometrical dimensions of the wedge corresponding to the attenuation coefficients used in the calculations. These "effective" dimensions are then used in future calculations. This process requires the acquisition of data for each individual wedge (or compensator) and if the error is to be kept below 3% such data should also be obtained for different field sizes.

In summary, the absorbed dose from a beam of incident photons at a point in a phantom can be presented in simplified form as a product of the dose in free space modified by the transmitted fraction of photons and TAR.

Figure 5.4. The errors in dose distribution calculation, when 45^{o} wedge for 4 MV SHM linac is inserted into the beam.

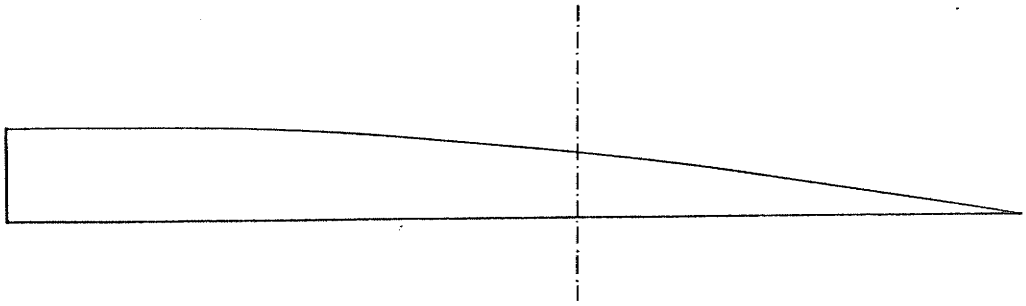

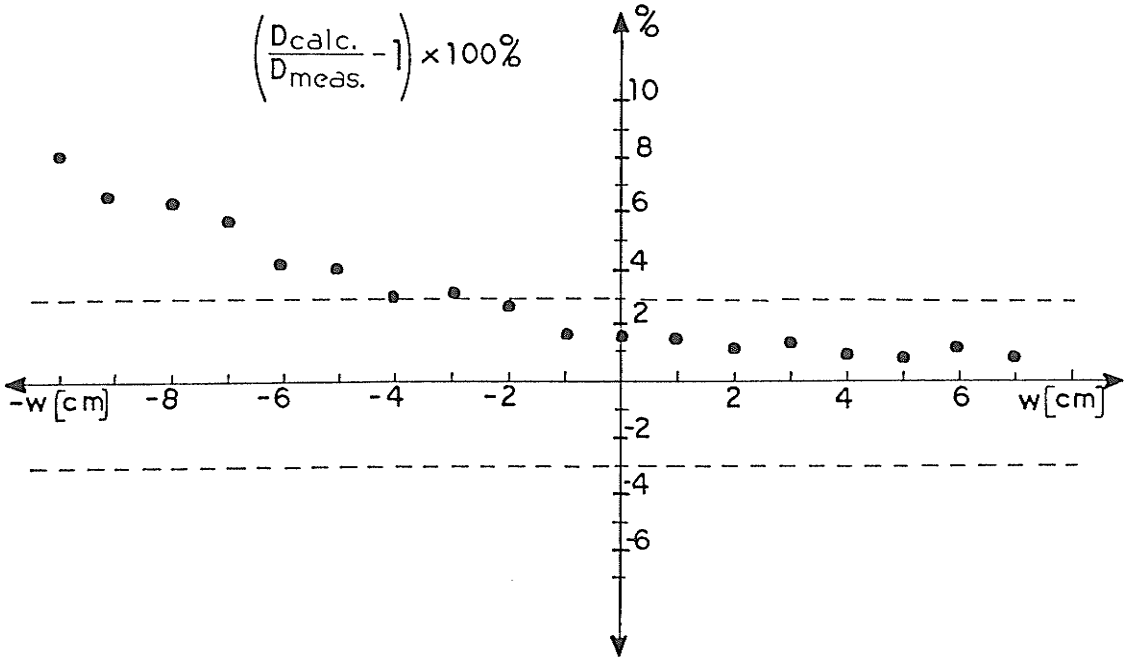
$\left(\frac{D_{calc.}}{D_{meas.}} - 1\right) \times 100\%$
%
10
8
6
4
2
-2
-4
-6
-w [cm]
-8
-6
-4
-2
2
4
6
w [cm]

$$D(P) = D_A \times TR \times TAR$$

5.14

where: TR is the transmitted fraction of photons through an attenuator, TAR is tissue-air ratio and D_A is dose in free space.

The presence of any attenuator will have an influence on dose in air as well as on TAR. For the amount of lead usually used for wedges and compensators, and for 10 cm depth in a phantom, which is a depth for which accuracy tests are normally performed, the hardening effect on TARs can be neglected. Therefore the main source of errors is the transmitted fraction, TR, of photons through the attenuator.

The dose calculational methods do not take into account or do not account fully for the following facts:

i) the energy spectrum across the beam is dependent on the distance from the central axis for the 4MV SHM linac

ii) the thickness of most attenuators in use (wedges, compensators) changes throughout the beam.

iii)the "effective field size", as defined by Day (1950) and Jones (1949) changes throughout a given field. In the discussion of the field size depend - ance of the attenuation coefficient (van Dyk (1986)) the attenuation coefficient on the central axis of

the field has been considered. It has also been demonstrated that for irregular fields the central axis coefficient can be obtained by Clarkson's sector integration technique. However, for off-axis points within a given beam the "effective field size" will change and under some circumstances this can also introduce a significant error.

The purpose of the present work was to develop a calculational method which is able to predict TR values across any filter from its physical properties with sufficient accuracy to keep the errors involved within 3%. The method developed accounts for the defciencies (i), (ii) and (iii) described above.

5.4. The experimental parameters.

5.4.1. Introduction

The calculational method developed in this project takes into account all variables which may affect the transmission of photons through the attenuators, namely: the field size, the changing thickness of the attenuator across the field and the changes in the energy spectrum. The values of effective attenuation coefficient measured experimentally under different treatment conditions for the same beam quality radiation and attenuating material show some discrepancies. The effective attenuation coefficient for lead for Co-60 γ -rays was found to be $0.81 cm^{-1}$ in an experimental work performed by Leung (1974) and a value of 0.77 cm^{-1} has been reported by Wilks and Casebows (1969) and 0.636 cm^{-1} has been reported by van Dyk (1986). These results strongly suggests that the value of μ_{eff} or the transmitted fraction TR of photons through the attenuators reaching the detector is dependent on the experimental setup and thus the simulation of treatment conditions for the transmission measurement is very important. Care was taken to ensure that the experimental setup will resemble the typical treatment geometry. The source-attenuator-detector arrangement was such as when wedges are being used.

5.4.2. Radiation sources.

5.4.2.1. Cobalt-60.

The source of the Co-60 γ-rays employed in this work is a Theratron "F" Cobalt- 60 teletherapy unit with a SSD (source to surface distance) of 75 cm. The source provided an exposure rate of 127.6 roentgens per minute at 75 cm distance when measured on May 11,1987.

5.4.2.2. MV x-rays.

The source of 4 MV x-rays employed in this work is a 4 MV SHM Therapi 4 medical linear accelerator with a SSD of 80 cm. The linac produces a parallel beam of 4 MeV electrons, approximately 3 mm in diameter. This electron beam strikes the target made of high Z material, and the x-ray field produced is flattened by a lead flattening filter which is designed to produce optimum field flatteness at a 10 cm depth in a phantom. The primary collimators provide a maximum field size of 32x32 cm^2 at 80 cm SSD. The depth of maximum dose is 1.2 cm as measured in water for a 10x10 cm^2 field at 80 cm SSD. The x-ray output is approximately 0.01 cGy per radiation pulse at a distance of 80 cm in air for the target with a pulse rate equal to 240 per sec.

5.4.3. Dosimetry devices.

The exposure measurements were carried out with a Capintec - 61143 air equivalent plastic Farmer Replacement ionization chamber with an effective volume of 0.6 ml. The chamber has a diameter 7 mm and length of 22 mm and an air equivalent plastic wall of 50 mg/cm^2 thickness. In all measurements the chamber was used with the appropriate buildup cap i.e. 0.5 g/cm^2 Lucite cap for Co-60 γ-rays radiation and 1.5 g/cm^2 Lucite cap for 4MV x-rays. The buildup cap thickness was furnished to prevent secondary electrons generated by the filter from entering the active volume and to provide build up. The ionization chamber was connected to a Keithley 35614 dosimeter. The equipment was turned on and allowed to stabilize. A number of readings of leakage current integrated over 1 min. were taken while the machine was "off" and the effect was found to be negligeable. Hanson et al.(1986) found that the effect of irradiating the entire stem is not significant and this effect was ignored. Each signal represented charge collected for a fixed reading of 200 monitor units (1 monitor unit corresponds approximately to 1 cGy at 80 cm SSD at 1.2 cm in water for a 10x10 cm^2 field) in the case of the 4MV x-rays and for a fixed time of 1 min.-corrected for the shutter error for a Co-60 machine. The combined

variation for the detector and monitor circuit was evaluated by repeated exposures without the attenuators and was found to be within 1% of the mean value.

A beam profile scanner was used to measure the effect of the filters on dose distribution in a water phantom. Two beam profiles were measured for a given wedge for each machine. The first profile was measured without the filter in the beam for a flat surfaced phantom at 10 cm depth. The second beam profile was made at the same depth in a water phantom with the filter inserted into the beam. The latter beam profile was normalized at 10 cm depth in water at the central axis to the open beam profile. The size of the field was defined at the surface of the phantom. The scans were taken across the radiation field at 10 cm depth with an EMI two-dimensional isodose plotter, equipped with 0.1 cm^3 PTW ionization chamber. Fig.(5.5) shows the Automatic 2D Isodose Plotter System manufactured by EMI Therapy Systems. The three units which are identified in Fig.(5.5) are integrated into a dual dosimeter circuit, an X-Y positioning circuit, and an analog and digital control circuit. The Automatic 2D Isodose Plotter system is capable of making two dimensional measurements of a cross-section of the radiation field in a water phantom. When a radiation beam is directed through the phantom,

Figure 5.5. Automatic 2D isodose plotter system configuration.

X-Y DRIVE AND WATER TANK ASSEMBLY UNIT 1

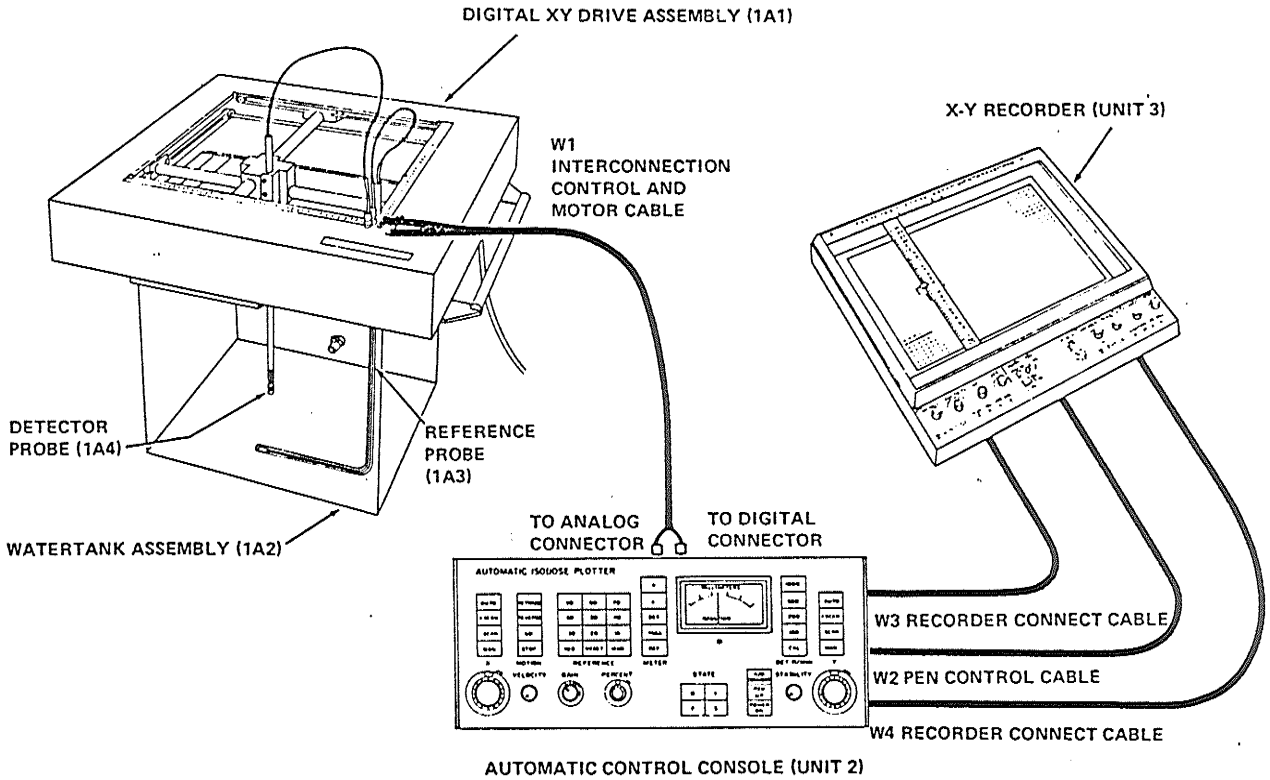

a detector probe scans the radiation field according to the specified mode of operation, and provides a signal indicating its position and the intensity of the radiation at a point to the Control Console. The Control Console processes this signal and sends that voltage to the X-Y Recorder which plots the measurements on graph paper. The system may be used to obtain the following relative measurements: beam profiles, depth dose curves and isodose curves.

5.4.4. Experimental setup.

The transmission data were measured for the experimental setups shown in Fig.(5.6) and in Fig.(5.7). The lead sheets used as absorber material for these experiments were nominally 99.9 % pure lead of 11.36 g/cm^3 density. The lead covered the entire beam and thicknesses were determined by dividing the weight by the area and density for each absorber thickness. The absorber thicknesses were 1.1, 5.33, 8.76 and 14.9 mm. The maximum value was determined by the clearance between the machine diaphragm and the wedge tray. The lead sheets were sequentially placed over a thin Lucite tray. The ion chamber was set up coaxially with the beam at a fixed source to ion chamber distance of 75 cm in the case of the Theratron F Co-60 machine and of 80 cm in the case of the 4 MV SHM

Figure 5.6. The experimental setup for the transmission study for Co-60 radiation.

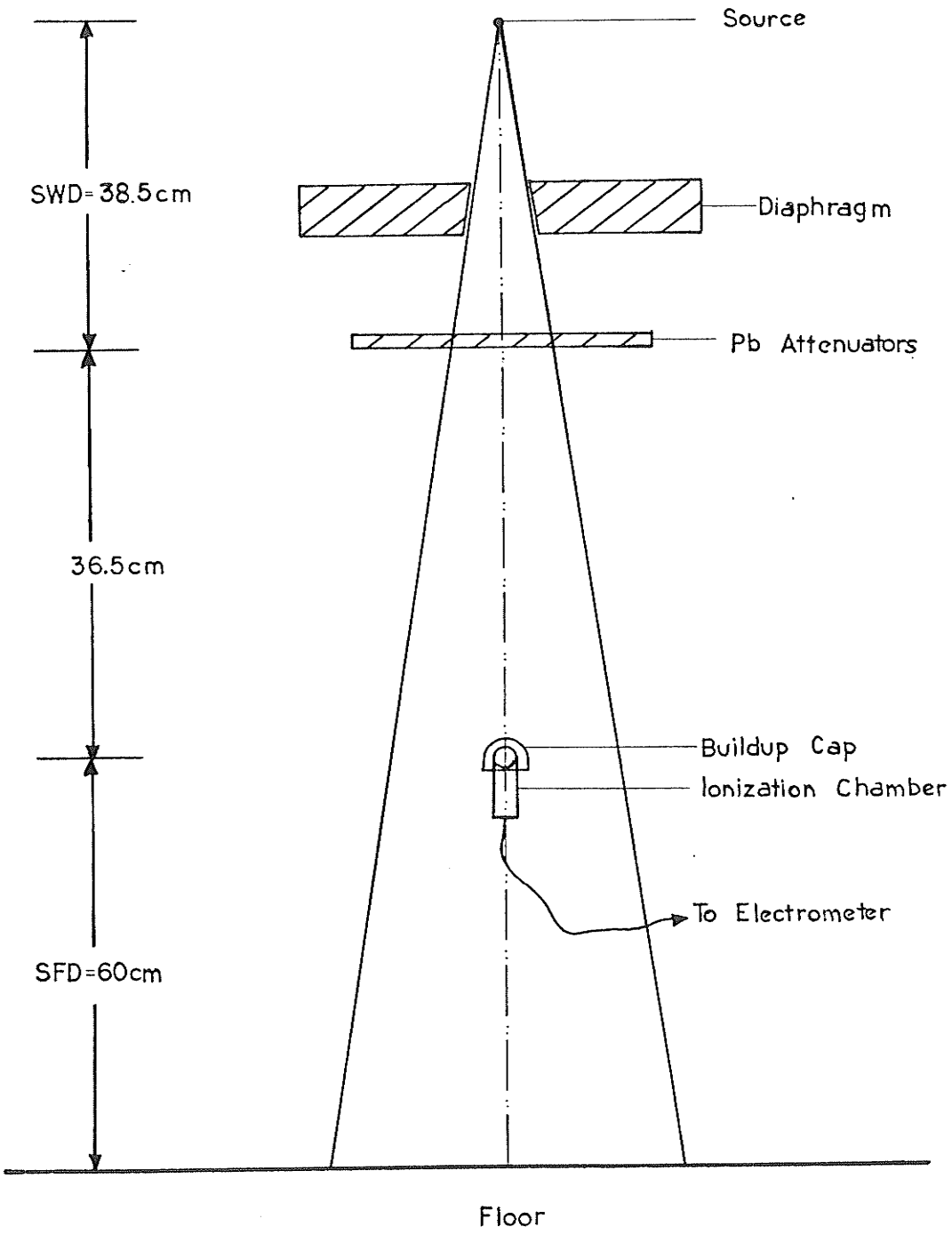
Source
SWD=38.5cm
Diaphragm
Pb Attenuators
36.5cm
Buildup Cap
Ionization Chamber
To Electrometer
SFD=60cm
Floor

Figure 5.7. The experimental setup for the transmission study for 4 MV x-rays.

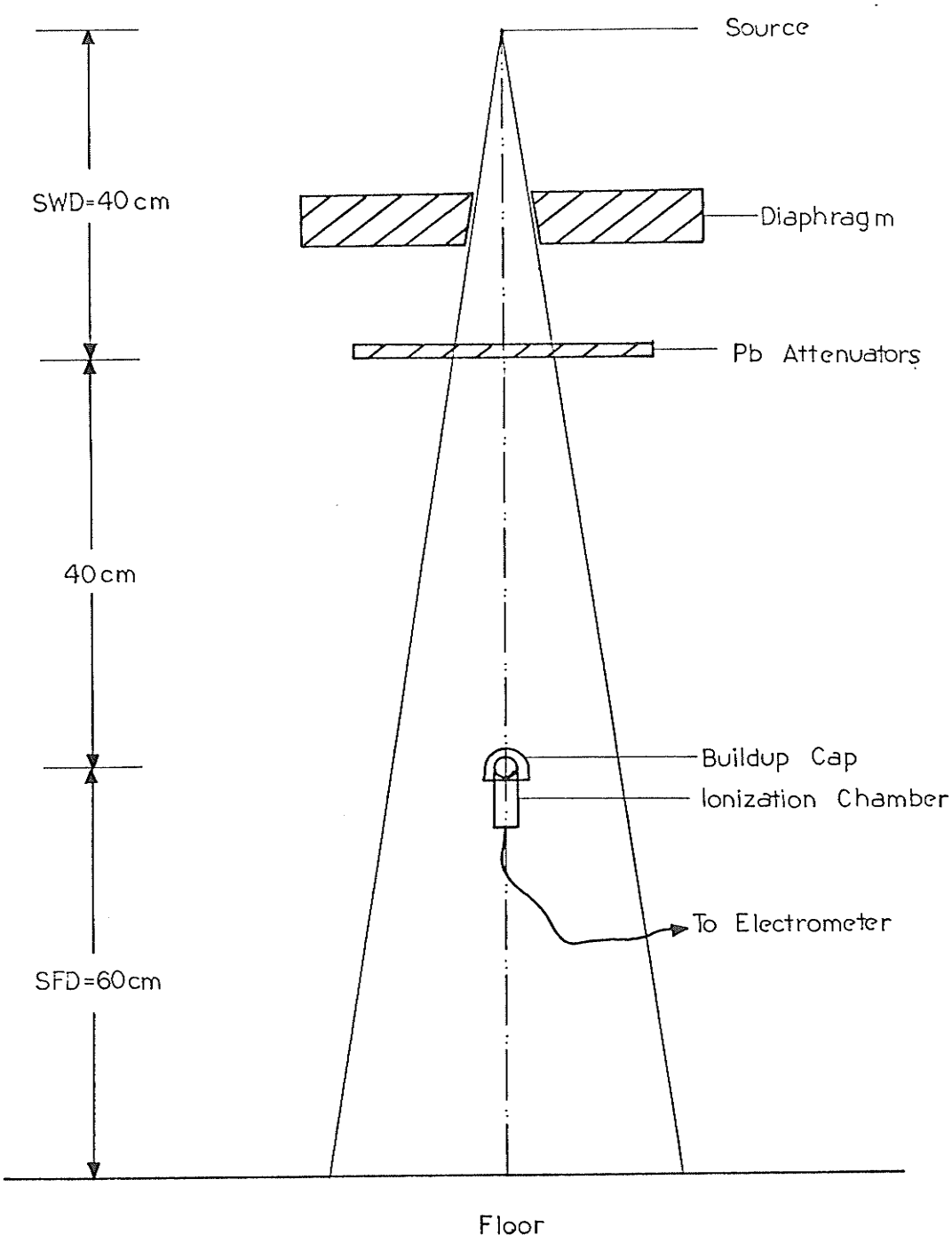
Source
SWD=40 cm
Diaphragm
Pb Attenuators
40 cm
Buildup Cap
Ionization Chamber
To Electrometer
SFD=60 cm
Floor

linac. The size of the field was large enough to clearly enclose the buildup cap. The measurements were performed for all attenuator thicknesses for field sizes of 3.5x 3.5 cm^2, 5x5 cm^2, 7x7 cm^2, 10x10 cm^2, 15x15 cm^2 and 20x20 cm^2 for the Co-60 machine and for field sizes of 3.5x3.5 cm^2, 5x5 cm^2, 10x10 cm^2, 15x15 cm^2, 20x20 cm^2 and 30x30 cm^2 for the 4 MV SHM linac. A diagram of the experimental setup for off-axis measurements is shown in Fig.(5.8) only for the 4MV SHM linac. The energy spectrum for the Co-60 machine does not change significantly across the radiation field. The field sizes set by collimators were 30x3.5 cm^2, 30x 5 cm^2, 30x7 cm^2 and 30x10 cm^2 at the ion chamber position, and the thick lead blocks defining the size of a square field in the other direction were placed below the attenuating lead sheets on the block tray. The gantry was rotated to different -angles to position the off-axis beam vertically and the measurements for the given field sizes at different positions off-axis at 2°, 5°, 7° and 9° from the central axis were performed. In this experimental technique of Hanson et al.(1980) oblique incidence is automatically accounted for since measurements are taken along off-axis rays. The TR values across a 30x30 cm^2 4 MV x-rays radiation field were measured at 80 cm distance from the source, at 2°, 5°, 7° and 9° off the central axis for attenuators 5.33, 8.76 and

Figure 5.8. Experimental setup for transmission measurements at different α angles off the central axis.

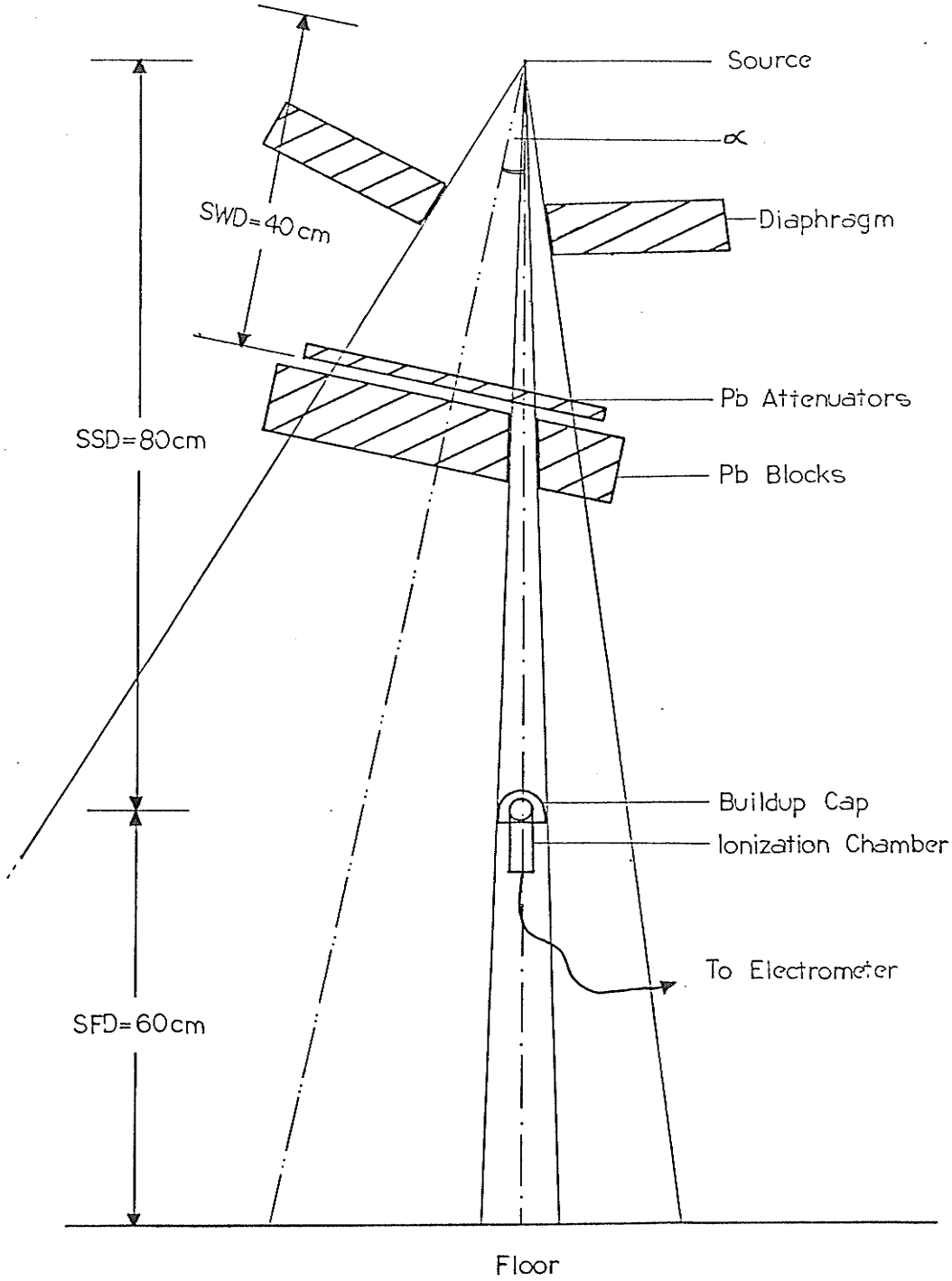
Source
∝
Diaphragm
SWD=40cm
Pb Attenuators
Pb Blocks
SSD=80cm
Buildup Cap
Ionization Chamber
To Electrometer
SFD=60cm
Floor

14.9 mm thick. The results are depicted in Fig.(5.13). For Co-60 radiation beam such measurements were not performed, since such data was not required for the improvement in dose distribution calculations.

5.5. The transmitted fraction of photons through the attenuator-TR.

The transmitted fractions are the ratios of detector signals for the same experimental setup with and without the attenuating material in a beam. The Lucite supporting tray was considered to be a part of a treatment head and was left in place for all measurements. Experimental uncertainties in all transmitted fraction measurements were determined by making each measurement several times. The errors were within 1.2 % of the mean value.

The results of the transmission measurements for a Co-60 γ-ray beam are shown in Fig.(5.9) and for 4 MV x-rays in Fig.(5.10). The transmitted fraction of photons through the lead filters is plotted as a function of the radius of the field instead of the side of a square field. This conversion is done by using the equivalent field method as described by Jones (1949), Day (1950) and Batho et al.(1956). Each curve represents data for a different thickness of the attenuating filter. The zero area

Figure 5.9. The transmission through lead for Co-60 γ-rays as a function af radius of the field, each curve is plotted for a different thickness of the lead filter.

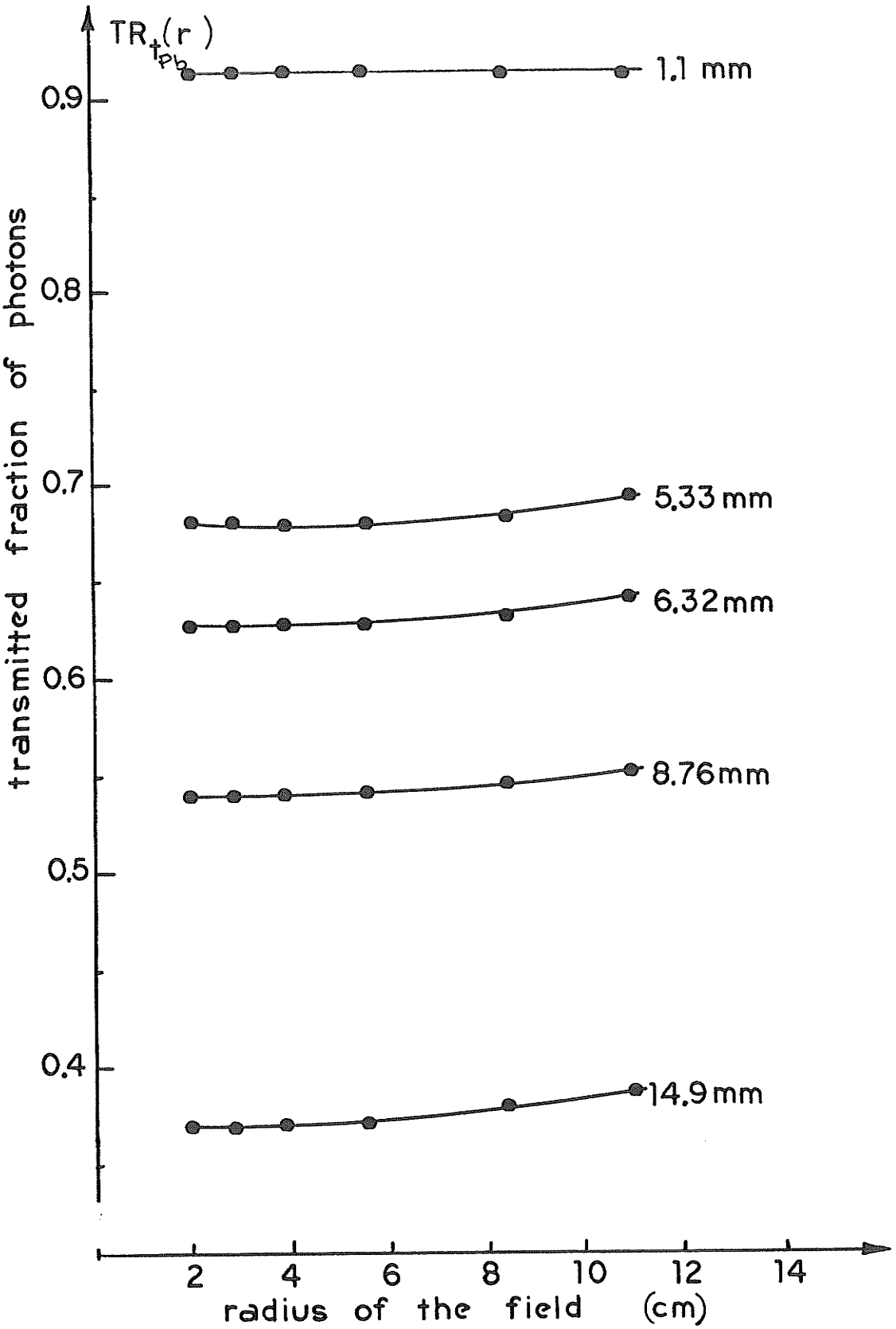
TR_tPb(r)
1.1 mm
5.33 mm
6.32 mm
8.76 mm
14.9 mm
transmitted fraction of photons
0.9
0.8
0.7
0.6
0.5
0.4
2
4
6
8
10
12
14
radius of the field (cm)

Figure 5.10. The transmission through lead for 4 MV x-rays as a function of radius of the field, each curve is plotted for a different thickness of the lead filter.

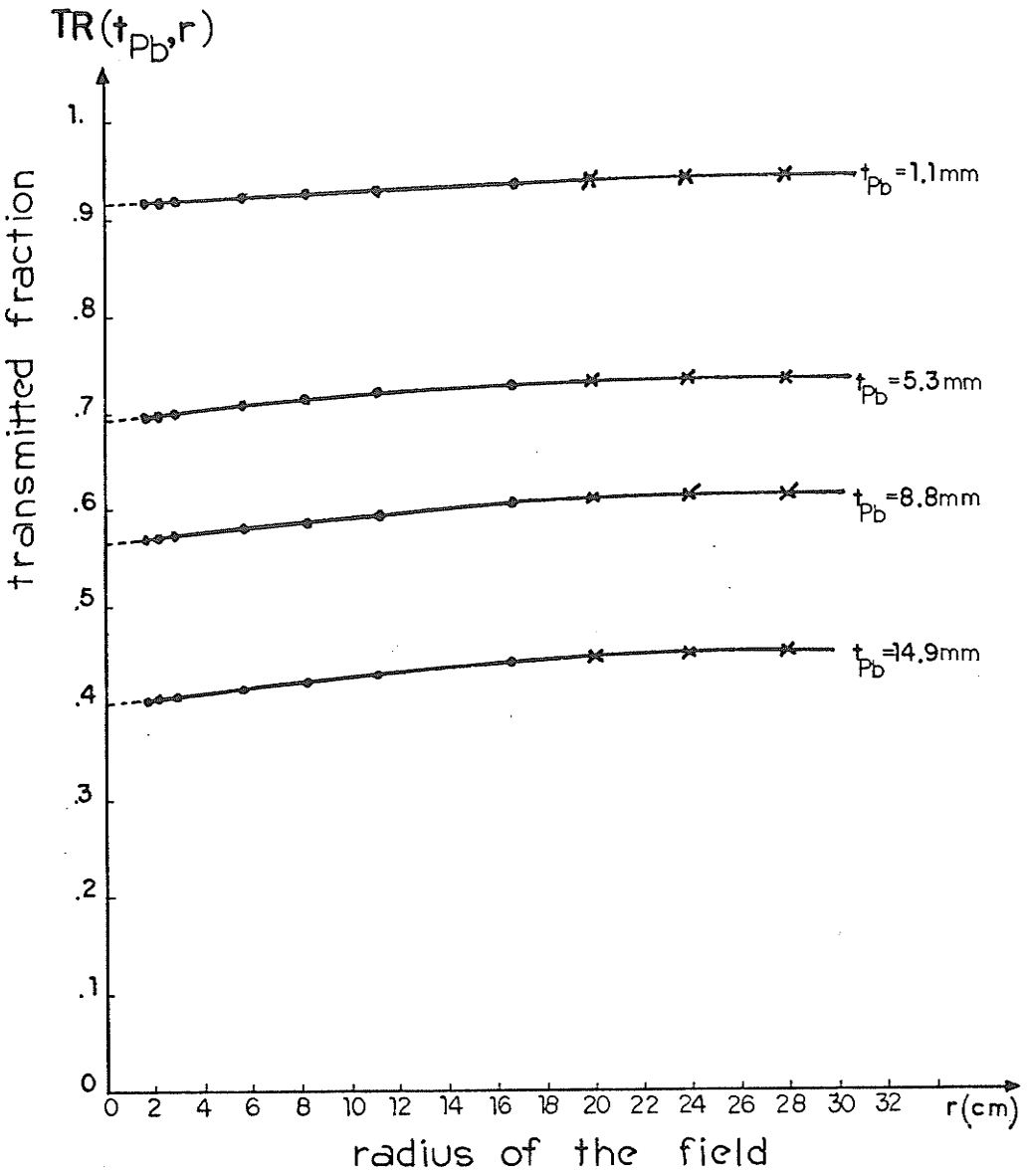
TR(t_Pb, r)
transmitted fraction
1.
.9
.8
.7
.6
.5
.4
.3
.2
.1
0
0 2 4 6 8 10 12 14 16 18 20 22 24 26 28 30 32
r(cm)
radius of the field
t_Pb=1.1mm
t_Pb=5.3mm
t_Pb=8.8mm
t_Pb=14.9mm

values for the transmitted fraction of photons through a given attenuator were obtained by extrapolating (by hand) the TR values measured for few small field sizes to the zero area field. The points for large field sizes, for 4 MV x-rays, marked by crosses, were not obtained by direct measurements but are the results of extrapolation which is part of a SARTAB routine of the Theraplan calculation algorithm. This extrapolation technique is described in appendix A.

Results for 4 MV x-rays show that the curves increase smoothly with increasing number of scattered photons reaching the detector. The curves tend to level off at very large field radii. The differences between the total transmitted fractions and the zero area values, which represent the scatter component of the total transmittance are plotted in Fig.(5.11). The scatter component increases with the thickness of the scattering material for a given field size, which is expected, since a thicker layer of the scattering material will produce more scattered photons. For further use in calculations data for different thicknesses of attenuating material than have been measured are needed. Therefore the TR (t_{Pb}) values for different radii of the field as a function of the attenuator thickness were plotted and are shown in Fig.(5.12). Values for different thicknesses

Figure 5.11. The scatter component of the total transmission plotted as a function of the radius of the field, each curve corresponds to a different thickness of the lead filter.

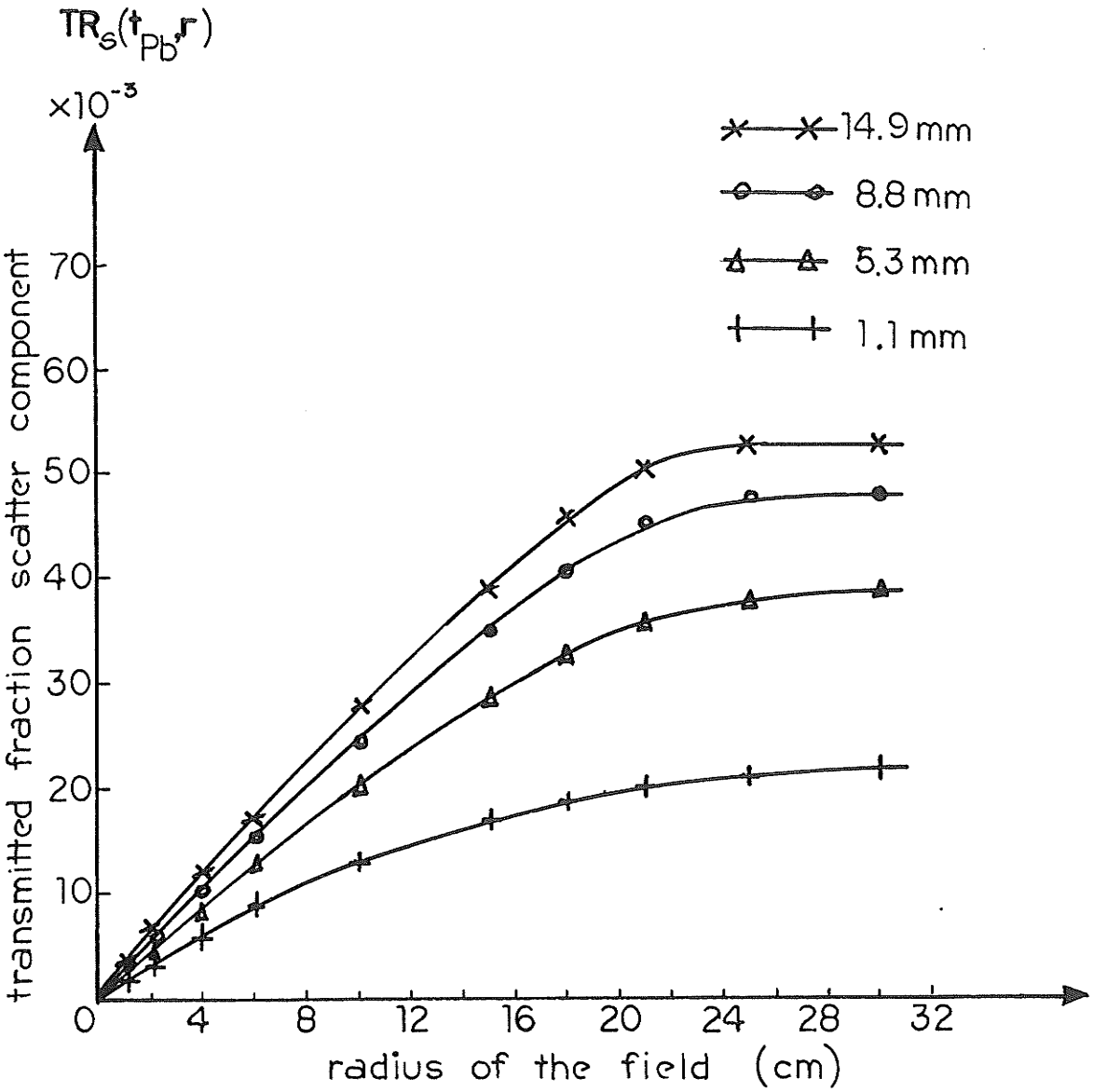
$TR_s(t_{Pb}, r)$
$\times 10^{-3}$
14.9 mm
8.8 mm
5.3 mm
1.1 mm
transmitted fraction scatter component
70
60
50
40
30
20
10
0
4
8
12
16
20
24
28
32
radius of the field (cm)

Figure 5.12. The total transmitted fraction of photons plotted as a function of the attenuator thickness, each curve for a different radius of the field size.

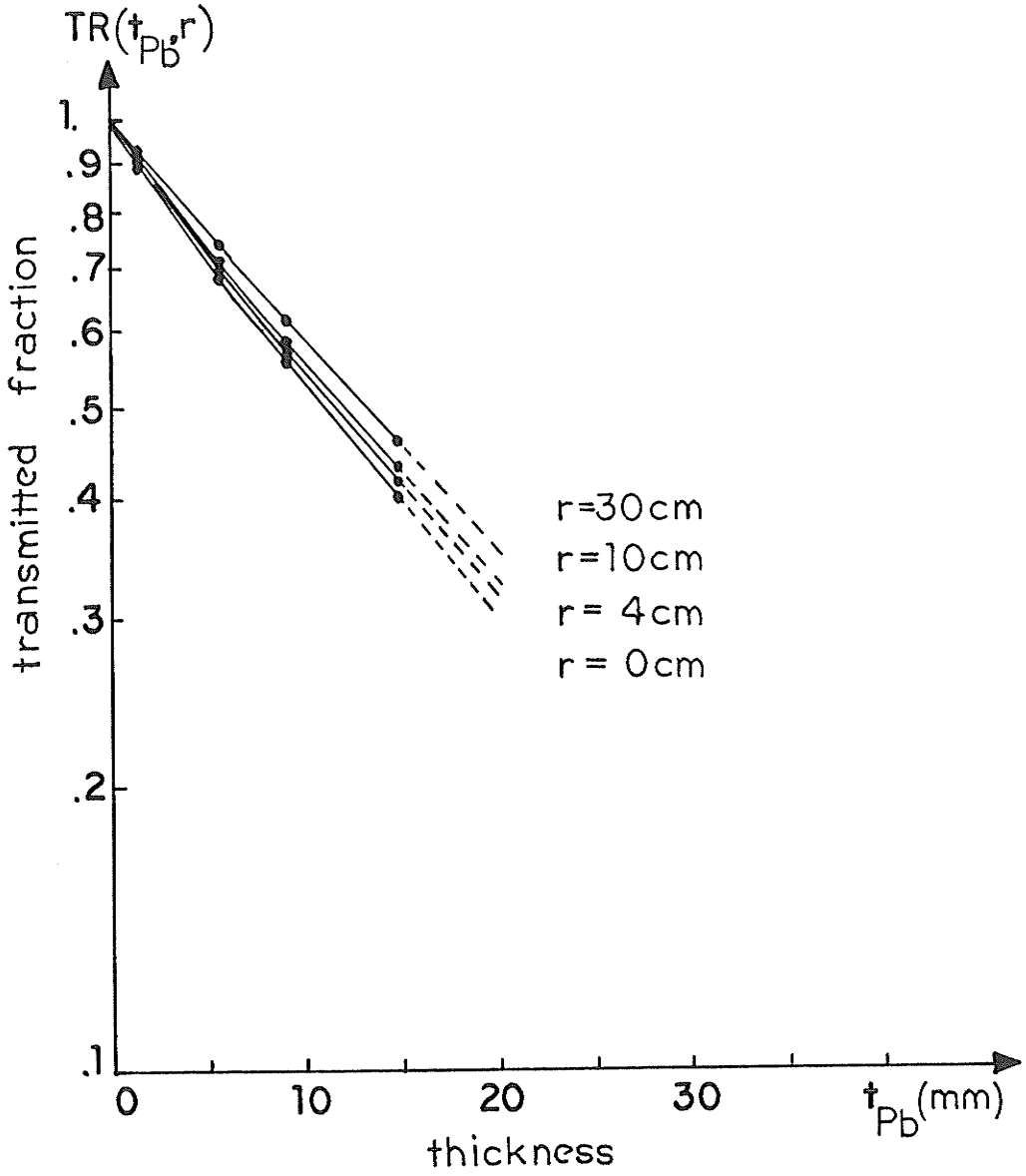
TR(t_{Pb},r)
transmitted fraction
1.
.9
.8
.7
.6
.5
.4
.3
.2
.1
r=30cm
r=10cm
r= 4cm
r= 0cm
0
10
20
30
t_{Pb}(mm)
thickness

can then be read from the graph. As was mentioned in section 2.2. the energy spectrum for 4 MV x-rays in the central part of a photon beam is somewhat harder than in the region near the edge of the beam. Since the variation of spectrum across the beam is important when calculating the transmission through an attenuator, the transmitted fractions, TR, at different α -angles for a few small field sizes have been measured. The results of these measurements are presented in Fig.(5.13). Each point, for TR_o is the result of the extrapolation from measurements performed for several small field sizes. These data are presented on a semilogarithmic scale in Fig.(5.14). Data for different thicknesses of attenuating material for different off axis points of calculation can be read from these graphs. The result of all those measurements is a complete set of transmission data for different thicknesses of lead filters, field sizes and distances from the central axis. For 4 MV x-rays the results are presented in Table 5.1. The zero area transmitted fractions can be presented as a double exponential function of lead thickness,t and distance from the central axis,w :

$$TR_o(t_{Pb}, w) = (1-A)\, e^{-0.5\, t_{Pb}} + A\, e^{-0.058\, t_{Pb}} \qquad 5.15$$

where: $A = 0.954 - 0.006\ w$

Figure 5.13. The zero area component of the total transmission and the the total TR measured across the radiation field as a function of the distance off the central axis, each curve represents data for different filter thickness.

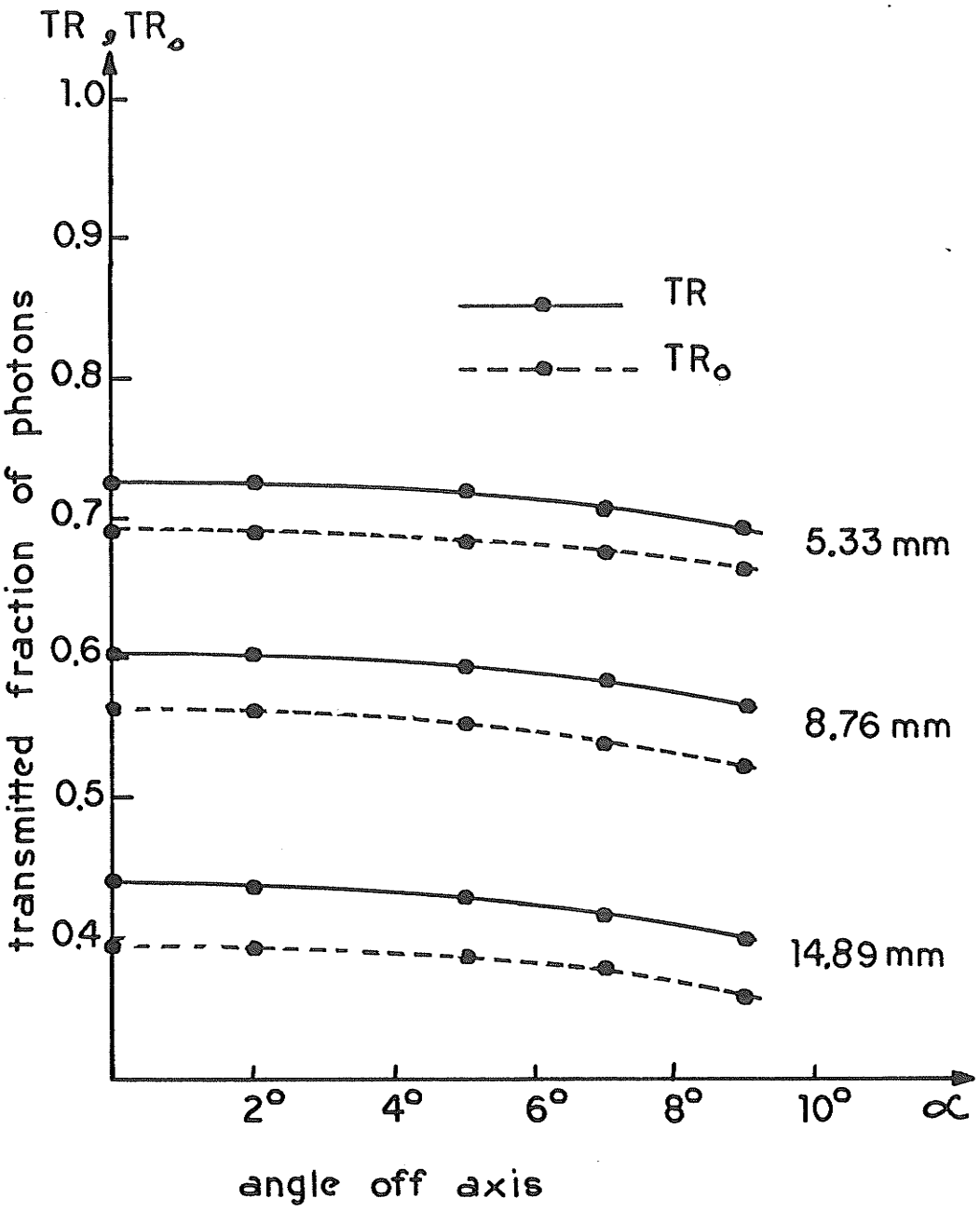
TR , TR$_o$
1.0
0.9
0.8
0.7
0.6
0.5
0.4
transmitted fraction of photons
TR
TR$_o$
5.33 mm
8.76 mm
14.89 mm
2°
4°
6°
8°
10°
α
angle off axis

Figure 5.14. The zero area component of the total transmission as a function of the attenuator thickness, each curve representing data for a different position off the central axis.

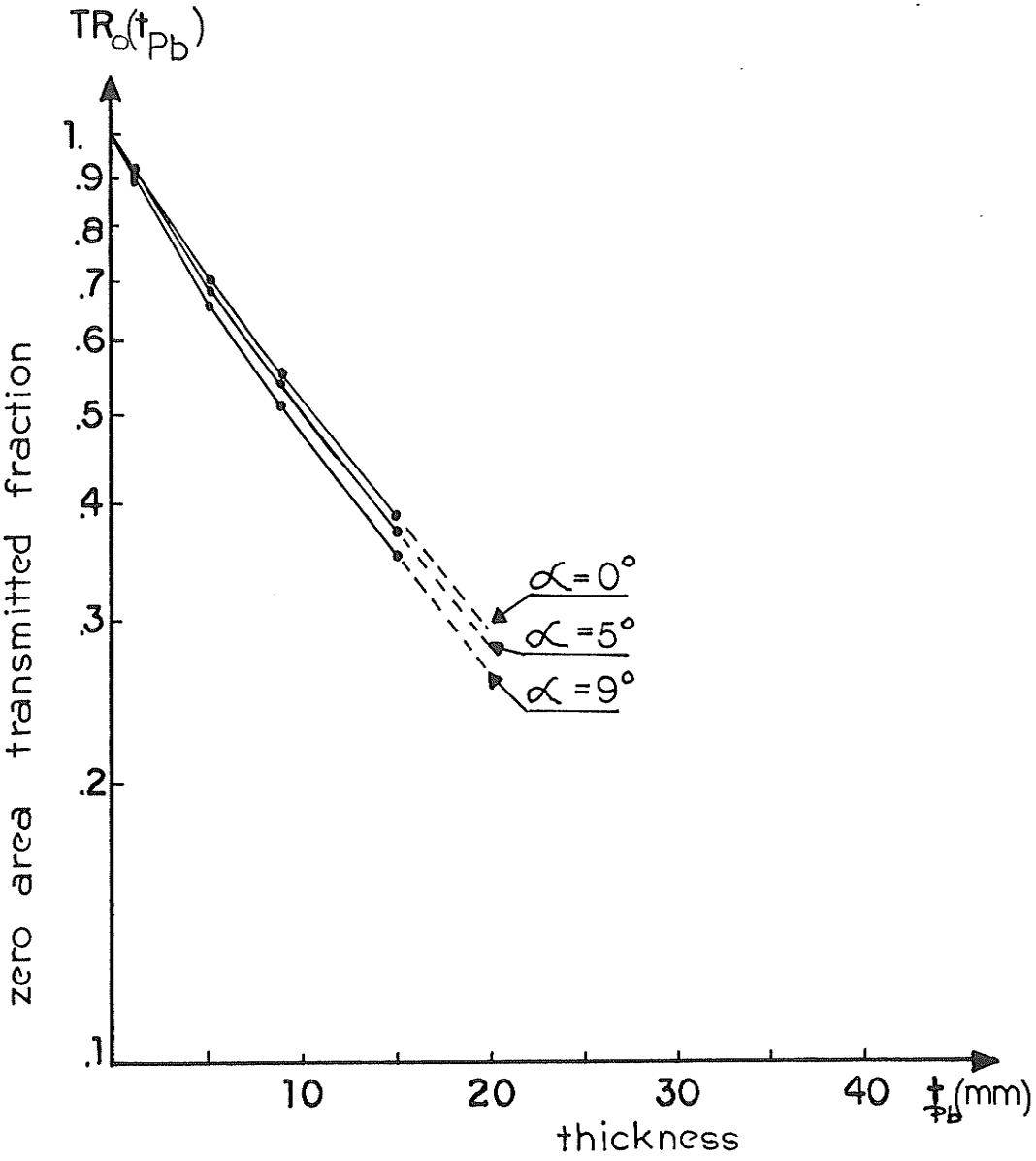
TR_o(t_Pb)
1.
.9
.8
.7
.6
.5
.4
.3
.2
.1
zero area transmitted fraction
α=0°
α=5°
α=9°
10
20
30
40
t_Pb (mm)
thickness

Table 5.1. The transmission data as measured and extrapolated for different lead thickness, and radius of the field. The zero area and scatter component are displayed in different columns.

		$TR_S(t_{Pb}, r) \times 1000$									
t_{Pb} [mm]	$TR(t_{Pb}, r=0)$	Radius of field size [cm]									
	0	1	2	4	6	10	15	18	21	25	30
0.	1.000	0	0	0	0	0	0	0	0	0	0
0.7	.946	1	3	5	8	10	12	14	15	16	17
1.1	.917	1	3	6	9	13	17	19	20	21	22
2.8	.820	2	4	7	11	16	23	26	28	29	32
5.3	.695	2	5	8	13	20	29	33	36	37	39
6.7	.636	3	6	10	15	23	34	40	44	45	46
8.8	.566	3	6	10	15	24	34	42	47	48	48
9.2	.552	3	6	11	17	25	34	42	48	49	50
11.5	.483	4	7	11	17	27	38	45	50	52	53
13.4	.434	4	7	12	17	27	38	46	51	52	53
149	.399	4	7	12	17	28	39	46	52	53	53
16.0	.374	5	8	13	18	30	42	48	53	54	54
16.5	.363	5	8	14	18	31	43	49	53	54	54

and w is the distance between the central and off axis ray as measured in the plane perpendicular to the central axis at the SSD distance from the source and is related to the off axis α-angle:

$$w = SSD \times \tan\alpha \qquad 5.15.$$

5.5.1. Analysis.

The relative transmission of the high energy photons through lead absorbers is dependent on the field size, the thickness of the attenuator, the spectrum of the radiation and on the source-surface distance.

The spectrum of the radiation impinging on the absorber consists of the primary radiation and the scatter component from the collimator. The primary component of radiation for a Co-60 source will not depend on the position off axis while the scatter component will depend on the field size and consequently on the position off axis.

For larger fields, the opening of the collimator is larger and more scattered photons will arrive at the detector positioned at some point, P at a given SSD. For smaller fields, because of the smaller opening the scattered photon has less of a chance of getting out without interacting with the collimator material a second time. Thus the exposure rate increases with field size.

The increase is more significant at smaller field size. When the field size is very large, the exposure rate attains a maximum value and should eventually decrease, because the scattering angle becomes to large and is not favourable for the Compton scattering process. The photons scattered from the collimators are of lower energy than the primary photons, thus with increasing field size the soft radiation component of the impinging radiation beam on the absorber increases, causing the resultant photon spectrum to become softer as the field size increases. Thus the transmitted fraction, TR, is expected to decrease with increasing field size, since the lower energy photons will be more absorbed. However, the absorber introduced into the radiation beam becomes the next source of scattered radiation, and this component will be field size dependent too. The total transmitted fraction of photons reaching the detector will increase with field size due to increased number of photons scattered from the attenuator.

The relative importance of these two effects will depend on the radiation, collimator design and on the amount of the absorbing material.

From the transmission data, depicted in Fig.(5.9), for Co-60 radiation, it can be seen that these two

effects counterbalance almost completely, except for very large fields. The effective attenuation coefficients calculated from these data, and presented in Fig.(5.15), show substantial dependence on the thickness of the attenuating material and much smaller dependence on the field size. It is possible to arrive at an acceptable accuracy for the calculated dose distribution by using attenuation coefficients corresponding to the thickness of the the attenuator along raylines, averaged over the range of clinically employed field sizes. Such a calculation was performed for a 20^{o} wedge for the Theratron "F" Cobalt-60 and the comparison with the measured dose distribution is presented in section 5.6.2.
The transmission data for 4 MV x-rays show the TR dependence on the field size, attenuator thickness and off axis position of the measuring point. The photon spectrum impinging on the attenuator depends on the distance from the central axis because of the effect which the flattening filter has on the radiation beam. Fig.(2.10) shows the change in the spectrum at different positions off axis, the beam becoming softer towards the edges of the beam. For 4 MV there is a more pronounced dependence of the TR on field size, indicating the predominance of scattered photons from the absorber. Therefore, for the 4 MV x-rays the off-axis change in

Figure 5.15. Effective attenuation coefficient as a function of the attenuator thickness, each curve represents data for different field size.

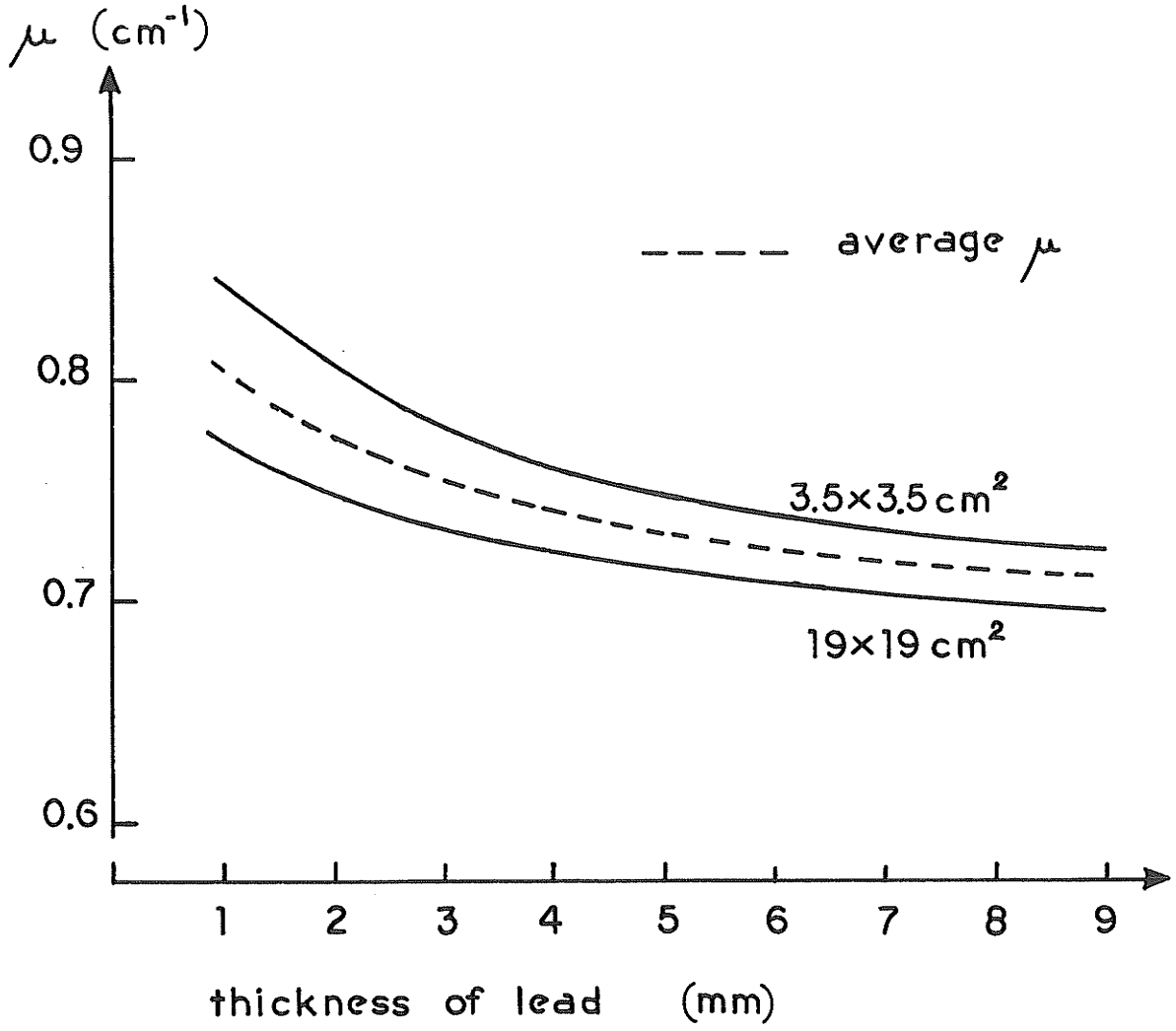
μ (cm⁻¹)
0.9
0.8
0.7
0.6
average μ
3.5×3.5 cm²
19×19 cm²
1
2
3
4
5
6
7
8
9
thickness of lead (mm)

spectrum and the field size dependence of the TR will have to be taken into consideration in the following analysis.

5.6. The TR calculational method.

The calculational method developed in this project takes into account all variables, except the dependence on the SSD, which may affect the transmission of photons through the attenuators, namely: the field size, the changing thickness of attenuator across the field and the changes in the energy spectrum.

The calculational method is based on the concept of separating mathematically the primary and secondary components. The primary component is the primary radiation transmitted through the attenuator and the scatter component is due to photons scattered uniformly throughout the volume of the attenuating material. Since these two components are functions of somewhat different parameters, it is useful to consider each component separately and combine them as the last stage in the calculation.

The total transmitted fraction of photons through the attenuator can be written as:

$$TR(t_{Pb}, r) = TR_o(t_{Pb}) + TR_S(t_{Pb}, r) \qquad 5.17$$

where:

$TR_o(t_{Pb})$ is the zero area transmitted fraction and $TR_s(t_{Pb},r)$ is the scatter component of total transmitted fraction.

Zero area in this context means the absence of scattered photons. If the irradiated area (volume) is reduced, so that r approaches 0, the scatter radiation reaching the point will tend to disappear while the primary radiation will remain.

$$\lim_{r \to 0} TR\ (\ t_{Pb}, r\ ) = TR_o(\ t_{Pb}) \qquad 5.18$$

This limit must be thought of as an empirical one which can best be obtained graphically by plotting $TR(t_{Pb},r\ )$ as a function of a radius of field size and extrapolating it to r =0. TR_o is a measure of the transmitted fraction of primary photons through the attenuator,and it will be a function of thickness of the attenuating material and the quality of the radiation. Since the spectrum changes for off-axis positions, TR will also depend on the off-axis position of the point of calculation.

The difference between the total TR measured for a given field size and the zero area value for the same amount of attenuating material, see Fig.(5.16), will depend on how many photons were scattered by the irradiated volume of the filter and reached the point of measurement. This scatter component will be a function of the thickness of the attenuator and field size, and it is assumed that the

Figure 5.16. Diagram illustrating the zero area and scatter component of the total transmiited fraction.

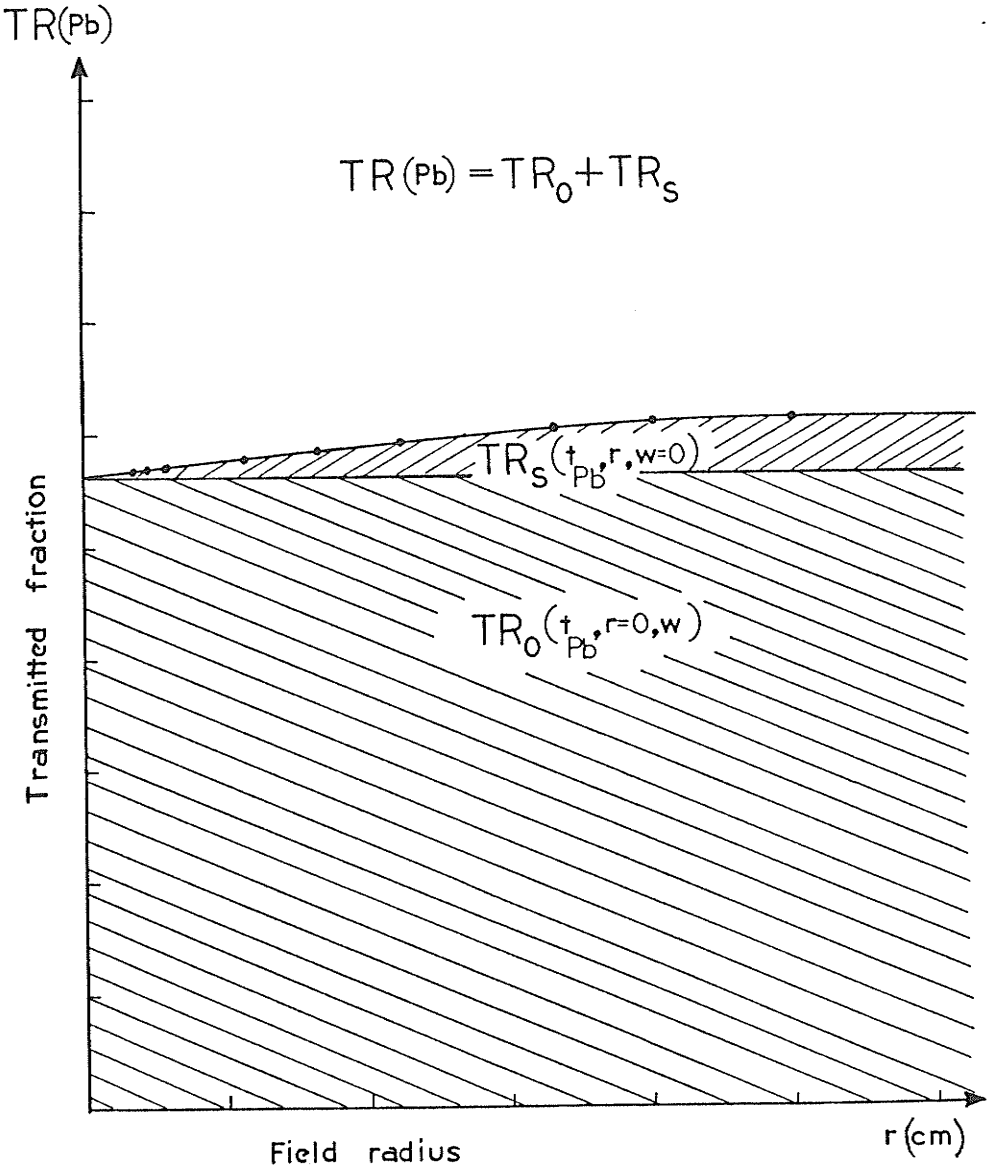
TR(Pb)
$TR(Pb) = TR_0 + TR_S$
$TR_S(t_{Pb}, r, w=0)$
$TR_0(t_{Pb}, r=0, w)$
Transmitted fraction
Field radius
r (cm)

scatter component, TR_S, is independent of the changes in the radiation spectrum across the beam. The off-axis changes in the scatter component are attributed exclusively to changes in the effective field size.

Furthermore, it has been assumed that the effective field size can be considered to consist of sectors of circular fields and that the scatter component for such circular fields does not depend on the off-axis position of the centre of the field. The last assumption is essential for the application of the sector integration technique to an off-axis calculation point and for the use of the sector integration technique as outlined by Clarkson (1941) and presented in section 4.2. This technique was originally introduced to calculate scattered radiation in a tissue; but is used here to calculate the scatter radiation in an attenuator.

Let us outline the steps involved in sector integration as applied to the calculation of the scatter component of the total transmittance.

The TR form a quantity that can be determined from measurements and can be tabulated as a means of describing radiation scattered from an irradiated volume. Their use can be illustrated by referring to Fig.(5.17).

This diagram shows a cross-section of a radiation beam. Point, P, is a point somewhere within the beam. The

Figure 5.17. Diagram showing the representation of a beam of rectangular cross-section by a summation of sectors of circular beams; is the angular width of one sector at an angle Θ and $R(\Theta)$ is its radius.

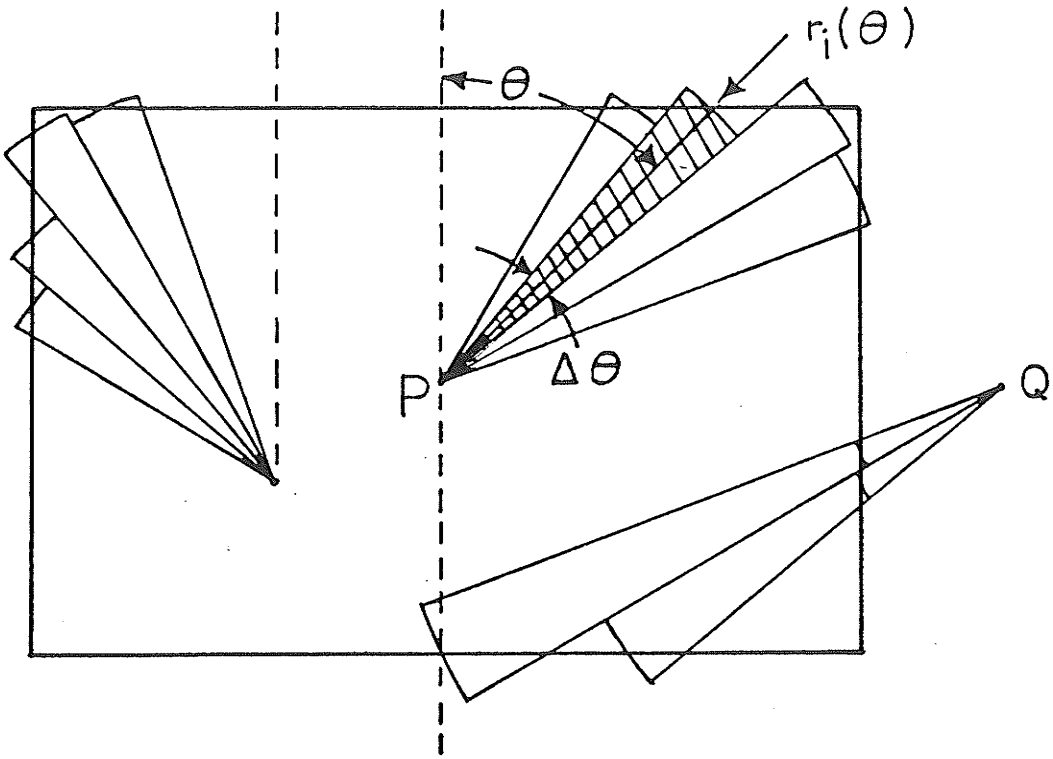
$r_i(\theta)$
θ
$\Delta\theta$
P
Q

crosshatched region is a sector of a circle with radius, r_i, and thickness, t_{Pb}. The contribution to TR_S from this sector at the point P can be taken as:

$$TR_S(t_{Pb}, r_i)\ (\Delta\theta/2\pi) \qquad 5.19$$

where $\Delta\theta$ is the angular width of a sector.

The whole of the irradiated volume can be covered by a series of such sectors and the scatter component of the total transmitted fraction of photons through the filter can be written as:

$$TR_S(t_{Pb}, P) = \sum_{i=1}^{n} \frac{\Delta\theta}{2\pi} TR_S(t_{Pb}, r_i) \qquad 5.20$$

where: $2\pi/n$ is the number of sectors required to cover the irradiated part of the attenuator and

$TR\ (t_{Pb}, r_i)$ is the scatter contribution to point , P, for a circular field of radius, r_i, and filter thickness, t_{Pb}.

The use of sectors of circular radiation beams to represent components of beams of any shape involves some simplifying assumptions:

1) The scattered radiation from each sector to the apex is the same in the circular beam (for which measured data is available) as it is in the actual beam, and the TR for a circular field does not depend on the off-axis position of the centre of the field.
2) It is assumed that the surface of the irradiated attenuator is at right angles to the ray from the

source to the point of calculation. This will not be true for points near an edge of the beam.

3) It is assumed that the radiation field is uniform across the sector .

When, for example, a wedge is present not a filter of uniform thickness, the thickness of the attenuator will vary at every point in the field. It has been shown by Cunningham (1978) that the scatter function can be differentiated so as to produce a quantity describing the amount of scatter reaching a point from a volume element. In order to do so, each angular sector has to be divided into radial elements, Δr, as shown on Fig.(5.18). A value of Δr can be made small enough to ensure a good accuracy of calculation. The contribution from each such element can be added separately, taking into account the thickness of the filter element at the position of each Δr element. Thus we can write TR_s as:

$$TR_s(t_{pb}, P) = \sum_{i=1}^{n} \frac{\Delta\theta}{2\pi} \sum_{r_i=0}^{R_i} \left[TR_s(t_{pb}, r_i) - TR_s(t_{pb}, r_i - \Delta r) \right] \quad 5.21$$

The total scatter contribution to a point P is obtained by summing the scatter along each sector, and finally by summing the total from each sector over the whole field. A program TRSCAT has been written which calculates the scatter component of the total transmittance at any point

Figure 5.18. Diagram showing a schematic representation of the geometry for the transmitted fraction calculation at point P due to scatter arising within a volume element through point Q. The right hand diagram shows the beam cross section through points P and Q.

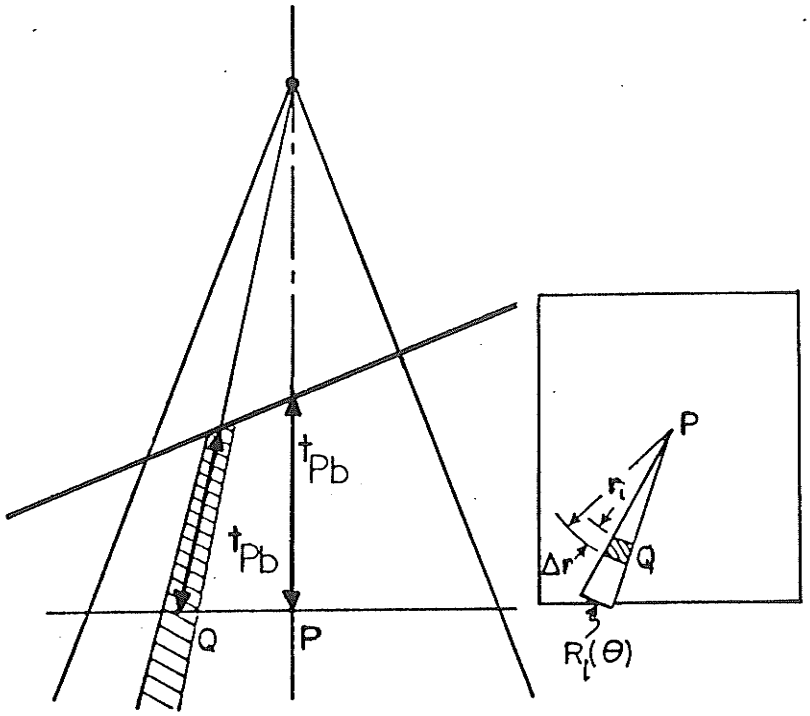
t_{Pb}
t_{Pb}
Q
P
P
r_i
Δr
Q
$R_i(\theta)$

for an arbitrary attenuator, for irregular fields, and which takes into account two dimensional attenuators. Filters are assumed to have the same cross-section along the length of the filter. The program TRSCAT was written in PASCAL for an IBM PC computer and is given in appendix B. At every point of calculation the primary component, TR_o, of the total transmitted fraction of photons through the attenuator has to be added to the scatter, TR_s. As was mentioned previously the energy spectrum, for example, for the 4MV x-ray linac varies with the distance from the central axis and this effect will cause the TR_o values to depend on the distance from the central axis. As has been shown in a previous section the TR_o can be expressed by a double exponential function of thickness of lead and distance from the central axis.
The total transmitted fraction of photons, TR can then be written as:

$$TR_p(t_{Pb}) = TR_o(t_{Pb}, w) + \sum_{i=1}^{n} \frac{\Delta\theta}{2\pi} \sum_{r_i=0}^{R_i} \left[TR_s(t_{Pb}, r_i) - TR_s(t_{Pb}, r_i - \Delta r) \right] \qquad 5.22$$

And the whole calculational concept is depicted in Fig.(5.19). This calculational method should allow for an accurate calculation of the total transmitted fraction TR through an arbitrary attenuator, at any point of

Figure 5.19. Diagram illustrating the sector integration method of calculating the transmitted fraction of photons at any point in the radiation field.

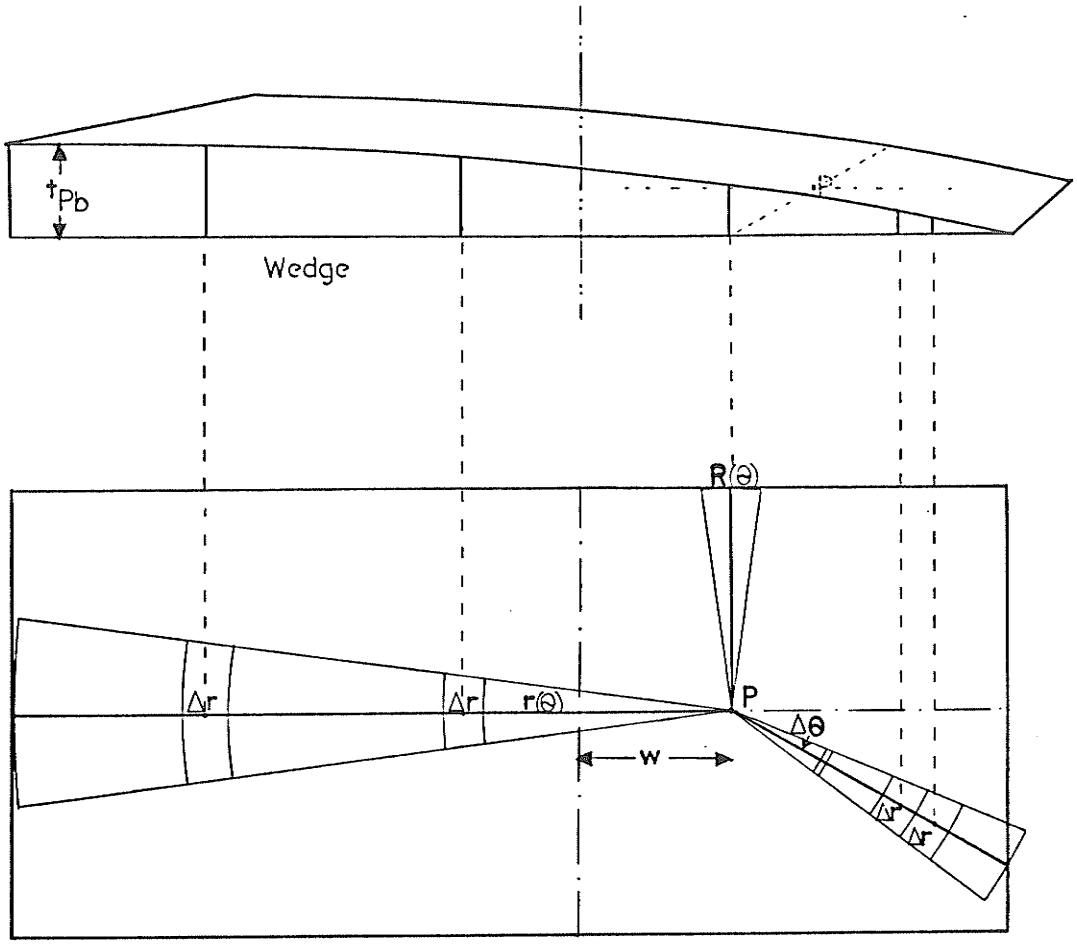
t_{Pb}
Wedge
R(θ)
Δr
Δr
r(θ)
P
Δθ
w
Δr
Δr

interest, provided the geometrical dimensions and transmission data are known.

The validity of the assumptions inherent in the above calculation algorithm were tested by comparing calculated and measured values of TR_S for a Pb slab of uniform thickness (5.33 mm) and of TR for the 45° wedge for the 4 MV SHM linac.

5.6.1. The calculational results.

The accuracy of the calculation was tested by comparing the measured and calculated TR values across given a attenuator and the calculated ones. The input data for the algorithm are the lookup tables containing the geometrical dimensions of the attenuator and scatter component values, TR_S, as given in Table 5.1. The TR_o is calculated using equation 5.15. The results for a 5.33 mm Pb slab is given in Table 5.2. The TR_o was measured at 2°, 5°, 7° and 9° off or 2.8, 7, 9.8 cm and 12.6 cm from the centre along a major axis of a 30x30 cm^2 field. The TR_o values can be obtained from equation 5.15, but for this particular slab they would be tha same as those given in Fig.(5.13). The calculated values for TR_S are given in Table 5.2 in the forth row. It can be seen from Fig.(5.20) that the largest difference between the measured and calculated TR values is % .

Table 5.2. The transmitted fraction values across the 30x30 cm^2 field at different points,for the 5.33 mm thick Pb slab.

TR_m - measured TR

TR_o - zero area TR

TR_s - scatter contribution, measured

TR_{sc} - scatter contribution, calculated

	α - angle off the central axis				
	0°	2°	5°	7°	9°
5.3mm					
TR_m	.728	.724	.717	.705	.690
TR_o	.694	.691	.684	.676	.663
TR_s	.034	.033	.033	.029	.027
$TR_{Sc.}$	.033	.033	.032	.024	.019

Figure 5.20. The errors between measured and calculated TR values for a 5.33 mm slab.

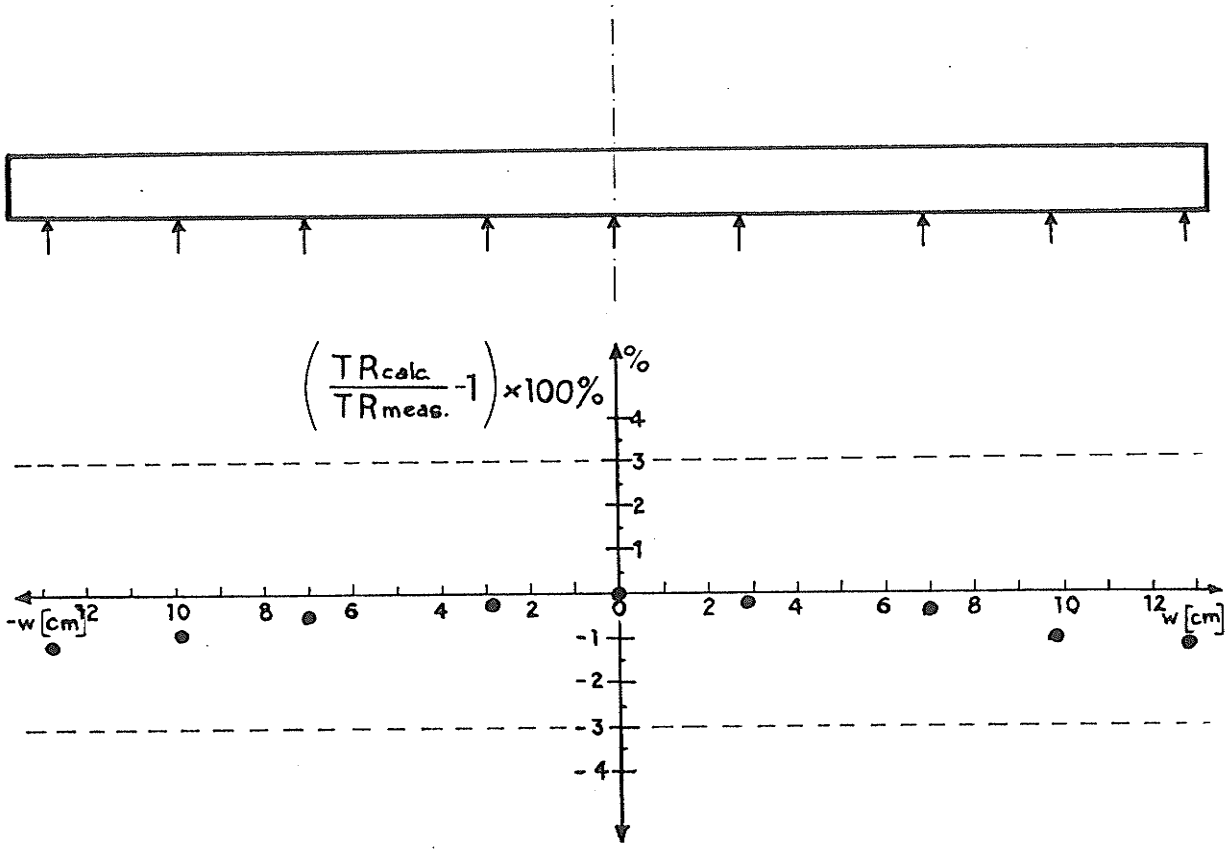
$\left(\frac{TR_{calc.}}{TR_{meas.}}-1\right)\times 100\%$
%
4
3
2
1
-1
-2
-3
-4
-w [cm]
12
10
8
6
4
2
0
2
4
6
8
10
12
w [cm]

The next test was done for a 45° wedge for the 4 MV SHM linac. The total transmitted fractions of photons across this wedge have been measured and the comparison with the calculated values for the same irradiation conditions are shown in Table 5.3 and in Fig.(5.21). Table 5.3 contains the TR values for the 45° wedge for the 4 MV SHM linac, as measured for the thickness of the portion of the filter along appropriate raylines. The TR_o values are added to the scatter component, TR_s, calculated for the same point and which are tabulated in the last column of this table. The errors between measured and calculated TR values are shown in Fig.(5.22). The largest error is 2.5 % at the thin end of the 45° wedge. This disagreement is mainly due to the fact that the values of the TRs are measured with a large ionization chamber which detects photons coming from the portion of the wedge of rapidly changing thickness, thus the field gradient across the ion chamber occurs and the measured values tend to be overestimated.

Table 5.3. The measured TR and calculated TR_S values for the 45° wedge for 4 MV SHM linac.

distance from the central axis w (cm)	wedge thickness along rayline t_{Pb} (mm)	TR_o	$TR_{Scal.}$
-8.4	16.5	.330	.022
-7	16.5	.345	.024
-5.6	15.8	.360	.025
-4.2	14.9	.383	.025
-2.8	13.6	.415	.025
0	11.45	.481	.025
2.8	8.55	.585	.023
4.2	6.7	.657	.023
5.6	3.85	.778	.019
7	0.7	.939	.019

Figure 5.21. Comparison of measured and calculated transmitted fractions across the 45° wedge. Bottom part shows the transmitted fractions as a function of the distance from the central axis.

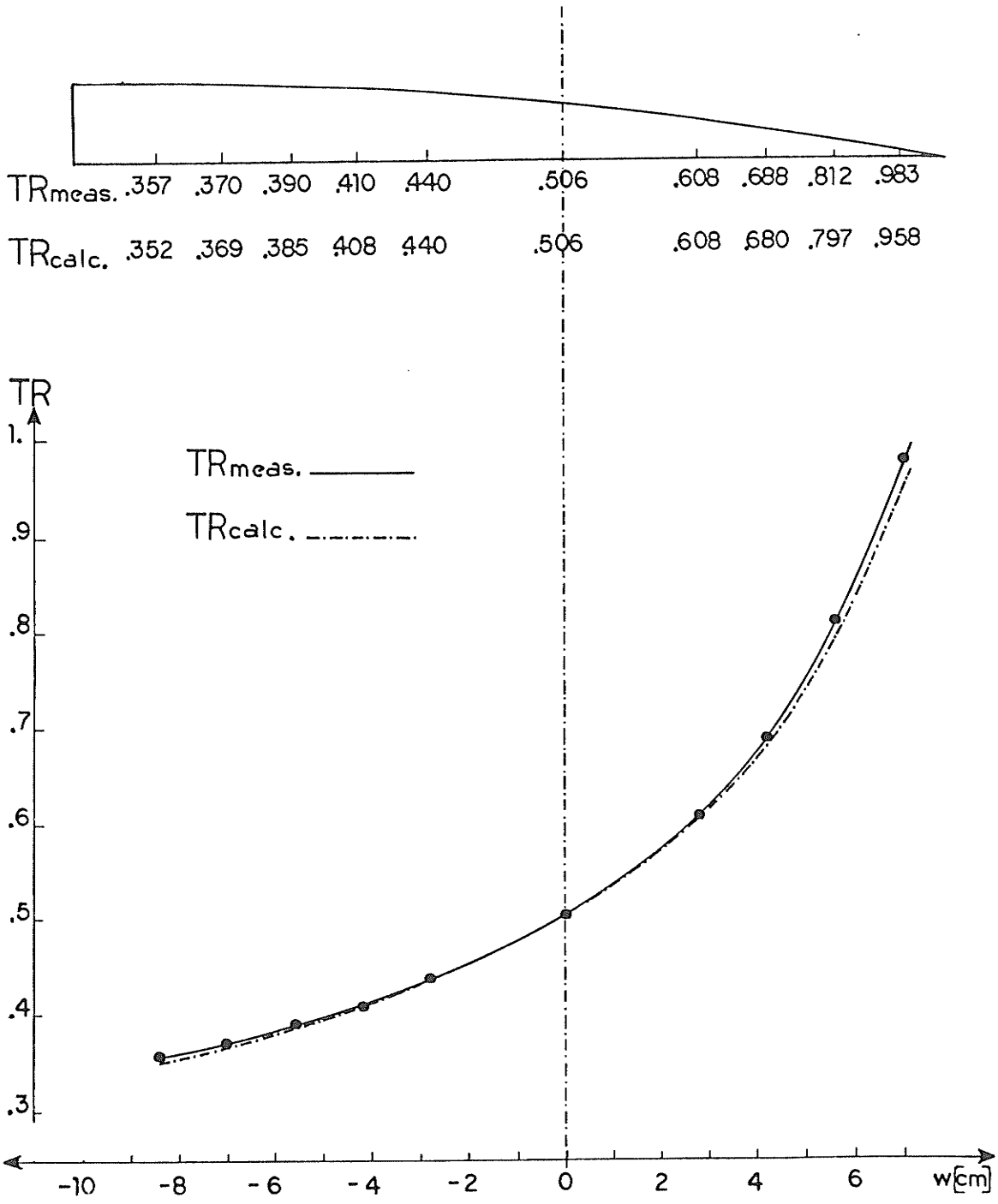
TRmeas. .357 .370 .390 .410 .440 .506 .608 .688 .812 .983
TRcalc. .352 .369 .385 .408 .440 .506 .608 .680 .797 .958
TR
1.
.9
.8
.7
.6
.5
.4
.3
TRmeas.
TRcalc.
-10 -8 -6 -4 -2 0 2 4 6
w[cm]

Figure 5.22. The errors between measured and calculated TR values for 45° wedge for 4 MV SHM linac.

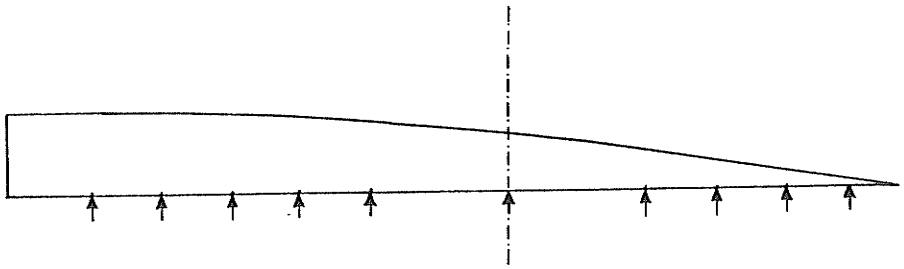

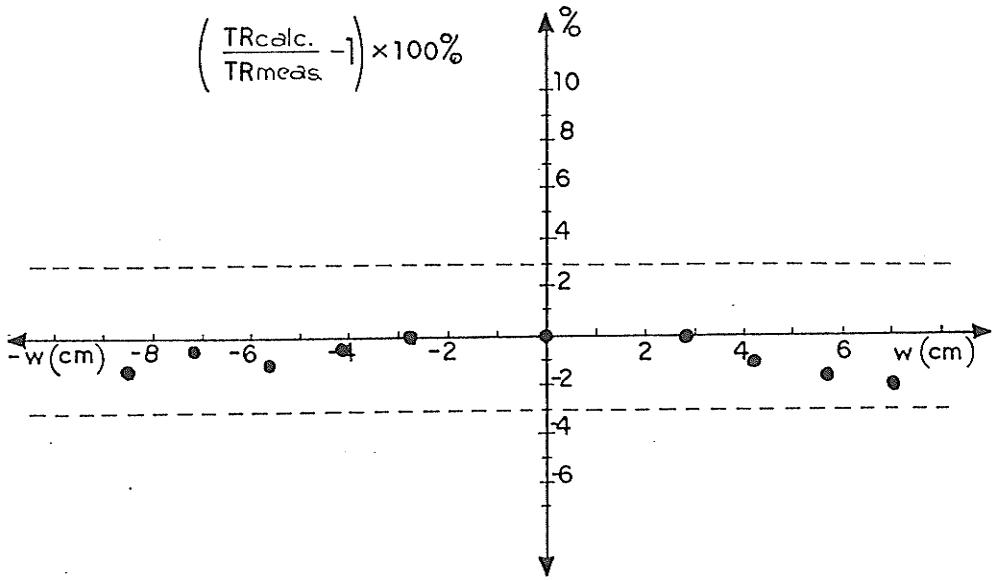
$\left(\frac{TR_{calc.}}{TR_{meas.}} - 1\right) \times 100\%$
%
10
8
6
4
2
-2
-4
-6
-w (cm)
-8
-6
-4
-2
2
4
6
w (cm)

5.6.2. The final dose distribution calculation.

The third test and the main one for the whole calculational concept is to determine the extent of an agreement that can be obtained between measured and calculated dose distributions in a phantom at a depth of 10 cm, which is the standard acceptance test for all beam modifiers in use. In order to do so the measured and calculated beam profiles are needed at this standard depth for the same irradiation conditions, namely: field size, source to surface distance and source to wedge distance. The beam profiles for an open field and a field altered by the 20° wedge for a Co-60 beam are shown in Fig.(5.23). The profiles are measured in a water phantom at the depth of 10 cm for a 18x18 cm^2 field size as defined at the surface of the phantom. The beam profiles for 45° wedge and open field for the 4 MV SHM linac are depicted in Fig.(5.24), for a 19x19 cm^2 field size. Using the calculated TR values as input wedge data for the dose distribution calculation algorithm (AECL Theraplan) the beam profiles for the same irradiation conditions as the measured ones were obtained. Both calculated and measured profiles are shown in Fig.(5.25) for Co-60 and in Fig.(5.26) for 4 MV linac. The results of the comparison of the calculated beam profile and the measured one in terms of the percentage error between

Figure 5.23. The Co-60 beam profiles for an open field and modified field altered by the 20° wedge.

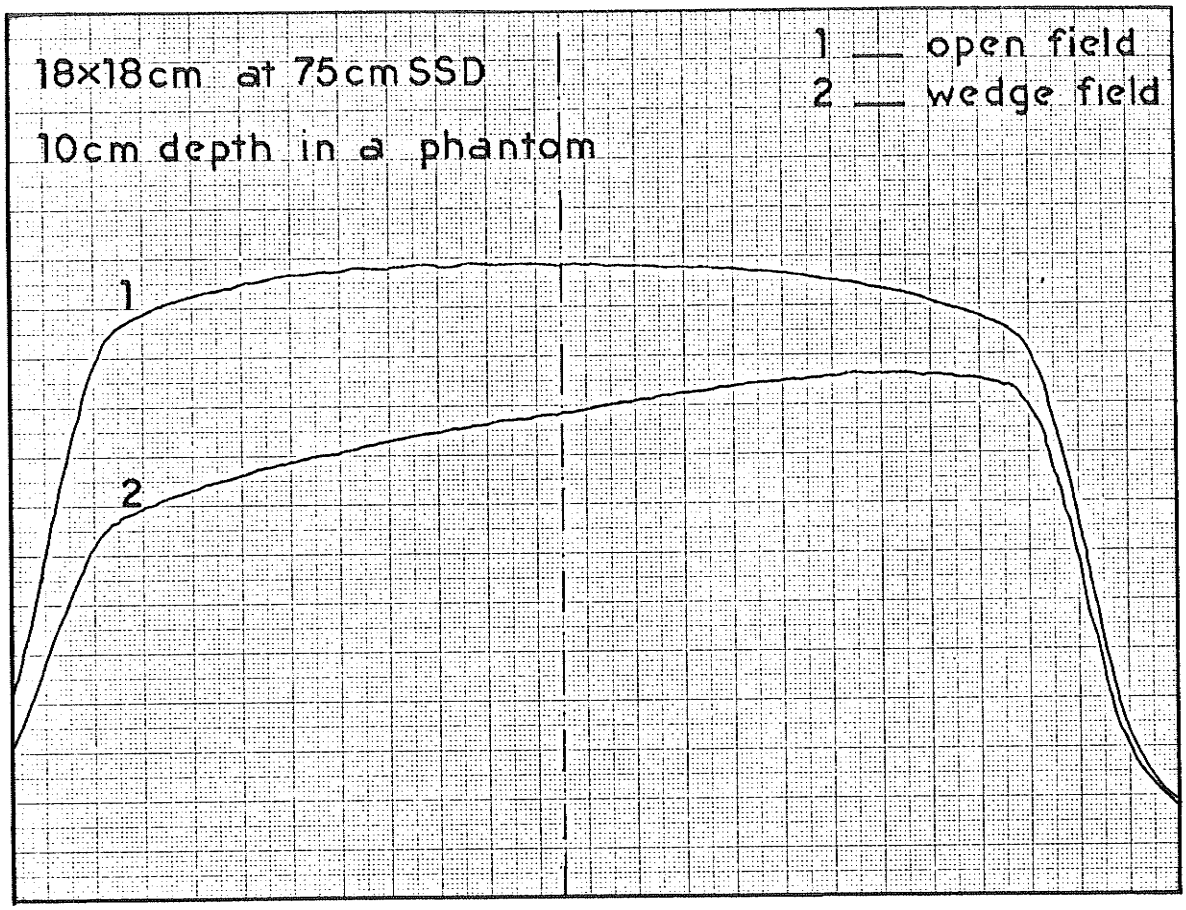
18×18cm at 75cm SSD
10cm depth in a phantom
1 — open field
2 — wedge field
1
2

Figure 5.24. The beam profiles for 45° wedge and open field for the 4 MV SHM linac.

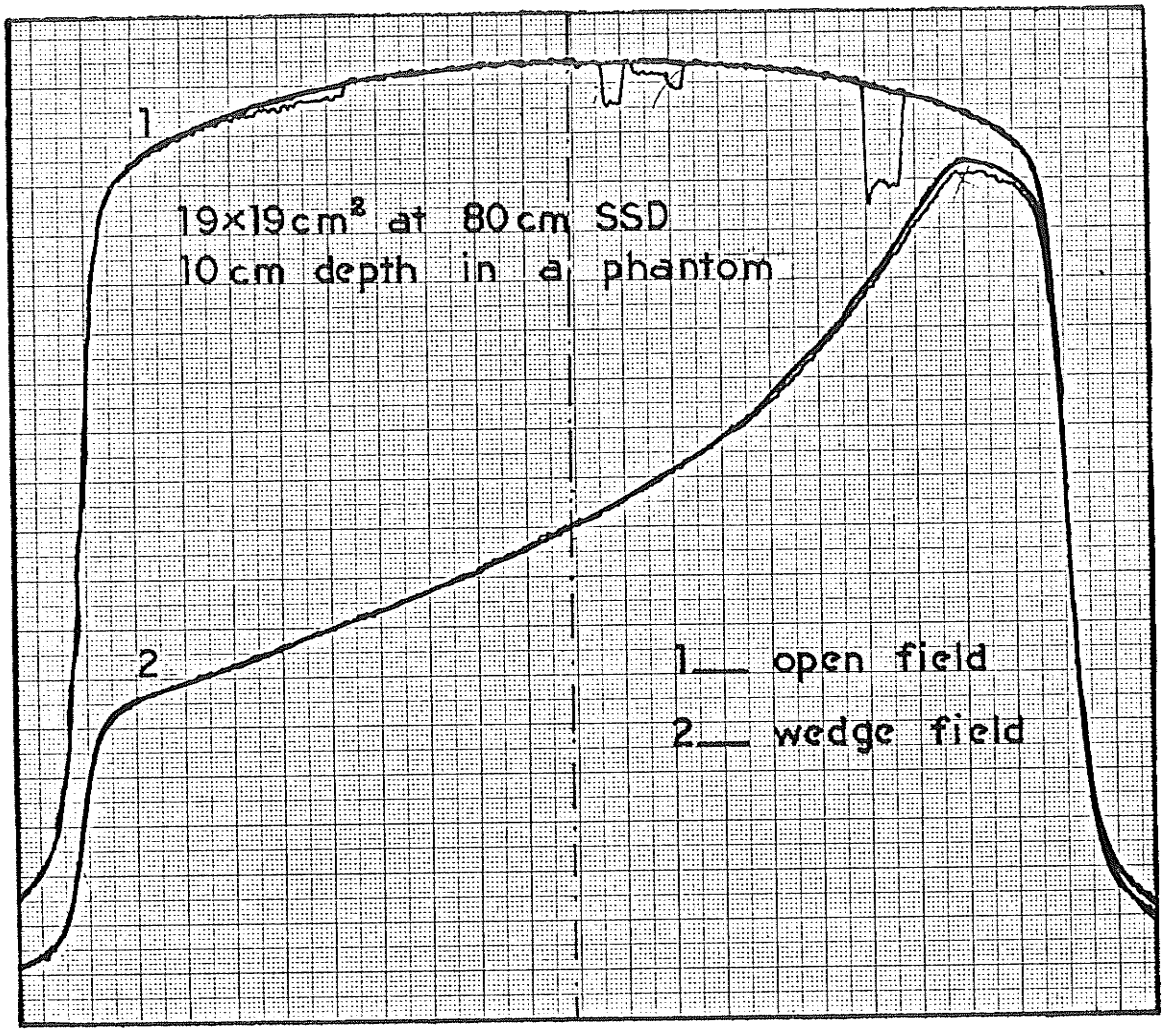
1
19×19cm² at 80cm SSD
10cm depth in a phantom
2
1___ open field
2___ wedge field

Figure 5.25. The calculated and measured beam profiles for 20° wedge for CO-60.

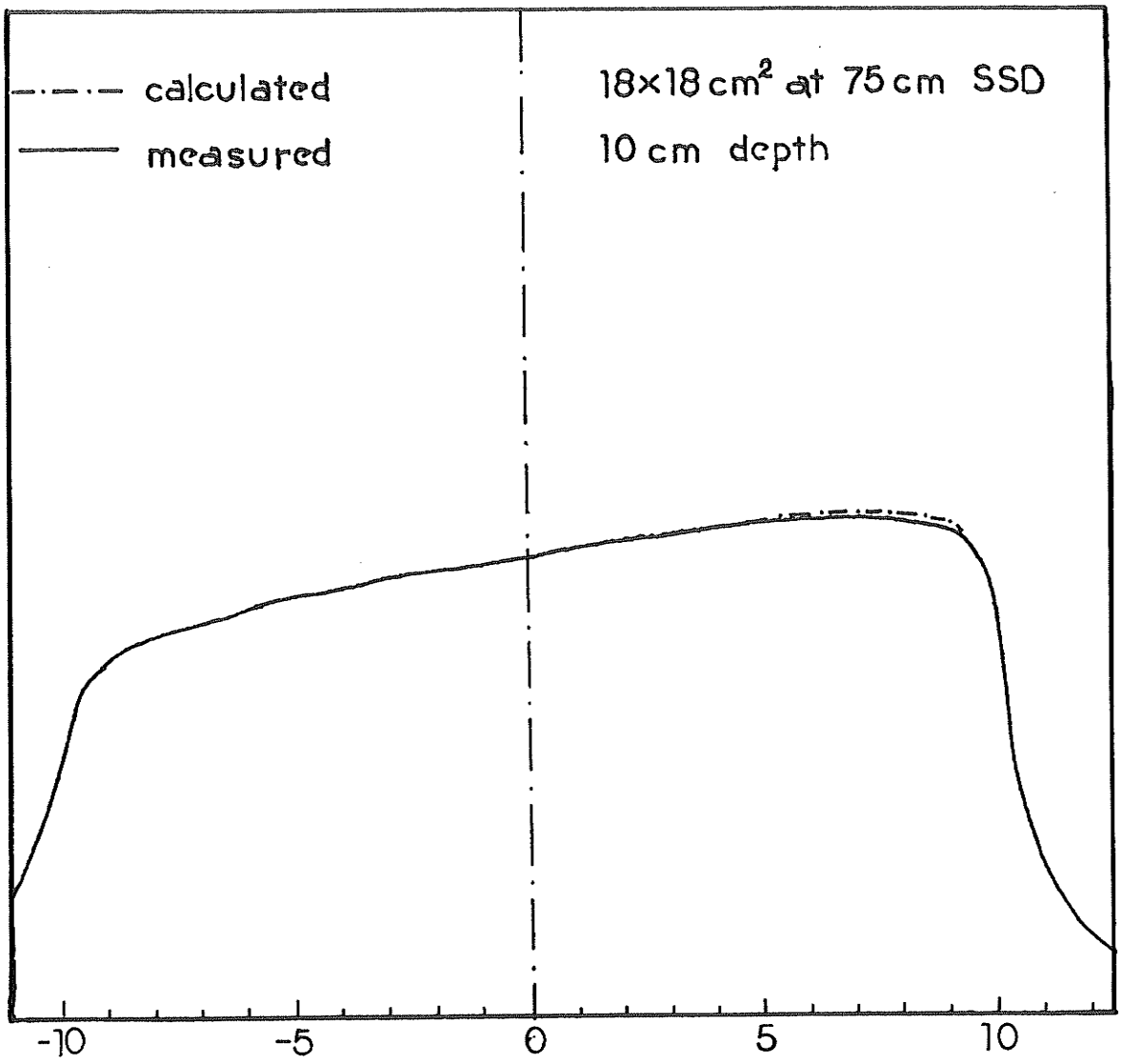
calculated
measured
18×18 cm² at 75 cm SSD
10 cm depth
-10
-5
0
5
10

Figure 5.26. The calculated and measured beam profiles for 45° wedge for the 4 MV linac.

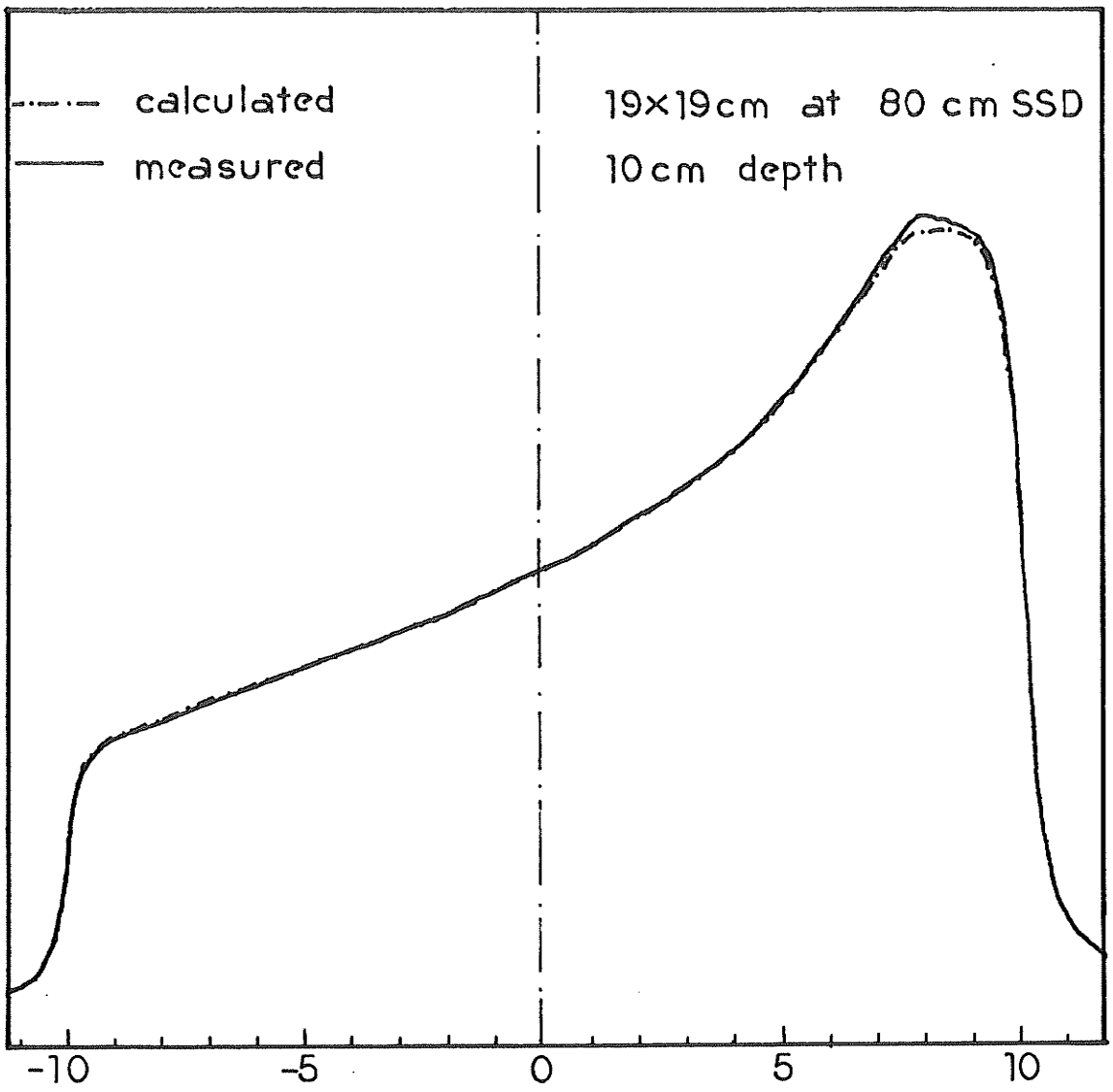
calculated
measured
19×19cm at 80 cm SSD
10cm depth
-10
-5
0
5
10

those two beam profiles are shown in Fig.(5.27) and in Fig.(5.28) for a 20° wedge for Co-60 and a 45° wedge for the 4 MV linac respectively. The errors vary from 0-2.7 %, the largest being recorded at the thin end of the wedges. The comparison with the Fig.(5.4) which shows the errors involved when the existing dose calculation procedure is used, reveals that most of the improvement was obtained at the thicker part of the wedge.

For the real situation when the patient is treated the surface is not flat, which means that the depth of calculation changes throughout the field. The calculational method described and tested as above does not take into account the effect of the source to point of calculation distance on the TRs. To test if this method can be used for points at different depths, the comparison of the calculated and measured beam profiles, for a 45° wedge for the 4 MV linac, at 5 cm and 15 cm depth in a water phantom was done. Both calculated and measured profiles are shown in Fig.(5.29) and Fig.(30). The results of the comparison of the calculated and measured beam profiles are presented in terms of the percentage error between those two beam profiles at two different depth are shown in Fig.(5.31). One can see that the errors are increasing with depth, but are within a 3 % limit, which still is considered to be acceptable. It

Figure 5.27. Comparison of the measured and calculated beam profiles for a 20° wedge for Co-60.

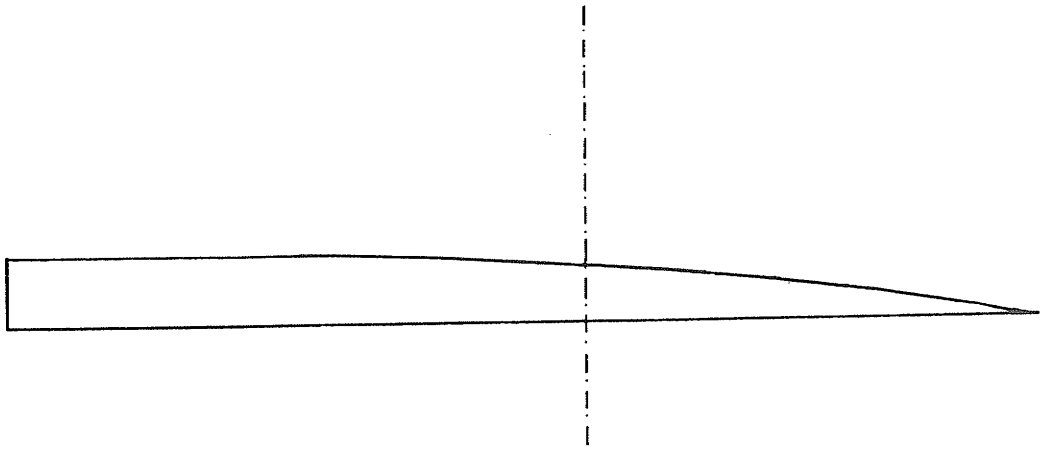

$$\left(\frac{D_{calc.}}{D_{meas.}} - 1\right) \times 100\%$$

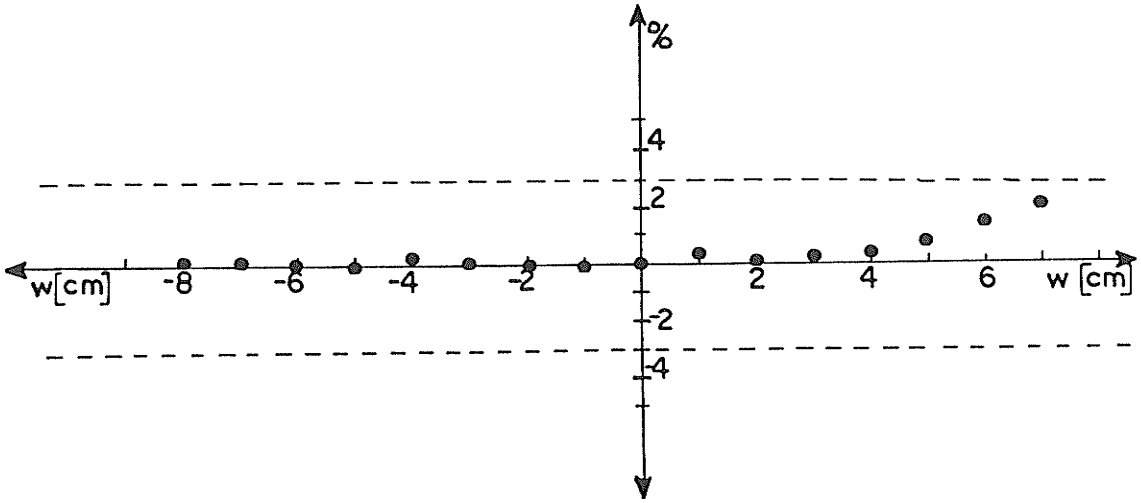

Figure 5.28. Comparison of the measured and calculated beam profiles for a 45° wedge for the 4 MV linac.

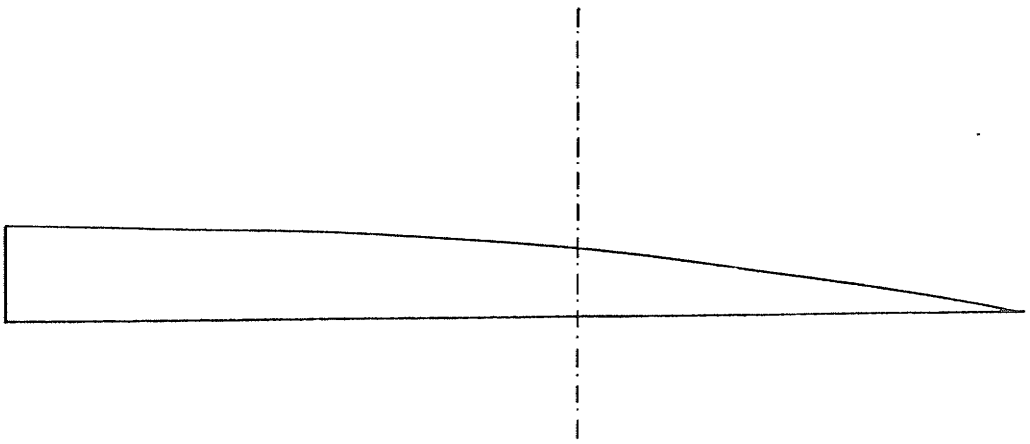

$$\left(\frac{D_{calc.}}{D_{meas.}} - 1\right) \times 100\%$$

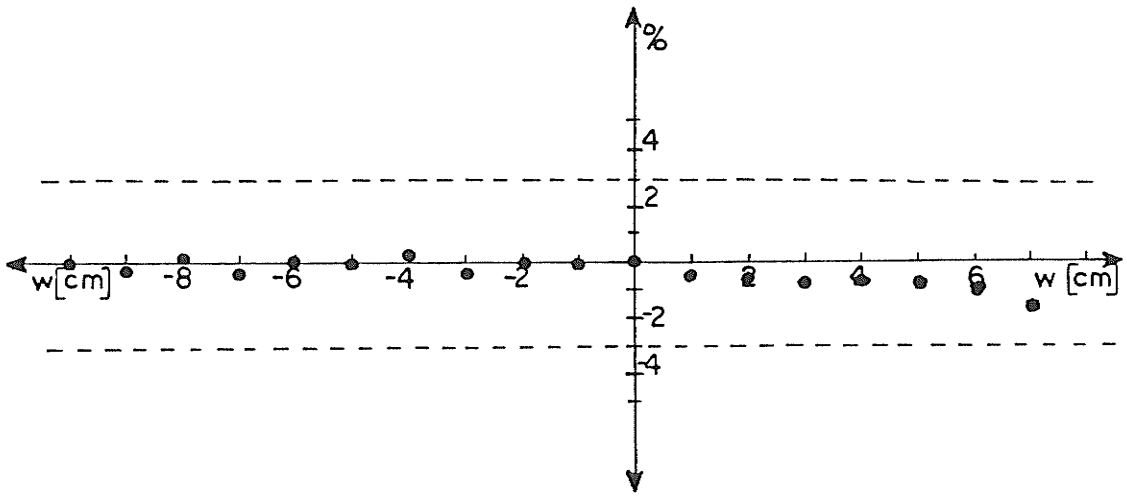

Figure 5.29. The calculated and measured beam profiles at 5 cm depth, for a 45° wedge for the 4 MV linac.

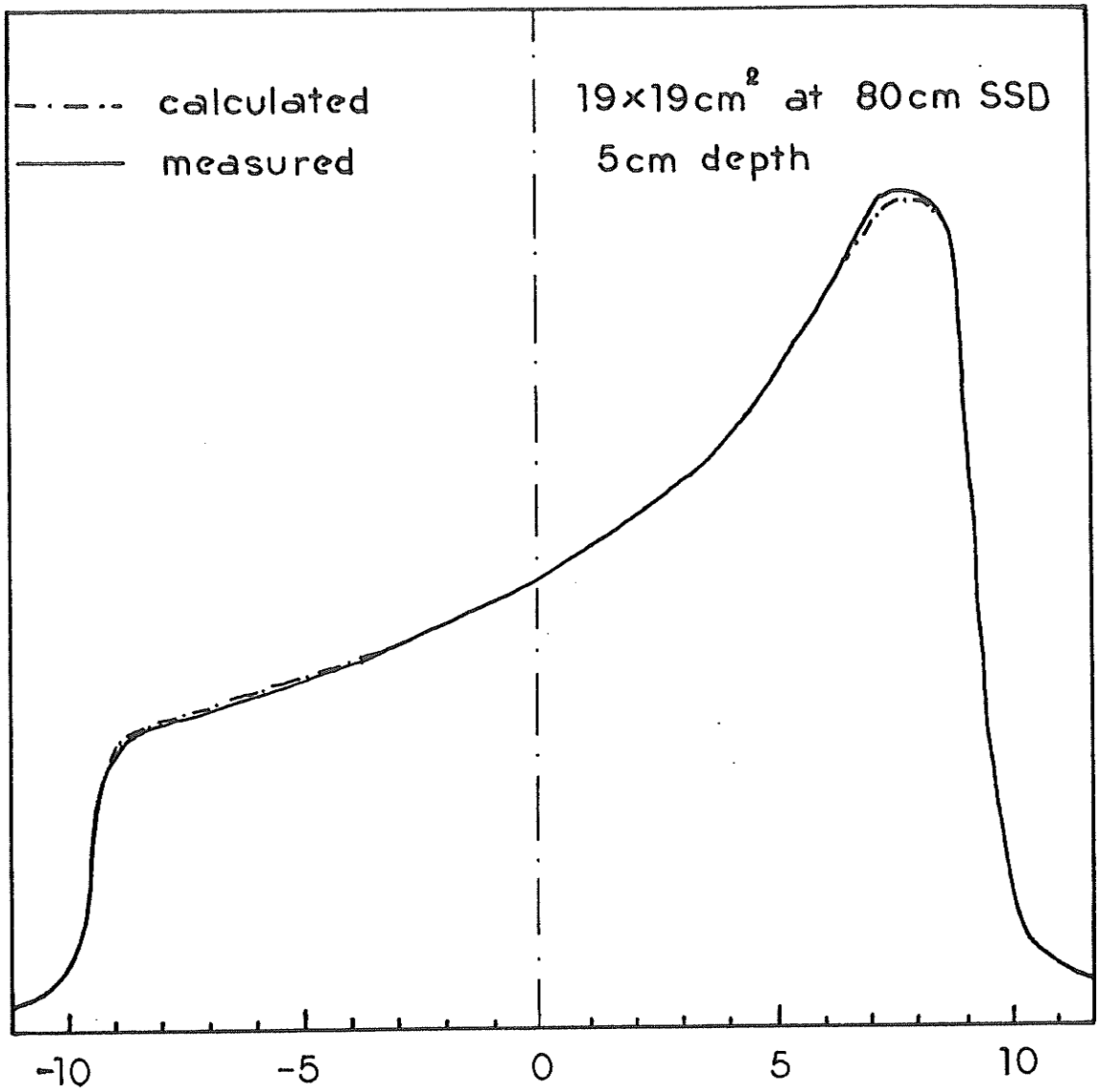
calculated
measured
19×19cm² at 80cm SSD
5cm depth
-10
-5
0
5
10

Figure 5.30. The calculated and measured beam profiles at 15 cm depth, for a 45° wedge for the 4 MV linac.

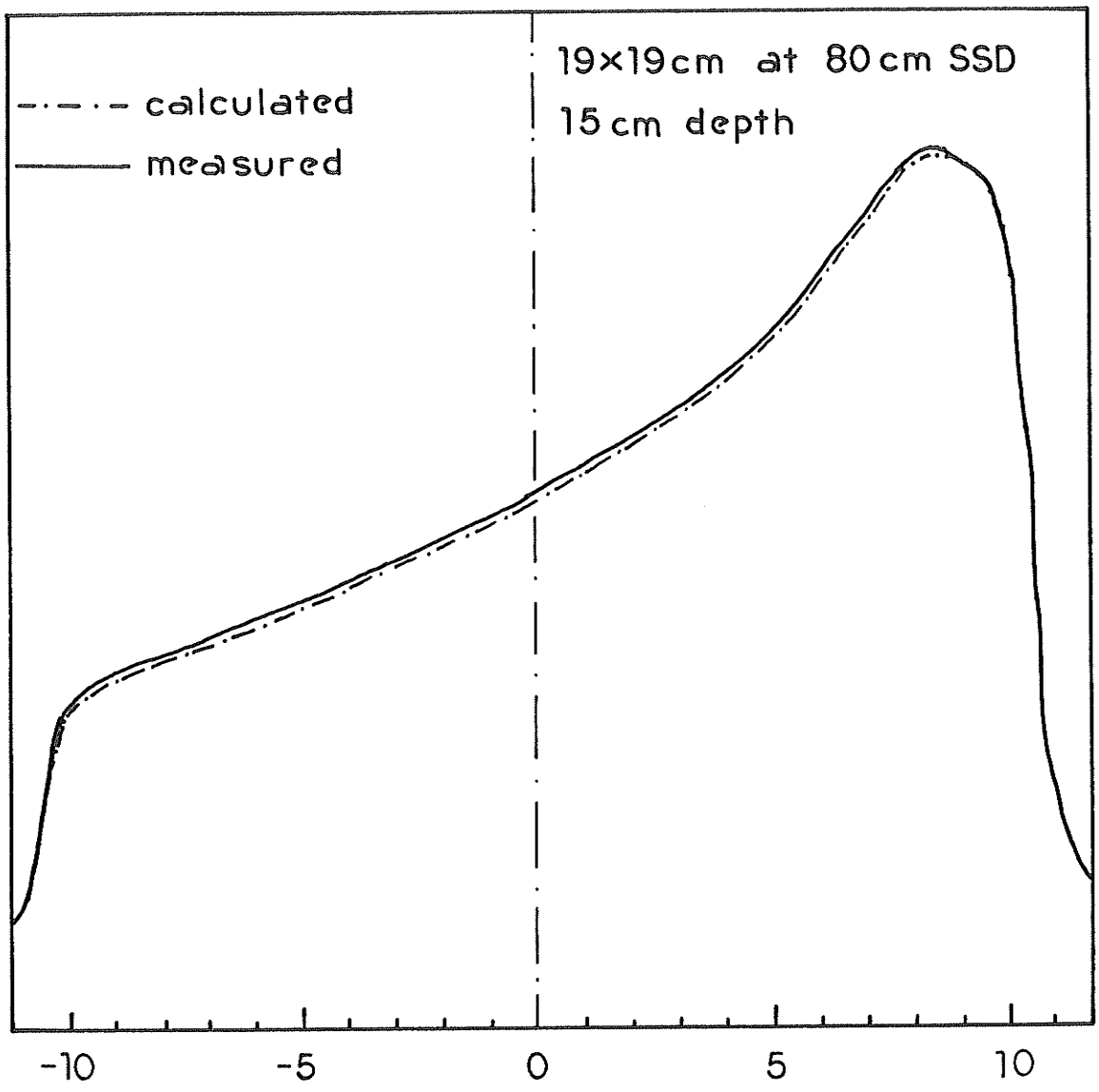
19×19cm at 80cm SSD
15cm depth
calculated
measured
-10
-5
0
5
10

Figure 5.31. Comparison of the measured and calculated beam profiles, at 5 cm and 15 cm depths for a 45° wedge for the 4 MV linac.

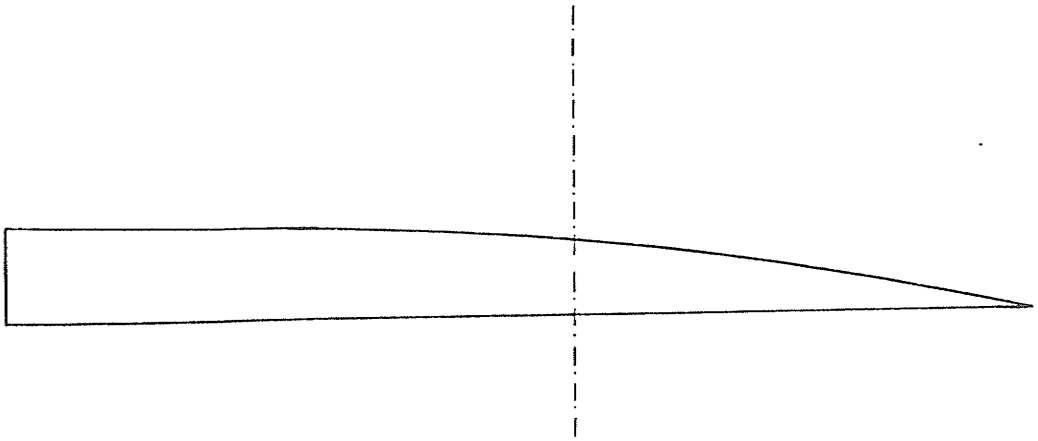

x 5cm

• 15cm

$$\left(\frac{D_{calc.}}{D_{meas.}} - 1\right) \times 100\%$$

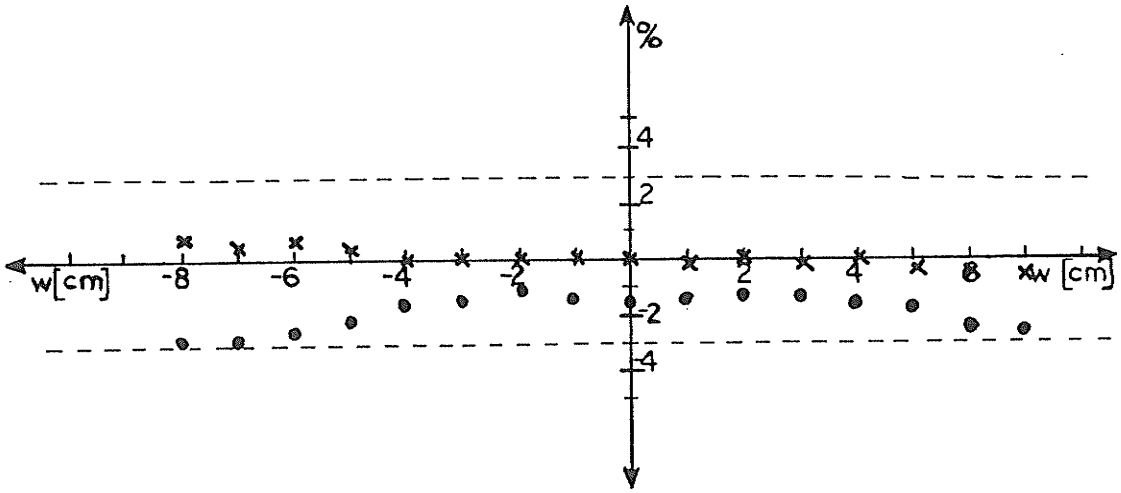

appears that for the geometries with different SSD than considered in this project one should use the transmission data measured for the particular set up, to avoid large, unacceptable errors in dose calculation.

VI. CONCLUSIONS

The work presented in this report was undertaken in an effort to improve the dose distribution calculation whenever beam modifying devices are inserted into the radiation beam using the Theraplan dose calculation algorithm. With this algorithm which is a part of the treatment planning program in use in the Manitoba Cancer Treatment and Research Foundation one can expect errors in dose calculation as high as 8% when for example a wedge is used. The goal to be achieved was to reduce those errors below 3%. The basic concept relies on the assumption that the presently used algorithm takes care of the changes of the attenuating and scattering conditions in a phantom, and that the hardening effects caused by the introduction of the lead attenuator into the photon beam is small enough not to affect the TAR values used in the dose calculation. For the amount of lead used for typical compensators or wedges and for the depth in phantom of 10 cm this assumption proved to be reasonable. Thus the only modification to the presently used calculations which is required to improve these calculations in the determination of the transmitted fraction of photons for the attenuator, TR, (at every point of interest). These calculated TR essentially are cor-

rection factors to be applied to the dose at a point in a phantom without the attenuator to get the dose to the same point when an attenuator is in the radiation beam, and they can be used as input wedge data for further dose distribution calculations. It was shown that such calculation improved the accuracy to the extend of being able to keep the errors within the 3% limit.

All experiments were performed with the attenuators covering the whole radiation beam. Further work is needed to solve problems involved in a situation of partially blocked fields, when beam altering devices cover only a part of the radiation beam. The calculation method developed for this project does not predict, for example the penumbra effect on the edge of a block.

APPENDIX A.

The behaviour of the scatter component of the transmitted fraction of photons through the attenuator for 4 MV X-rays as a function of radius is shown in Figure (A.1) for the 1.5 cm thick attenuator. It is a typical curve, which increases at first rapidly with an increasing radius and then more slowly, tending to level off for large radii. For computer work is convenient to store a table of data and use look-up and interpolation procedures than to fit such curves to analytical functions. The circles on the curve for $TR_S(t_{Pb}, r)$ are at equivalent radii, for which measurements have been made. There are no measurements either for very small radii or very large radii, and, in fact, for radii greater than 14 cm. The $TR_S(t_{Pb}, r)$ divided by radius forms a function which varies less rapidly than does the TR_S itself, and is shown on the Figure (A.1) as a dashed curve. This function, $TR_S(t_{Pb}, r)/r$ can be used as an aid in extrapolating the data for large radii. The TR_S gradually increases as the radius increases. $TR_S(t_{Pb}, r)/r$, except for the initial portion of the curve, must smoothly decrease towards zero. The extrapolation of the TR_S/r function to 0 value for very large radius was used to obtain $TR_S(t_{Pb}, r)$ for large radii.

Figure A.1. The scatter component of the transmitted fraction of photons for circular beams plotted against the radius of the beam for 1.5 cm thick attenuator for 4 MV X-rays. The curve shown as dashed line is the $TR_S(t_{eq}, r)/r$ and refers to the ordinate scale on the right.

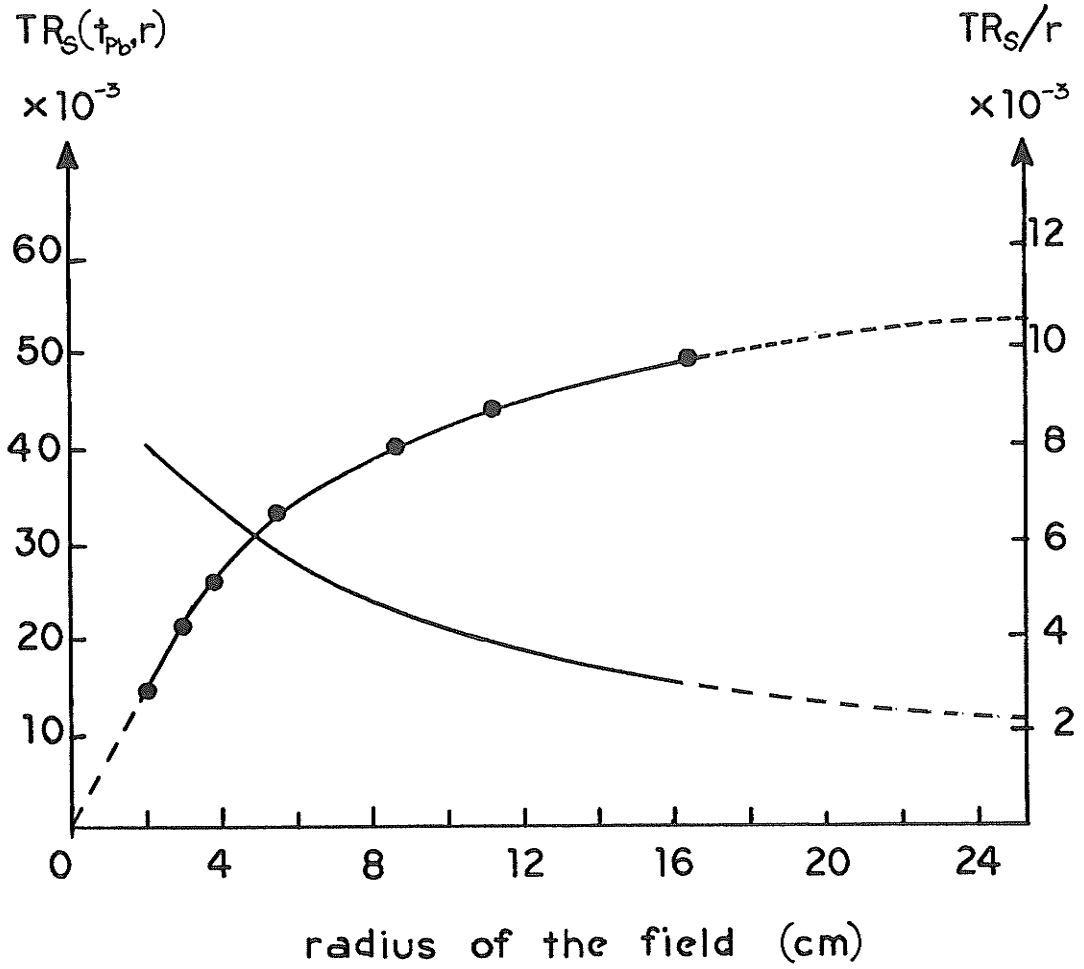
$TR_S(t_{Pb},r)$
$\times 10^{-3}$
TR_S/r
$\times 10^{-3}$
60
50
40
30
20
10
12
10
8
6
4
2
0
4
8
12
16
20
24
radius of the field (cm)

APPENDIX B. Program TRSCAT;

```
type
   row   = array[1..20] of real;
   arr   = array[1..15,1..15] of real;
   sdata = record
                n : integer;
                m : integer;
                s : arr;
           end;
   rdata = record
                n : integer;
                r : row;
           end;

Var
   i,nw,Nc,ip,n,j,ni,nj,L,Jd,nri,k,w:integer;

   x1,y1,x2,y2,vec,v,cross,ze,zeta,g,theta,xzero,yzero,
   dnom,phi,delta,delt,psi,ri,sc1,sc2,SCAT,Dc,delr,ri2,
   rid,cor2,ther,gar,  xri,scat1,coga,scat2:real;

   X,Y:array[1..12] of real;
   sar:arr;
   sardat : sdata;
   sarfile : file of sdata;
   rfile,wfile,xrfile : file of rdata;
   R,Dep,wedge,XR:   row;
   rdat,depdat,wdat,xrdat :rdata;
   noloop : boolean;
   ch : char;
   filename : string[12];
begin

   {This part of the program reads in sar, r, dep, wedge,
    XR,ni, nj, and nw from files}
   writeln('Default names for files?');
   read(kbd,ch);
   if ch = 'y' then
   begin
     assign(sarfile,'sar.dat');
     reset(sarfile);
     read(sarfile,sardat);
     ni := sardat.n;
     nj := sardat.m;
     sar := sardat.s;
     close(sarfile);
     assign(rfile,'r.dat');
```

```
      reset(rfile);
      read(rfile,rdat);
      if rdat.n <> ni then writeln('WARNING sar and R have
      incompatible sizes');
      R := rdat.r;
      close(rfile);
      assign(rfile,'dep.dat');
      reset(rfile);
      read(rfile,depdat);
      if depdat.n <> nj then writeln('WARNING sar and Dep
      have incompatible  sizes');
      Dep := depdat.r;
      close(rfile);
      assign(wfile,'wedge.dat');
      reset(wfile);
      read(wfile,wdat);
      nw := wdat.n;
      wedge := wdat.r;
      close(wfile);
      assign(xrfile,'xr.dat');
      reset(xrfile);
      read(xrfile,xrdat);
      if nw <> wdat.n then writeln('WARNING NW is
different');
      xr := xrdat.r;
      close(xrfile);
    end
    else
    begin

      begin
        {read from file}
        writeln('enter name of file containing sar');
        {$I-}
        repeat
          noloop := true;
          readln(filename);
          if IOresult <> 0 then
          begin
            writeln('enter a legal file name, e.g.
            a:sar.dat');
            noloop := false;
          end;
        until noloop;
        {$I+}
        assign(sarfile,filename);
        reset(sarfile);
        read(sarfile,sardat);
        ni := sardat.n;
        nj := sardat.m;
```

```
   sar := sardat.s;
   close(sarfile);
   writeln('do you wish to see sar ? (y/n)');
   read(kbd,ch);
   if ch = 'y' then
   begin
      for i := 1 to nj do
      begin
         clrscr;
         writeln('row ',i:2);
         for j := 1 to ni do
         begin
            writeln(j:2,'     :     ',sar[i,j]:15:5);
         end;
         writeln('press any key to continue');
         repeat
         until keypressed;
      end;
   end;
end;

begin
   {read from file}
   writeln('enter name of file containing R');
   {$I-}
   repeat
      noloop := true;
      readln(filename);
      if IOresult <> 0 then
      begin
         writeln('enter a legal file name, e.g.
         a:R.dat');
         noloop := false;
      end;
   until noloop;
   {$I+}
   assign(rfile,filename);
   reset(rfile);
   read(rfile,rdat);
   if rdat.n <> ni then writeln('WARNING sar and R
   have incompatible sizes');
   R := rdat.r;
   close(rfile);
   writeln('do you wish to see R ? (y/n)');
   read(kbd,ch);
   if ch = 'y' then
   begin
         clrscr;
         for j := 1 to ni do
         begin
```

```
            writeln(j:2,'     :     ',r[j]:15:5);
        end;
        writeln('press any key to continue');
        repeat
        until keypressed;
    end;

    {read from file}
    writeln('enter name of file containing Dep');
    {$I-}
    repeat
       noloop := true;
       readln(filename);
       if IOresult <> 0 then
       begin
          writeln('enter a legal file name, e.g.
          a:Dep.dat');
          noloop := false;
       end;
    until noloop;
    {$I+}
    assign(rfile,filename);
    reset(rfile);
    read(rfile,depdat);
    if depdat.n <> nj then writeln('WARNING sar and Dep
    have incompatible sizes');
    Dep := depdat.r;
    close(rfile);
    writeln('do you wish to see Dep ? (y/n)');
    read(kbd,ch);
    if ch = 'y' then
    begin
        clrscr;
        for j := 1 to nj do
        begin
           writeln(j:2,'     :     ',dep[j]:15:5);
        end;
        writeln('press any key to continue');
        repeat
        until keypressed;
    end;
end;

     writeln('enter name of file containing wedge');
    {$I-}
    repeat
       noloop := true;
       readln(filename);
       if IOresult <> 0 then
       begin
```

```
        writeln('enter a legal file name, e.g.
        a:R.dat');
        noloop := false;
      end;
    until noloop;
    {$I+}
    assign(wfile,filename);
    reset(wfile);
    read(wfile,wdat);
    nw := wdat.n;
    wedge := wdat.r;
    close(wfile);
    writeln('do you wish to see wedge ? (y/n)');
    read(kbd,ch);
    if ch = 'y' then
    begin
        clrscr;
        for j := 1 to nw do
        begin
          writeln(j:2,'    :    ',wedge[j]:15:5);
        end;
        writeln('press any key to continue');
        repeat
        until keypressed;
    end;

    writeln('enter name of file containing XR');
    {$I-}
    repeat
      noloop := true;
      readln(filename);
      if IOresult <> 0 then
      begin
        writeln('enter a legal file name, e.g.
        a:R.dat');
        noloop := false;
      end;
    until noloop;
    {$I+}
    assign(xrfile,filename);
    reset(xrfile);
    read(xrfile,xrdat);
    if nw <> wdat.n then writeln('WARNING NW is
different');
    xr := xrdat.r;
    close(xrfile);
    writeln('do you wish to see XR ? (y/n)');
    read(kbd,ch);
    if ch = 'y' then
    begin
```

```
            clrscr;
            for j := 1 to nw do
            begin
               writeln(j:2,'     :     ',xr[j]:15:5);
            end;
            writeln('press any key to continue');
            repeat
            until keypressed;
      end;
end;

  Writeln('enter no of corners');
  {$I-}
  repeat
  begin
     noloop := true;
     readln(nc);
     if IOresult <> 0   then
     begin
        writeln('please enter an integer between 1 and
        12');
        noloop := false;
     end
     else
     begin
        if (nc <= 0) or (nc > 12) then
        begin
           writeln('please enter an integer between 1 and
           12');
           noloop := false;
        end;
     end;
  end;
  until noloop;
  {$I+}
  For i:=1 to nc do
  begin
     writeln ('Enter coord of corner  ',i);
     {$I-}
     repeat
        noloop := true;
        readln(x[i],y[i]);
        if IOresult <> 0 then
        begin
           writeln('please enter two real numbers
           separated by a blank');
           noloop := false;
        end;
     until noloop;
     {$I+}
```

```
end;
x[nc+1] := x[1];
y[nc+1] := y[1];
writeln('origin');
{$I-}
repeat
   noloop := true;
   readln(xzero,yzero);
   if IOresult <> 0 then
   begin
      writeln('please enter two real numbers separated
      by a blank');
      noloop := false;
   end;
until noloop;
{$I+}

writeln('Enter Dc');
{$I-}
repeat
   noloop := true;
   readln(Dc);
   if IOresult <> 0 then
   begin
      writeln('please enter a real number');
      noloop := false;
   end;
until noloop;
{$I+}

For i:=1 to nc do
begin
   writeln(x[i]:8:1,y[i]:8:1);
end;

SCAT:=0.0;
for i:=1 to nc do
begin
   ip:=i+1;
   x1:=X[i];
   y1:=y[i];
   x2:=x[ip];
   y2:=y[ip];

   Vec:=(x2-x1)*(x2-x1)+(y2-y1)*(y2-y1);
   v:=sqrt(vec);
   cross:=(x1-xzero)*(y2-y1)-(x2-x1)*(y1-yzero);
   ze:=cross/v;
   if (ze< -0.01) or (ze > 0.01) then
   begin
```

```
zeta:=abs(ze);
g:= ze/zeta;
dnom:=((x2-xzero)*(x1-xzero)+(y2-yzero)*
(y1-yzero));
if(dnom< -0.001) or (dnom> 0.001) then
begin
   Theta:=ArcTan(((y2-yzero)*(x1-xzero)-
   (y1-yzero)*(x2-xzero))/dnom);
end
else
begin
   theta:=pi/2.0;
end;
if g*theta < 0.0 then
begin
   theta:=pi-abs(theta);
end
else
begin
   theta:= abs(theta);
end;
n:=round( 18.0*theta/pi);
if n = 0.0 then
begin
   n:=1
end;
dnom:=((x1-xzero)*(x2-x1)+(y1-yzero)*(y2-y1));
if(dnom< -0.001) or (dnom> 0.001) then
begin
   phi:=arctan(((y1-yzero)*(x2-x1)-(y2-y1)*
   (x1-xzero))/dnom);
end
else
begin
   phi:=pi/2.0;
end;
if g*phi < 0.0 then
begin
   phi:=pi-abs(phi);
end
else
begin
   phi:= abs(phi);
end;
delta:=theta/n;
delt:=delta/6.283;
psi:=phi-delta/2.0;
{writeln('theta,delta',theta:8:4,delta:8:4);}
For j:=1 to n do
begin
```

```
psi:=psi+delta;
RI:=zeta/sin(psi);

If Ri > R[ni] then
   begin
      Ri:=r[ni];
   end;


{divide sectors of radius Ri into sections}


Nri:=round(Ri/1.0);
If Nri=0.0 then nri:=1;
delr:=ri/nri;

   For k:=1 to nri do
   begin
      ri:=delr+delr*(k-1);
      ri2:=ri-delr;
      rid:=ri-delr/2.0;

      cor2:=arctan((y1-yzero)/(x1-xzero));

      IF ((x1-xzero)>- 0.001) and ((x1-xzero)<
 0.001) then
         begin
            if (y1-yzero) > 0.0 then
               cor2:=pi/2.0
            else
               cor2:=-pi/2;
         end;

      ther:=delta/2.0+(j-1)*delta;
      gar:=cor2+ther;
      if (x1-xzero) > 0.0 then
            xri:=rid*cos(gar)
         else
            xri:=-rid*cos(gar);
      xri:=xri+xzero;
      coga:=cos(gar);
     { if i=1 then
      writeln('delta,cor2,ther,gar,coga',
      delta:8:4,cor2:8:4,ther:8:4, gar:8:4,
      coga:8:4);}
      w:=2;
      while (w < nw) and (XR[w] < xri) do
         w:=w+1;
      Dc:=wedge[w-1]+(wedge[w]-wedge[w-1])*
      (xri-xr[w-1])/(xr[w]-xr[w-1]);
```

```
{calc scat1 for ri and dc}

L:=2;
While (L < ni) and (R[l] < Ri) do
   begin
      L:=L+1;
   end;
Jd:=2;
While (Jd< nj) and (Dep[Jd]< Dc) do
   begin
      Jd:=Jd+1;
   end;
if (i=1) and (j=1) then
writeln('l,jd,sar[jd-1,l-1]',l:3,jd:3,
sar[jd-1,l-1]:8:2);

Sc1:=sar[Jd-1,l-1]+(sar[Jd-1,l]-
   sar[Jd-1,l-1]) *(Ri-R[L-1])/(R[L]-R[L-1]);

   Sc2:=sar[Jd,l-1]+ (sar[Jd,l]   -
   sar[Jd,l-1]) *(Ri-R[L-1])/(R[l]-R[l-1]) ;

   if (i=1) and (j=1) then
   writeln('sc1,sc2',sc1:8:2,sc2:8:2);

   SCAT1:=G*Delt*(Sc1+(Sc2-Sc1)*
   (Dc-Dep[Jd-1])/(Dep[Jd]-Dep[Jd-1]));

   L:=2;
   While (L < ni) and(R[l] < Ri2) do
      begin
         L:=L+1;
      end;
   Jd:=2;
   While (Jd< nj) and (Dep[Jd]< Dc) do
      begin
         Jd:=Jd+1;
      end;
   Sc1:=sar[Jd-1,l-1]+(sar[Jd-1,l]-
   sar[Jd-1,l-1]) *(Ri2-R[L-1])/(R[L]-R[L-1]);

   Sc2:=sar[Jd,l-1]+ (sar[Jd,l]   -
   sar[Jd,l-1]) *(Ri2-R[L-1])/(R[l]-R[l-1]) ;

   SCAT2:=G*Delt*(Sc1+(Sc2-Sc1)*
   (Dc-Dep[Jd-1])/(Dep[Jd]-Dep[Jd-1]));

   if (i=1) and (j=1) then
   writeln('i, j,k,Ri,rid,xri,Dc,scat1,
   scat2',i:2, j:2, k:2, Ri:4:1,rid:4:1,
```

```
                    xri:4:1,'  ',Dc:6:1,scat1:8:2,scat2:8:2);

                    SCAT:=SCAT+(SCAT1-SCAT2)


                end;
            end;
        end;
    end;
    Writeln('SCAT=',  SCAT:8:4);
end
```

REFERENCES

1. Aitken J.H., Henry W.H.: Int. J. Appl. Radiation (1964) 15, 713
2. Aspin N., Johns H.E., Horsley R.J.: Radiology (1961) 76, 76
3. Batho H. F., Theimer O., Theimer R.: J. Canad. Ass. Radiol.(1956) 7, 51
4. Berger M. J., Dogget J.: J. Res. Natl. Bur. Stand. (1956) 56,89
5. Bleehen N. M., Glatstein E., Haybittle J. L.: "Radiation Therapy Planning", Marcel Dekker, Inc. New York and Basel (1983)
6. Clarkson J. R.: Br. J. Radiol. (1941) 14, 265
7. Costrill L. : Hlth. Phys.(1962) 8, 261
8. Cunningham J. R.: Phys. Med. Biol. (1972) 17, 429
9. Cunningham J. R., Shrivastara P.N and Wilkinson J.M.: Comput. Programs Biomed. (1972) 2, 192
10. Day M.J.: Brit. J. Radiol. (1950) XXIII, 368
11. Day M.J.: Brit. J. Radiol. (1961) suppl.#10, 77
12. Dillman L.T. and von der Lage E.C.: Radionuclide decay schemes and nuclear parameters for use in radiation dose estimation. MIRD (1975) pamphlet #10, New York: Society of Nuclear Medicine (1975).
13. El - Khatib E.E, Podgorsak EB. and Pla C.: Med. Phys. (1986) 1316, 928
14. Enow K. and Jessen K.A.: Acta Radiol. Ther. Phys. Biol.(1974) 13, 262
15. Evans R.D.: The Atomic Nucleus. New York Mc Graw-Hill, 1955
16. Fano U.: Nucleonics (1953) 11/9, 55
17. Godwin P.N. and Opal C.: Radiology (1965) 84, 127
18. Gray L.H.: Proc. Roy. Soc. A. (1929) 122, 647
19. Gray L.H.: Proc. Roy. Soc. A. (1936) 156, 578
20. Gupta S.K. and Cunningham J.R.: Br. J. Radiol. (1966) 39, 7
21. Hanson W.F., Berkeley L.W. and Peterson M.: Med. Phy.(1980) 1, 145
22. Hering D.F. and Compton D.M.J.: Br. J. Radiol. Sp. Rep. (1970) No 5 , 51
23. Huang P.H., Kase K.R. and Bjärngard B.E.: Med. Phys. (1983) 10(6), 778
24. Huang P.H., Chris L.M. and Bjärngard B.E.: Med. Phys.(1986) 13(1), 57
25. Hubble J.H., Photon Cross-Sections, Attenuation Coefficients and Energy Absorption Coefficients from 10 KeV to 100 GeV, NSRDA - NBS 29, U.S. Department of Commerce, 1969
26. ICRU report # 23 (1973), Washington D.C. Measurement of Absorbed Dose in a Phantom Irridiated by a Single Beam of X or Gamma Rays.

27. ICRU report # 24 (1976), Washington D.C. Determination of Absorbed Dose in a Patient Irridiated by Beams of X or Gamma Rays in Radiotherapy Procedures
28. Jessen K.A.: ACTA Radiol. Ther. Phys. Biol.(1973) 12, 561
29. Johns H.E. and Cunningham J.R.: "The Physics of Radiology" IV edition, C.C.Thomas, (1983)
30. Jones D.E.A.: Brit. J. Radiol. (1949) XXII, 342
31. Leung D.M.K., Van Dyk J. and Robins J.:Br. J. Radiol. (1974) 47,805
32. Leung D.M.K., Johns H. E.: Med. Phys. (1977) 4, 441
33. Löfroth P.O.: Acta Radiol. Therapy Phys. Biol. (1973) 12, 552
34. Maruyama T., Kumamoto Y., Hashizume T. and Yamamoto M.: Health Phys. (1971) 20, 227
35. Mohan R. and Chiu Ch.: Med. Phys. (1985) 12(5), 592
36. Padikal P.A. and Deye J.A.: Phys. Med. Biol. (1978) 23, 1086
37. Peebles G.H., Glenn H. and Plesset M.S. : Phys. Rev. (1951) 81, 430
38. Plechaty E.F, Cullen D.E. and Howerton R.J.: Tables and graphs of photon interaction cross-section from 1.0 keV to 100 MeV derived from LLL evaluated nuclear data library. UCRL-504000 vol. 6. University of California, 1975.
39. Robinson D.M.: M.Sc. Thesis (1986)
40. Rogers D.W.O., Bielajew A.F. and Ewart G. M.: Med. Phys. (1984) 11, 401
41. Rogers D.W.O. and Bielajew A.F.: Nat. Res. Counc. Can. Report PXNR-2692 (1984a)
42. Scrimger J.W. and Cormack D. V.: Brit. J. Radiol. (1963) 36, 514
43. Shukovsky L. J.: Am. J. Roentgenol. (1970) 108, 27
44. Spencer L. V. and Attix F. H.: Radiation Res. (1955) 3, 239
45. TP-11/ Theraplan operator's manual (1982), AECL-commercial products
46. Theratron "F" Co unit manual
47. Van Dyk J.: Med. Phys. (1986) 13(1), 105
48. Wilks R. and Casebow M. P.: Br. J. Radiol. (1969) 42,452
49. Wong J.W., Henkelman R.M., Fenster A. and Johns H.E.: Med. Phys. (1981) 8, 775